Alma Mater Studiorum – Università di Bologna

DOTTORATO DI RICERCA IN

Ingegneria Civile, Ambientale e dei Materiali

Ciclo XXVII

Settore Concorsuale di afferenza: 08/B1

Settore Scientifico disciplinare: ICAR/06

The use of satellite remote sensing for flood risk management

Presentata da: Francesca Franci

Coordinatore Dottorato — Relatore

Prof. Alberto Lamberti — Prof. Gabriele Bitelli

Esame finale anno 2015

TABLE OF CONTENTS

KEYWORDS

Satellite remote sensing

Flood risk management

Geographic Information System

Change detection analysis

Object-based classification

ABSTRACT

Over the last decades the impact of natural disasters to the global environment is becoming more and more severe. The number of disasters has dramatically increased, as well as the cost to the global economy and the number of people affected. Among the natural disaster, flood catastrophes are considered to be the most costly, devastating, broad extent and frequent, because of the tremendous fatalities, injuries, property damage, economic and social disruption they cause to the humankind. In the last thirty years, the World has suffered from severe flooding and the huge impact of floods has caused hundreds of thousands of deaths, destruction of infrastructures, disruption of economic activity and the loss of property for worth billions of dollars.

In this context, satellite remote sensing, along with Geographic Information Systems (GIS), has become a key tool in flood risk management analysis.

Remote sensing for supporting various aspects of flood risk management was investigated in the present thesis. In particular, the research focused on the use of satellite images for flood mapping and monitoring, damage assessment and risk assessment. The contribution of satellite remote sensing for the delineation of flood prone zones, the identification of damaged areas and the development of hazard maps was explored referring to selected cases of study.

INTRODUCTION

The impact of natural disasters to the global environment is becoming more and more severe over the last decades. The reported number of disaster has dramatically increased, as well as the cost to the global economy and the number of people affected [1]. The strong increase in losses and people because of natural disasters is mainly due to the increased exposure of the world population to them. Both factors leading to a larger risk and factors leading to a higher occurrence of hazardous events are responsible for this situation [2].

Among the natural disasters, flood catastrophes are considered to be the most costly, devastating, broad extent and frequent, because of the tremendous fatalities, injuries, property damage, economic and social disruption they cause to the humankind. Over the last thirty, the world has suffered from severe flooding and the huge impact of floods, including river floods, flash floods, storm surge and tsunamis, has caused hundreds of thousands of deaths, destruction of infrastructures, disruption of economic activity and the loss of property for worth billions of dollars [1].

The last two decades have witnessed the increasing use of satellite remote sensing for understanding the geophysical phenomena underlying natural hazards [3]. Being able to observe large portions of the Earth surface, to perform frequent and regular in time measures and with the capability to investigate in the different bands of the electromagnetic spectrum, satellite remote sensing allows to study phenomena not directly accessible with the traditional surveying techniques and ongoing situations difficult to identify in another way [4].

Satellite remote sensing, along with Geographic Information Systems (GIS), has become a key tool in flood risk and damage assessment analysis [5]. Satellite images, acquired during, before and after a flood event, can provide valuable information about flood occurrence, intensity and progress of flood inundation, river course and its spill channels, spurs and embankments affected/threatened etc. so that appropriate mitigation measures can be planned and executed in time. Poor weather condition, generally associated with the floods, poor accessibility due to an

extreme flood event and the lack of instruments in recording hydrological information, with particular reference to developing countries, makes the ground assessment of inundated areas a difficult task. With a synoptic coverage over wide areas in a cost effective way, the application of satellite remote sensing allows to overcome these limitations. Satellite remote sensing can provide valuable information and objective data for supporting the disaster management activities and the decision making by means of the identification of hazardous areas, the assessment of the damaged zones and the definition and the monitoring of the recovery plans, after the occurrence of a disaster [4].

The main concern of this thesis is the delineation of flood prone areas, the identification of damaged areas and the development of hazard maps indicating flood susceptible areas by means of geospatial approaches. In particular, the contribute of satellite remote sensing and GIS for flood mapping and monitoring, damage assessment and risk assessment was explored referring to selected cases of study.

The first case of study focuses on the use of satellite images time series for flood mapping and monitoring purpose. The experimentation was performed on the Dhaka district area (Bangladesh). In recent decades, a rapid increase in urban population has occurred in Dhaka [6]. The rural-urban migration has significantly contributed to this growth. Unfortunately, the absence of an appropriate urban planning has been contributing to an urban sprawl, resulting in widespread environmental problems throughout the city. The increase in impervious surfaces, resulting from the rapid and uncontrolled urbanization, is not only threatening the agricultural land but also the local watershed, damaging and reducing the local water resources and exacerbating the impacts of water flows during the monsoon season, that typically affects the territory from May to October. In this context, multitemporal satellite images were processed in order to identify the flood prone areas and for monitoring the impact of land use/cover conversion on the surface water system around the city.

With the second case study, the contribute of satellite remote sensing for flood damage assessment was investigated. In particular, extreme flooding occurred in

Bangladesh in the 2004 were analysed. According to the World Risk Report 2014 Bangladesh was ranked 5 because of lives and properties losses caused by natural disasters [7]. In particular, among the natural disasters recorded between 1983-2014 in the Emergency Events Database (EM-DAT), floods were found the most harmful both in terms of people affected and in terms of economic losses. Different causes make this country dangerously subject to flooding. The country is located on an alluvial plain which contains almost 250 perennial rivers and most of the surface elevation is less than 5 m above sea level; heavy monsoon rains affect the country from May to September; rapid increase in river discharge can occur in spring due to the Himalaya snowmelt [8]. The experimentation was conduct on a large area located between Dhaka and the confluence of the main branch of the Gange River and the Meghna River. Pre-event and post-event satellite images were processed for mapping the submerged areas and thus to assess damages on the different land use/cover types.

The third case of study concerns the contribution of Earth Observation to flood risk assessment. In particular, the use of satellite remote sensing data, coupled with Multi-Criteria Analysis (MCA) technique, for generating flood hazard map was investigated. This approach was tested on a portion of the Yialias river watershed basin, in Nicosia district (Cyprus). Despite Cyprus is characterized by long and frequent dry periods, almost every year, localised and in some cases more widespread flooding affect parts of the island [9]. Various factors, such as the type and intensity of precipitations, the geomorphology, the geology and the human intervention to the territory are responsible for flood events. As the most of the island rivers, the Yialias has an intermittent stream being dry in summer. Therefore, the occurrence of heavy rainfalls commonly results in debris transport and blockage of structures, such as culverts and bridge openings, generally undersized for these flow rates. In order to produce an easily-readable and rapidly-accessible flood hazard map of the study area, the MCA was performed considering different flood-causing factor. A very high spatial resolution satellite image and the Digital Elevation Model (DEM) available for the study area were processed to prepare most of them.

In the first chapter, after a detailed introduction about the general concepts and terminologies commonly used in the field of disaster risk management, the contribution of remote sensing in natural disaster applications - with particular reference to satellite imagery - is described. In the following chapters, the selected case studies are exploited to propose different procedures - based on the use of satellite remote sensing data - for flood mapping and monitoring, flood damage assessment and flood risk assessment. Each chapter begins with the discussion of some peculiarities regarding the examined phase.

CHAPTER 1

REMOTE SENSING AND RISK MANAGEMENT

Being able to observe large portions of the surface of the Earth, to perform frequent and regular measures and with the capability to investigate in the different bands of the electromagnetic spectrum, satellite remote sensing allows to study and analyse phenomena not directly accessible with the traditional surveying techniques and ongoing situations difficult to identify in another way.

The last two decades have witnessed the increasing use of remote sensing for understanding the geophysical phenomena underlying natural hazards [4][10][3]. In particular, the development of new acquisition systems in the field of optical remote sensing, with the possibility to direct the sensor to specific areas, has enabled to increase the spatial and the temporal resolution of the satellite images, allowing theoretically to collect scenes of any part of the Earth surface with a time interval ranging between 1 and 7 days. Capable to collect data in all weather and lighting condition, active microwave sensors have proven to be useful to identify various spatial phenomena; especially in the context of natural disaster management, Synthetic Aperture Radar (SAR) images are used for detecting damaged areas and for the real-time monitoring of harmful events.

The impact of natural disasters to the global environment is becoming more and more severe over the last decades. The reported number of disaster has dramatically increased (Figure 1), as well as the cost to the global economy and the number of people affected [1] (Figure 2).

The strong increase in losses caused by natural disasters is mainly due to the increased exposure of the world population to them [11][7]. There are different elements responsible for this phenomenon, which can be subdivided in factors leading to a larger risk and factors leading to a higher occurrence of hazardous events [2] (Figure 3). In particular, the increased risk is due to the rapid increase of the world population, which has doubled in size from 3 billion in the 1960s to 6 billion in 2000. According to the United Nations Department of Economic and Social

Affairs (UN/DESA) population estimates and projections, the world population of 7,2 billion in mid-2013 is projected to increase by almost one billion people within the next twelve years, reaching 8,1 billion in 2025, and to further increase to 9,6 billion in 2050 and 10,9 billion by 2100 [11].

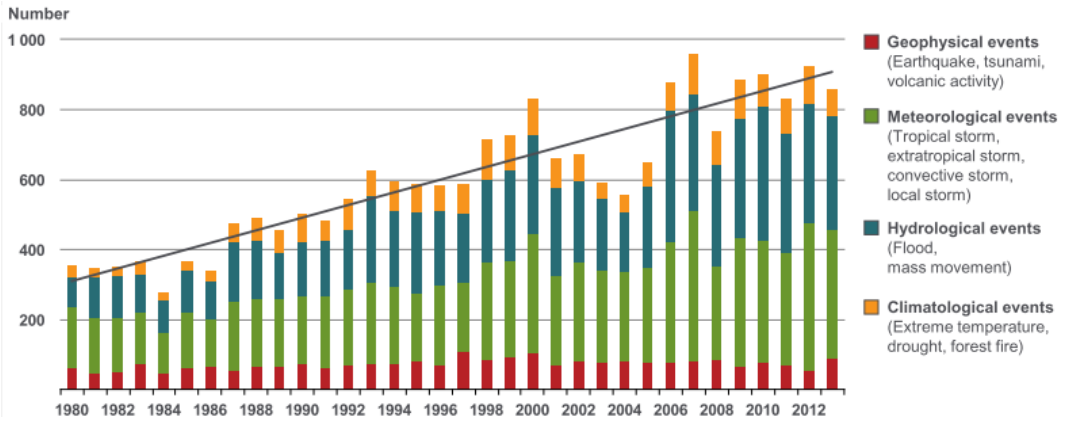

Figure 1 Number of loss natural disaster events between 1980 – 2013.

(source: Munich Re, 2014 [1])

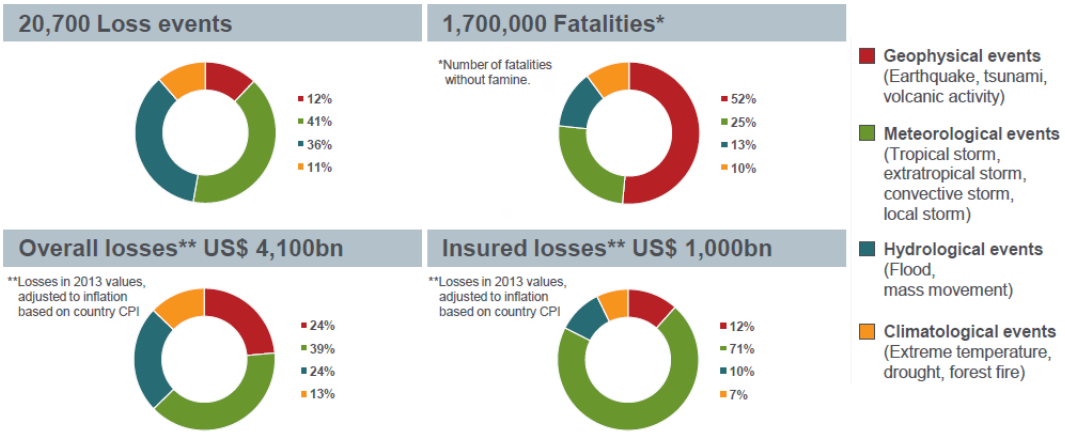

Figure 2 Losses in percentage distribution due to natural disaster events between 1980 – 2013.

(source: Munich Re, 2014 [1])

Another factor related to the population pressure is that areas that were previously avoided due to their susceptibility to natural hazards have become settled. In addition, there is the important trend of the concentration of people and economic activities in large urban centres (Figure 4), most of which are located in vulnerable areas. Mega-cities with a very rapid growth mostly experience the occupation of marginal land, susceptible to disasters, by the poor newcomers [7][6].

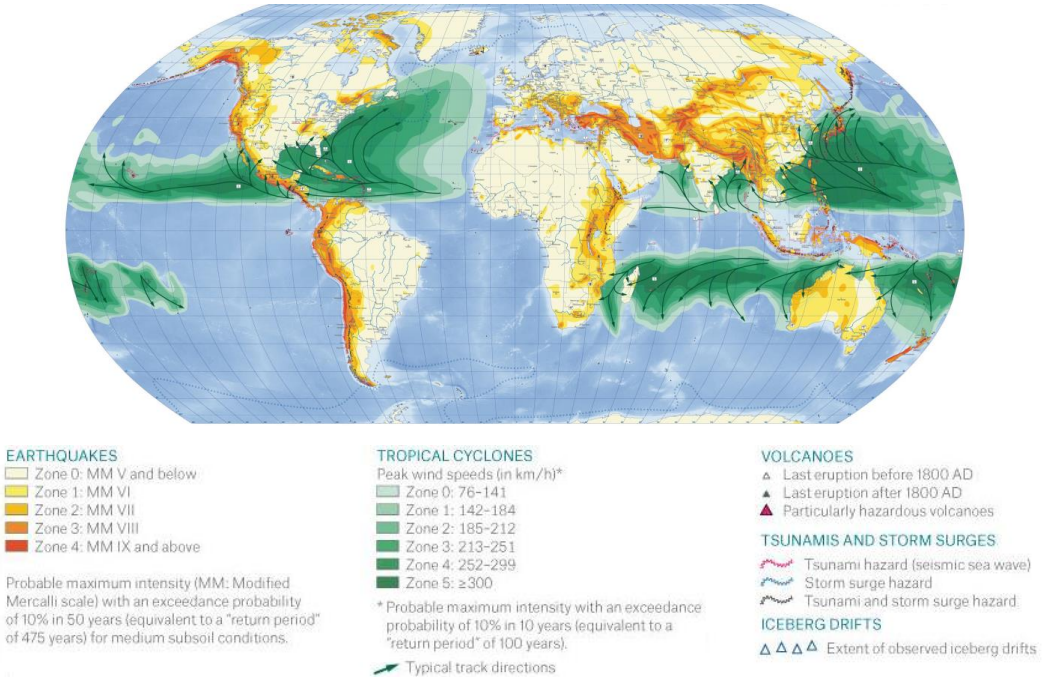

Figure 3 World map of natural hazards.

(source: Munich Re, 2011 [2])

Figure 4 Distribution of world population into urban and rural areas.

(source: *Garschagen et al.*, 2014 [7])

To effectively reduce the impacts of natural disasters, a complete strategy for disaster risk management is required. As defined by the United Nations Inter-Agency Secretariat of the International Strategy for Disaster Reduction (UN/ISDR), it consists in systematic process of using administrative decisions, organization, operational skills and capacities to implement policies, strategies and coping capacities of the society and communities to lessen the impacts of natural hazards and related environmental and technological disasters [12]. This comprises all forms

of activities, including structural and non-structural measures, to avoid or to limit adverse effects of hazards.

In this context, remote sensing provides valuable information helping to understand spatial phenomena and supporting the decision making with objective data. In particular, it can contribute to the disaster management activities through the identification of hazardous areas, the assessment of the damaged zones in a timely manner and assisting the recovery plans after the occurrence of a disaster.

In the following sections, after a detailed introduction to the general concepts and terminologies commonly used in the field of disaster risk management, is described the contribution of remote sensing in natural disaster applications, with particular reference to the satellite images.

1.1 Hazard, Vulnerability and Risk notions

There are many definitions and terms in the field of disaster risk assessment/management. In this section common terminologies and notions used to describe disaster, hazard, vulnerability, and risk are presented.

Disasters are defined as “a serious disruption of the functioning of a community or a society causing widespread human, material, economic or environmental losses which exceed the ability of the affected community or society to cope using its own resources” [12]. According to the United Nations - International Strategy for Disaster Risk Reduction (UN/ISDR), a disaster is a function of the risk process; it results from the combination of hazards, vulnerability conditions and insufficient capacity or measures to reduce the potential negative consequences of risk. Therefore, the distinction among disaster, hazard, vulnerability and risk terms is a crucial point for a proper understanding of which factors and parameters, and how, are involved and influence an effective risk management.

The term hazard indicates a potentially damaging physical event or phenomenon or human activity that can cause the loss of life or injury, or other health impacts, as well as damage and loss to property, infrastructure, livelihoods, service provision and environmental resources property damage, social and economic disruption or environmental degradation. Thus, hazard identifies a threat or potential adverse

effects, not the physical event itself. Physical events become hazards where social elements or environmental resources, that support human welfare and security, are exposed to their potentially adverse impacts and exist under conditions that could predispose them to such effects [13]. Hazards can be subdivided in natural, human-induced and socio-natural. Natural hazards are natural processes or phenomena in Earth's system that may constitute a damaging event (e.g. earthquakes, tropical cyclones, volcanoes, tsunamis and storms); human-induced hazards are those resulting from modifications of natural process in the Earth's system caused by human activities that accelerate/aggravate the damage potential (e.g. land degradation, landslides, and forest fires). Finally, human-made hazards originate from technological or industrial accidents, dangerous procedures, infrastructure failures, or certain human activities, which may cause the loss of life or injury, property damage, social and economic disruption, or environmental degradation (e.g. industrial pollution, nuclear activities and radioactivity, toxic wastes, dam failures, and transport, industrial, or technological accidents such as explosions, fires, and oil spills). Hazards can be single, sequential or combined in their origin and effects. Each hazard is characterised by its location, intensity, area affected, intensity, speed of onset, duration and frequency [14].

The use of the term vulnerability can span from the notion of the predisposition of a system to be affected or damaged by an external event at a certain instant of time to the notion of the residue of potential damages which cannot be targeted through the implementation of typical measures; or as conditions of incapacity to cope with disasters once they have taken place [15]. According to the definition of the UN/ISDR, the term vulnerability indicates the conditions determined by physical, social, economic and environmental factors or processes which increase the susceptibility of a community to the impact of hazards [12]. It is used to refer the degree of susceptibility of people, factories, offices or other business assets to suffer damage and loss, for example due to inadequate design and construction, lack of maintenance, unsafe and precarious living conditions, lack of access to emergency services. Generally, together with the vulnerability notion the concept of capacity is mentioned, referring to those positive factors which can increase the

ability of people to cope with hazards. Capacity is a combination of all the strengths and resources available within a community, society or organization that can reduce the level of risk, or the effects of a disaster.

In the framework proposed by the scientific community as indicated by the International Strategy for Disaster Reduction (ISDR) and its predecessor, the International Decade for Natural Disaster Reduction (IDNDR), the term risk is defined as the probability of harmful consequences, or expected losses (deaths, injuries, property, livelihoods, economic activity disrupted or environmental damage) resulting from interactions between natural or human-induced hazards and vulnerable conditions [12] (Figure 5). Conventionally, risk is expressed by the combination of hazards and vulnerability. An example of such a function is proposed by ISDR:

$$Risk = Hazards\ x\ Vulnerability$$

Some authors also include the concept of exposure to refer particularly to the physical aspects of vulnerability [16][17]. In this context, vulnerability is an intrinsic characteristic of people, infrastructure, economically and environmentally important land uses while the hazard is related to magnitude, duration, location and timing of the event. In this case, the relation between risk, hazard, vulnerability and exposure is represented as follows:

$$Risk = Hazard\ x\ Exposure\ x\ Vulnerability$$

As proposed by Villagrán [15], risk is a function of hazard, vulnerability and deficiencies in preparedness:

$$Risk = Hazard\ x\ Vulnerability\ x\ Deficiencies\ in\ Preparedness$$

In this relation, deficiencies in preparedness (e.g. the lack of emergency committees and emergency plans, the lack of early warning systems, and related measures) refer to those pre-existing conditions which inhibit an institution, a community, society or a country to respond in an effective and opportune way once the event is triggering the disaster to minimize its impacts, in particular the loss of lives. Such deficiencies would include the lack of emergency committees and emergency plans, the lack of early warning systems, and related measures.

In this context, the risk assessment/analysis, defined as a methodology to determine the nature and extent of risk by analysing potential hazards and evaluating existing conditions of vulnerability, exposure and capacity [12], is a complex process, as the intrinsic components need to be assessed individually and then combined through some kind of algorithm to produce the expected outcome. Regardless of the model employed to represent risk, the result should be the same, as defined by ISDR.

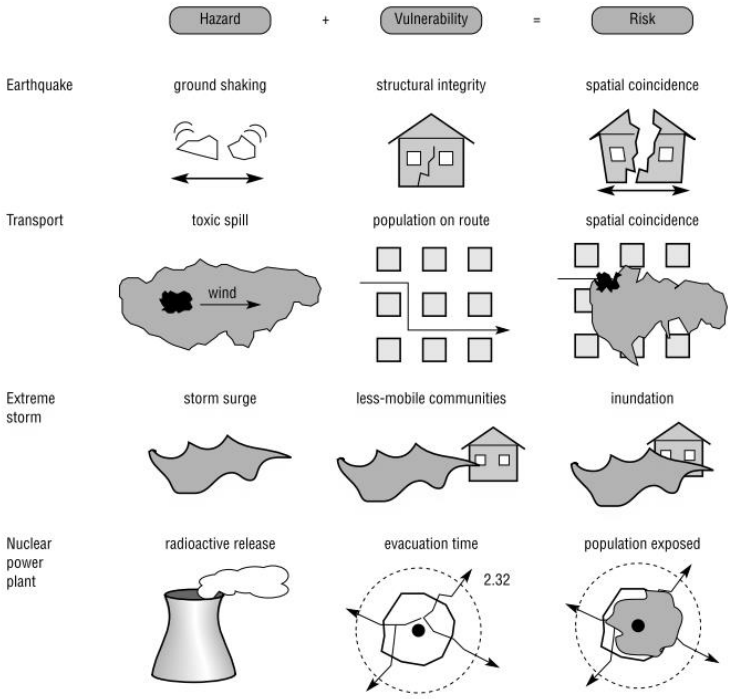

Figure 5 Examples of how hazard, vulnerability and risk concepts

(source: *Cova*, 1999 [18])

1.2 The disaster risk management cycle

The disaster risk management is defined as the systematic process of using administrative decisions, organization, operational skills and capacities to implement policies, strategies and coping capacities of the society and communities to lessen the impacts of natural hazards and related environmental and technological disasters [12].

The disaster risk management planning consists of four stages: mitigation and preparedness, prior to the disaster occurrence, and response and recovery which take place after the occurrence of the disaster [19]. Disaster management is

represented by a cycle model not only because the four phases are interconnected and integrated during all the planning process but also because the occurrence of a disaster event will eventually influence the way of preparing for the next one (Figure 6). Decisions about the risk mitigation can influence the preparedness planning and the response actions required; the preparedness level of the affected communities and responders can influence the severity of the disaster impact; the recovery stage will depend from the effectiveness of the response actions and can include risk reduction measures for reducing the future vulnerability.

Figure 6 Disaster management cycle

The mitigation phase refers to the actions and measures that attempt to reduce the likelihood of a disaster occurring. This is carried out by risk identification and reduction process.

Prior to a disaster's occurrence, the main aim of the preparedness stage is the planning of an efficient response to hazards in order to reduce their impacts. Considered as a bridge between disaster mitigation and disaster management, preparedness accepts the existence of residual and unmitigated risk and attempts to aid the community in eliminating certain of the adverse effects that could be experienced once an event occurs by training of emergency planners and rescuers, public education on hazards and their consequences, installation of early warning systems, planning of evacuation routes and emergency centres, national and international plans for assistance and aid.

The response phase consists of all activities, such as evacuation, rescue and needs assessment, carried out immediately before, during, and after a disaster occurs in order to save lives and minimize the property damages.

After a catastrophic event, the goal of the recovery phase is to restore normal life in disaster-affected areas. This stage can include many steps that start with the restoration of the lifeline utilities and the identification of the places for the reconstruction and continue with the monitoring of the communities rebuilding.

A comprehensive and effective framework of the disaster risk management cycle and how the notions of risk, hazard and vulnerability (section 1.1) are reflected into its various stages is described by *Taubenböck et al.*, 2008 [20]. The disaster management cycle relates risk, hazard, vulnerability to the timeline; the cycle model highlights various temporal phases where different types of indicators enable the assessment of the situation.

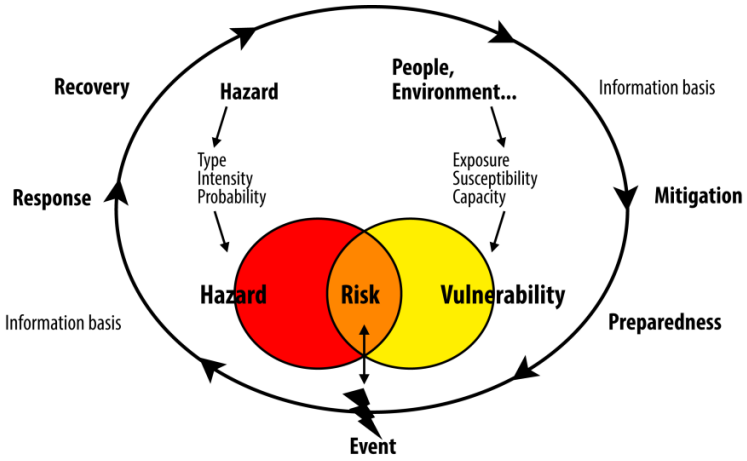

Figure 7 Risk as result of the interaction of the hazard and the vulnerability embedded in the various phases of the disaster management cycle

(source: adapted from *Taubenböck et al.*, 2008)

1.3 Satellite remote sensing in the disaster risk management cycle

An increasing number of studies have been elaborated on the importance and applications of remote sensing, with particular reference to satellite remote sensing data, in the disaster risk management [3][10]. A major reason of using remote sensing in this field is that it is the fastest means of collection data for pre and post-event disaster studies [21].

Satellite remote sensing refers to the technology used for observing various earth phenomena with instruments that are typically on board a spacecraft. These observations consist of measuring the electromagnetic energy of phenomena that occur without physical contact with the object of interest. Therefore, to investigate the Earth's surface without being in contact with it is an important feature considering the limited accessibility of the areas affected by a disaster and, in many cases, their extension and imperviousness. In addition, bandwidths are a crucial component of remote sensing operations. In fact, the different bandwidths of the electromagnetic spectrum are related to certain phenomena and Earth parameters that can be monitored and analysed using various sensors.

Satellite remote sensing can provide valuable information in each phase of the disaster risk management cycle, helping to understand spatial phenomena and supporting the decision making with objective data [4][22]. It can contribute to the risk management activities through the identification of hazard areas, the assessment of damaged zones in a timely manner and assisting the recovery plans.

Each phase of the risk management cycle requires satellite images data with appropriate characteristics of spatial, spectral and temporal resolution depending on the kind of information to be obtained, such as physical indicators and measureable features, and the spatial scale of the analysed hazard [21].

In the mitigation stage, the remote sensing data are usually employed for mapping landscape features (i.e. land use/land cover) and for detecting potentially hazardous areas; therefore, the update representations of a territory is an important requirement to select useful satellite images. Furthermore, high spatial resolution images can allow for the identification of infrastructure and buildings in risk areas, for the hazards consequence assessment (vulnerability) and the potential losses evaluation.

In the preparedness phase remote sensing data can support the developing of risk maps and models, using the information obtained in the previous stage, which are generally used by authorities to communicate information about location and range of hazard to the community.

During the pre-event phases and recovery stage there is sufficient time for selecting appropriate remote sensing data; instead, the timeliness is a crucial factor in the response phase during which the rapid damage assessment is fundamental for efficient emergency services and to assist evacuation plans. Moreover, the availability of high spatial resolution images allows a detailed representation of the ongoing situation.

In the recovery stage, remote sensing data are used for post-disaster census information, for identifying the rebuilding sites and for the long term monitoring of the territory; in particular, remote sensing can support this stage providing time series images over large areas with both high and medium spatial resolution from which changes can be detected and quantified.

1.3.1 Satellite remote sensing data types

There are many types of satellite sensors that can support the four stages of the disaster management cycle. The contribute of satellite remote sensing ranges from optical collected by passive sensors and thermal images to active microwave imaging [4] (Table 1). A comprehensive report of remotely sensed data types and image processing techniques for information extraction about natural hazards can be found in *Joyce et al.*, 2009 [23]. Often, more than one sensor is needed to properly meet all the requirements of a specific application [24].

Optical images, particularly when collected using true colour spectral bands (red, green and blue), are used by the disaster management community since they are simple to be interpreted. In particular, these images are effectively used to support the recovery monitoring and during the planning activities in the pre-event stages [25][26][27]. The use of optical images on the response phase depends on the speed of the data acquisition that is crucial for a rapid detection of the damaged areas [28][29]. For instance, sensors installed on geostationary satellites provide data for large area extent but low spatial detail therefore these type of data is appropriate for monitoring weather patterns, cyclones, etc. [30]. On the other hand very high spatial resolution images (e.g. SPOT, Ikonos, Quickbird) are effectively used when targeting relatively small area [31][32][33]. The greatest limitations of

the optical sensor are the impossibility of acquiring images through clouds, haze and smoke, which cause the loss of information on the ground, and during the night since these sensors detect the solar radiation reflected from the observed surface.

Table 1 Applications of different wavebands for hazard mapping and monitoring.

(source: *Lewis*, 2009 [34]**)**

Wavelength	Waveband	Example applications	Example sensors
Visible	0,4-0,7 μm	Vegetation mapping	SPOT; Landsat
		Building stock assessment	AVHRR; MODIS; IKONOS
		Population density	IKONOS; MODIS
		Digital elevation model	ASTER; PRISM
Near infrared	0,7-1,0 μm	Vegetation mapping	Spot; Landsat; AVHRR; MODIS
		Flood mapping	MODIS
Shortwave infrared	1,0-3,0 μm	Water vapour	AIRS
Thermal infrared	3,0-14 μm	Active fire detection	MODIS
		Burn scar mapping	MODIS
		Hotspots	MODIS; AVHRR
		Volcanic activity	Hyperion
Microwave (radar)	0,1-100 cm	Earth deformation and ground movement	Radarsat-2; TerraSAR-X; TanDEM-X; COSMO-SkyMed; PALSAR
		Rainfall	Meteosat; Microwave Imager (TRMM)
		River discharge and volume, flood mapping and forecasting	Radarsat-2; TerraSAR-X; TanDEM-X; COSMO-SkyMed; PALSAR; AMSR-E
		Surface winds	QuikScat radar
		3D storm structure	Precipitation radar (TRMM)

Even though thermal images have a lower spatial resolution than that capable of being achieved with optical and multispectral images, because of their comparatively low energy (energy decrease with increasing wavelength), they provide a valuable source of information for detecting volcanic activities [35] and wildfires [36]. Thermal imagery can be acquired during the day or night since the radiation is emitted not reflected [37].

Conversely, Synthetic Aperture Radar (SAR) sensors are active system, producing its own illumination. They illuminate the terrain and arrange the received signals reflected into an image. Therefore, active microwave sensors are capable to acquire data in all weather and lighting condition. Both backscatter intensity and the phase of SAR images can be used [38][39][40][41]. The backscatter intensity depends on

the dielectric properties of the reflecting material, the surface roughness and the sensor wavelength therefore, the accurate interpretation can sometimes be difficult but at the same time useful information about damaged infrastructures and hazardous phenomena such as landslide, tsunami, flooding [42], etc. can be effectively achieved [32].

1.3.2 Initiatives for using remote sensing data in the disaster management

The usefulness of Earth observation data in natural disaster management has been proven by the numerous ongoing international and national initiatives which have made easier the access to space-based information [43].

The International Charter "Space and Major Disasters" involves the majority of the space agencies (e.g. ESA, CNES, CSA, ISRO, USGS, DLR, etc.) with interest in Earth observation, and aims at providing a unified system of space data acquisition and delivery to those affected by natural or man-made disasters through authorized users [44].

Among the United Nations systems, the UNITAR's Operational Satellite Applications Programme (UNOSAT) provides satellite solutions and geographic information easily accessible to UN decision makers, member states, international organizations and non-governmental organizations for reducing the impact of crises and disasters and supporting plans for sustainable development [45]; the United Nations Platform for Space-based Information for Disaster Management and Emergency response (UN-SPIDER) has been established to ensure that all countries and international and regional organizations have access to and develop the capacity to use all types of space-based information to support the full disaster management cycle [46].

In Europe, Copernicus Programme (previously known as Global Monitoring for Environment and Security - GMES), initiative of the European Commission and the European Space Agency (ESA), is actively supporting the use of satellite technology in disaster management, with projects such as PREVIEW (Prevention, Information and Early Warning pre-operational services to support the management of risks), LIMES (Land and Sea Integrated Monitoring for Environment and Security), GMOSS

(Global Monitoring for Security and Stability), SAFER (Services and Applications For Emergency Response), and G-MOSAIC (GMES services for Management of Operations, Situation Awareness and Intelligence for regional Crises) [47].

The Sentinel Asia project supported by the Japan Aerospace Exploration Agency (JAXA) aims to promote international cooperation to prevent, monitor and mitigate natural disasters in the Asia-Pacific region using space technologies to collect disaster-related information and sharing it over the internet [48].

Various organizations and program are involved in rapid mapping activities after major disasters including ITHACA (Information Technology for Humanitarian Assistance, Cooperation and Action) [49], DLR-ZKI (Deutsches Zentrum fur Luft und Raumfahart - Zentrum für satellitengestützte Kriseninformation) [50], SERTIT (SErvice Régional de Traitement d'Image et de Télédétection) [51], GDACS (Global Disaster Alert and Coordination System) [52], the Dartmouth Flood Observatory [53].

The list of initiatives above mentioned is far from being exhaustive, but it gives an idea of the raised interest to disaster management from the organizations and the remote sensing community.

1.4 Remote sensing and flood risk management

Flooding is a natural and recurring event for a river or stream. It is caused in most cases by heavy or continuous rainfall, which exceeds the absorption capacity of soil and the flow capacity of rivers. Such rains may originate from storms, tornadoes, etc. Moreover, floods can be caused also by rapid melting of snow caps, by tsunami and by dam bursts due to natural events or human failure [54].

The world has suffered from severe flooding over the last decade. In recent years the huge impact of floods has caused hundreds of thousands of deaths, destruction of infrastructures, disruption of economic activity and the loss of property worth billions of dollars. Flood catastrophes are considered to be the most costly, devastating, broad extent and frequent because of the tremendous fatalities, injuries, property damage, economic and social disruption they cause to the humankind [1] (Table 2). Significant examples are the 2000 Mozambique flood

caused by heavy rains followed by a cyclone, floods due to heavy rainfall in Germany in 2002, the tsunami on the coasts of the Indian Ocean in 2004, Hurricane Katrina in New Orleans in 2005, the cyclone Nargis in Myanmar in 2008, the heavy monsoon floods in Pakistan in 2010, floods caused by abnormally heavy rains in Philippines between December 2010 and January 2011, and the Colorado flood in 2013.

Table 2 Most severe flood events recorded between 1999-2014, ordered by people affected (left) and economic damages (right).

(source: Emergency Events Database EM-DAT, http://www.emdat.be/)

Country	Year	Total people affected
China P Rep	2003	150.146.000
China P Rep	2010	134.000.000
China P Rep	2007	105.004.000
China P Rep	1999	101.024.000
China P Rep	2002	80.035.257
China P Rep	2011	67.900.000
India	2002	42.000.000
China P Rep	2009	39.372.000
Bangladesh	2004	36.000.000
China P Rep	2004	33.652.026

Country	Year	Total damage (US$ *1000)
Thailand	2011	40.000.000
China P Rep	2010	18.000.000
India	2014	16.000.000
Germany	2013	12.900.000
Germany	2002	11.600.000
United States	2008	10.000.000
Pakistan	2010	9.500.000
China P Rep	1999	8.100.000
Italy	2000	8.000.000
China P Rep	2012	8.000.000

During the past decades satellite remote sensing, along with Geographic Information Systems (GIS), has become a key tool for flood risk and damage assessment [55][56]. Remote sensing facilitates the flood surveys by providing the much needed information for flood studies. Satellite images acquired in different spectral bands during, before and after a flood event can provide valuable information about flood occurrence, intensity and progress of flood inundation, river course and its spill channels, spurs and embankments affected/threatened etc. so that appropriate flood relief and mitigation measures can be planned and executed in time.

Poor weather condition generally associated with the floods, poor accessibility due to an extreme flood event and the lack of instruments in recording hydrological information, with particular reference to developing countries, makes the ground assessment of inundated areas a difficult task. With a synoptic coverage over wide

areas in a cost effective way, the application of satellite remote sensing allows to overcome these limitations. Through the selection of appropriate sensors and platforms, remote sensing can provide accurate and timely estimation of flood inundation, flood damage and flood prone areas.

Development in remote sensing has furthermore evolved from optical to radar remote sensing, which has provided an all-weather imaging capability (section 2.1).

In this context, GIS can be useful not only for generating the visualization of flooding maps obtained by processing satellite images but also to integrate and analyse other data or factors which are required for an effective flood risk management.

In the following part of the thesis, the contribution of remote sensing application in flood risk management is discussed considering the generic four phases of risk management described above to three distinct areas, because the information obtained by geospatial approaches can support more than one stage. Therefore, the use of satellite remote sensing for mapping and monitoring flooded areas, assessing damages and predicting possible extensions of the flood was explored (Table 3).

Table 3 The contribution of satellite remote sensing for supporting flood risk management stages.

Flood mapping and monitoring	Damage assessment	Flood risk assessment
Mitigation		
Preparedness	Response	Mitigation
Response	Recovery	Preparedness
Recovery		

A flood map is prepared after a flood event occurrence in order to delineate the inundated areas. Floods are dynamic phenomena, therefore flood maps of different times are suitable for monitoring water expansion and regression. Moreover, multitemporal maps can aid to detect critical spatial changes in flood hazard and vulnerability over time. These products can be used for flood prone areas delineation in order to prevent future floods; they provide crucial information to identify appropriate protection measures and strategies for the risk mitigation. Flood maps can be employed for the preparation of an efficient response plans.

Once a flood event occurs, emergency planners and rescuers can use inundation maps to detect the most affected areas and then to identify evacuation routes and plan the assistance and aids. During the recovery stage, flood maps can support the identification of the places for the reconstruction and multi-date maps aid the monitoring of a community rebuilding [5][57].

The flood damage assessment map is produced after a flood event to present socio-economic damages. Generally based on land use/cover data, administrative units, socio-economic statistics, inundation extent and duration and water depth, this product provides information about the flood impacts which can be used both for planning rescue operations - during the response phase - and for recovery actions [54].

The purpose of a flood risk assessment is to identify flood prone areas. To evaluate flood risk, there are several qualitative and quantitative approaches, which can involve different data such as hydraulic information, topographic base map, terrain models, land use/cover map, inundation map, population density etc. A range of techniques is available within the GIS to evaluate hazards and vulnerability in relation to floods and one of the common approaches consists on the construction of indexes by combining various indicators [58]. Risk maps should be available in advance of a flood event therefore, they can help stakeholders to prioritise investments and allocate resources for mitigation activities. They can be used for the reallocation of facilities and infrastructures at risk and for the formulation of suitable plans for future expansion; moreover, these maps enable authorities and people to prepare for disasters [59].

The role of satellite remote sensing and GIS for flood mapping and monitoring, the damage assessment and finally the development of hazard map, indicating flood susceptible areas, will been then explored in the next three chapters, introducing each topic with a discussion about some specific question and then presenting one application for a selected case of study.

CHAPTER 2

FLOOD MAPPING AND MONITORING

Satellite remote sensing provides the instantaneous and synoptic view necessary to accurately map the extent of floods. Therefore, it is effectively used to delineate inundation areas and it is considered highly potential to reduce flood losses and deaths during the response phase.

Mapping of the flooded areas using optical images is based on the fact that water absorbs or transmits most of the electromagnetic energy in the near-infrared (NIR) and medium-infrared (MIR) wavelengths, which results in less reflection. Optical remote sensing techniques, though providing very fine spatial resolution, are less capable of penetrating through the clouds, which limit their application in bad weather condition. Use of microwave remote sensing techniques, with its all-weather capability, compliments the existing optical images to overcome this. Water surface provides specular reflection of the microwave radiation, and hence very little energy is scattered back compared to the other land features. The difference in the energy received back at the radar sensor is used for differentiating and to mark the boundaries of the water bodies. In some cases, both optical and microwave data are clubbed to get a better perspective of the flood map [60].

2.1 Application of optical and radar remote sensing

In the initial stages of satellite remote sensing, the available data were from Landsat Multi Spectral Scanner (MSS) in four spectral bands and with a spatial resolution equal to 80 meters. Landsat mission represents the world's longest continuously acquired collection of space-based moderate resolution land remote sensing data [61] (Table 4). The MSS data exist since 1972 when Landsat1 satellite was successfully launched. The pioneering investigations of the use of remote sensing data for flood mitigation were predominantly concentrated on the flood prone regions of USA [62][58]. In particular, the band 7 (0,8-1,1 μm) has been found suitable for the detection of water or moist soil because of the strong absorption of the water in the near infrared range of the spectrum. From the early 1980s, Landsat

Thematic Mapper (TM) imageries comprising seven spectral bands, six with 30 m spatial resolution and one in the thermal infrared range with 120 m, became the main source of data for monitoring floods and delineating the boundary of inundation. Special attention was given to dealing with monsoon flooding in the developing countries [55]. Landsat TM band 4 (NIR) also proved to be useful in discriminating water surfaces from equivalent of MSS band 7 [63]. However, the low energy reflected by developed land use areas (e.g. downtown commercial, urban areas, industrial areas) in the near infrared band, may cause problem in separating water from certain urban features. This confusion can be successfully solved by adding TM band 7 (2,08-2,35 μm) to the TM band 4 [64]; in fact, in the band 7 images the reflectance from water, paved road surfaces and roof tops differs significantly. Therefore, adopting TM band 4 plus band 7 images, selecting the density slice for extracting the flood water, becomes easier. In the 1999, the Landsat7 satellite was successfully launched six years after the failure of the Landsat6 launch. The instrument on Landsat7, the Enhanced Thematic Mapper Plus (ETM+), replicates the capabilities of the highly successful TM sensor on Landsat4 and Landsat5 including the first panchromatic band with 15 m spatial resolution and the thermal infrared channel with 60 m spatial resolution [65]. On May 31, 2003, the Scan Line Corrector (SLC), which compensates for the forward motion of Landsat7, failed causing duplication in the imaged area with width that increases toward the scene edge. Despite this fact, ETM+ is still capable of acquiring useful data, particularly within the central part of any scene. With Landsat5 retiring in 2013, leaving SLC-offLandsat7 as the only on-orbit Landsat program satellite, the launch of the Landsat8 in the same year has ensured the continued acquisition and availability of Landsat data. The Landsat8 collects Earth images with a 16-day repeat cycle in an 8-day offset to Landsat7 and carries two instruments: the Operational Land Imager (OLI) and the Thermal InfraRed Sensor (TIRS). The OLI sensor, while similar to ETM+ sensor, provides enhancement from prior Landsat instruments with the addition of two new spectral bands: a deep blue visible channel (0,433-0,453 μm), specifically designed for water resources and coastal zone investigation, and a new infrared channel (1,360-1,390 μm) for the detection of cirrus clouds. The TIRS

sensor provides two thermal bands, formerly covered by one wide spectral band on Landsat4 and 7, with a minimum of 100 meter resolution.

Thanks to the continuous periodical acquisition, Landsat images are often used for multitemporal studies by means of change-detection algorithms (e.g. image differencing, image ratio, principal component analysis, etc.) which can contribute significantly in detecting flooded areas [66][67][68][69]. In addition, various combinations bands, including band ratio approaches, differences, additions are also used to delineate flood-prone areas using Landsat data [70][64][71][72].

Table 4 Technical Specifications of Landsat sensors

(source: http://landsat.gsfc.nasa.gov/)

Satellite	Launch (End of service)	Sensor		Wavelength (μm)	Spatial resolution (m)	Coverage repeat (days)
Landsat 1-2	L1:7/23/72 (1/6/78) L2: 1/22/75 (2/25/82)	RBV	1	0,48-0,57	80	18
			2	0,58-0,68		
			3	0,70-0,83		
		MSS	4	0,50-0,60	80	
			5	0,60-0,70		
			6	0,70-0,80		
			7	0,80-1,1		
Landsat 3	3/5/78 (3/31/83)	RBV	1	0,505-0,75	40	18
		MSS	4	0,50-0,60	80	
			5	0,60-0,70		
			6	0,70-0,80		
			7	0,80-1,1		
			8	10,4-12,6	240	
Landsat 4-5	L 4*: 7/16/82 L 5: 3/1/84 (6/5/2013) *TM data transmission failed in August 1993	MSS	4	0,50-0,60	80	16
			5	0,60-0,70		
			6	0,70-0,80		
			7	0,80-1,1		
		TM	1	0,45-0,52	30	
			2	0,52-0,60		
			3	0,63-0,69		
			4	0,76-0,90		
			5	1,55-1,75		
			6	10,4-12,5	120	
			7	2,08-2,35	30	

Satellite	Launch (End of service)	Sensor		Wavelength (μm)	Spatial resolution (m)	Coverage repeat (days)
Landsat 7	4/15/99	ETM+	1	0,45-0,52	30	16
			2	0,52-0,60		
			3	0,63-0,69		
			4	0,76-0,90		
			5	1,55-1,75		
			6	10,4-12,5	60	
			7	2,08-2,35	30	
			PAN	0,50-0,90	15	
Landsat 8	02/11/2013	OLI	1	0,433-0,453	30	16
			2	0,450-0,515		
			3	0,525-0,600		
			4	0,630-0,680		
			5	0,845-0,885		
			6	1,560-1,660	60	
			7	2,100-2,300	30	
			8	0,500-0,680	15	
			9	1,360-1,390	30	
		TIRS	10	10,6-11,2	100	
			11	11,5-12,5		

Satellite Pour l'Observation de la Terre (SPOT) data were also used for flood delineation with the assumption that water has very low reflectance in the near-infrared portion of the spectra [73][74][75][76]. The SPOT constellation includes seven medium-high resolution satellites launched starting in 1986; three are still active (SPOT 5,6,7). From the first satellite, the spatial resolution has been greatly increased; the newest satellites, SPOT 6 and 7 (launched in 2012 and 2014) collect images with a pixel size of 2,2 m and 8 m in the panchromatic and multispectral respectively (Table 5).

Among the optical satellite images, the data collected by Moderate Resolution Imaging Spectroradiometer (MODIS), the key instrument on board the Terra and Aqua satellites, has been largely used for flood mapping and flood's progression through time [77]. The spatial resolution of the MODIS sensor, 250 m (band 1-2), 500 (band 3-7), 1000 m bands 8-36), may not be ideal for mapping small water features but, since Terra was launched in December 1999, it has become possible to monitor continental-scale inundated areas [78]. Terra passes from North to South

across the equator in the morning, while Aqua passes South to North over the equator in the afternoon and they view the entire Earth's surface every 1-2 days, acquiring data in 36 spectral bands (from 0,4 μm to 14,4 μm). Therefore, MODIS images are particularly useful for covering large areas with high temporal resolution which is an important characteristic for a daily water monitoring [79]. All historical data from 2000 to the present are readily available and freely distributed. The cloud cover is always an issue when trying to map flood events using optical remote sensing, especially during the rising stage of a flood event. To help the reduction of cloud interference, the use of 8-day or 16-day MODIS composites (provided by NASA) has proven useful in mapping the temporal dynamics of water [80][81] (Table 6).

Table 5 SPOT technical specifications.

(source: https://apollomapping.com)

Satellite	Band	Wavelength (μm)	Pixel size (m)
SPOT 6,7	Panchromatic	0,45 - 0,745	2,2
	B0: blue	0,45 - 0,52	8,8
	B1 : green	0,53 - 0,59	
	B2 : red	0,625 - 0,695	
	B3 : near infrared	0,76 - 0,89	
SPOT 5	Panchromatic	0,48 - 0,71	2,5 or 5
	B1 : green	0,50 - 0,59	10
	B2 : red	0,61 - 0,68	
	B3 : near infrared	0,78 - 0,89	
	B4 : short wave infrared	1,58 - 1,75	20
SPOT 4	Monospectral	0,61 - 0,68	10
	B1 : green	0,50 - 0,59	20
	B2 : red	0,61 - 0,68	
	B3 : near infrared	0,78 - 0,89	
	B4 : short wave infrared	1,58 - 1,75	
SPOT 1,2,3	Panchromatic	0,51 - 0,73	10
	B1 : green	0,50 - 0,59	20
	B2 : red	0,61 - 0,68	
	B3 : near infrared	0,78 - 0,89	

Table 6 MODIS sensor spectral bands.

(source: http://modis.gsfc.nasa.gov/about/)

Band	Wavelength (μm)	Band	Wavelength (μm)	Band	Wavelength (μm)
1	0,620 - 0,670	13	0,662 - 0,672	25	4,482 - 4,549
2	0,841 - 0,876	14	0,673 - 0,683	26	1,360 - 1,390
3	0,459 - 0,479	15	0,743 - 0,753	27	6,535 - 6,895
4	0,545 - 0,565	16	0,862 - 0,877	28	7,175 - 7,475
5	0,1230 - 0,1250	17	0,890 - 0,920	29	8,400 - 8,700
6	0,1628 - 0,1652	18	0,931 - 0,941	30	9,580 - 9,880
7	0,2105 - 0,2155	19	0,915 - 0,965	31	10,780 - 11,280
8	0,405 - 0,420	20	3,660 - 3,840	32	11,770 - 12,270
9	0,438 - 0,448	21	3,929 - 3,989	33	13,185 - 13,485
10	0,483 - 0,493	22	3,929 - 3,989	34	13,485 - 13,785
11	0,526 - 0,536	23	4,020 - 4,080	35	13,785 - 14,085
12	0,546 - 0,556	24	4,433 - 4,498	36	14,085 - 14,385

On board the Terra satellite, there is also the Advanced Spaceborne Thermal Emission and Reflection Radiometer (ASTER), which provides images of Earth in 14 different bands (Table 7) from visible to thermal infrared, with a spatial resolution ranging between 15 m to 90 m. Different indexes (e.g. NDVI NDSI, NDWI) and surface temperature images produced from ASTER data before and during the floods have been used to estimate flooded areas in the daytime [82][83][84].

Among the coarse spatial resolution sensors, Advanced Very High Resolution Radiometer (AVHRR) from NOAA's series of polar-orbiting satellites (at present 9 satellites) have received considerable attention and have been extensively used to study regional, continental and global phenomena [85]. The AVHRR is a broad-band sensing in the visible, near and thermal infrared portions of the electromagnetic spectrum. It collects image with a spatial resolution of approximately of 1,1 km and it is outstanding for its temporal resolution: the NOAA satellites pass twice daily above each location [86] allowing to monitor the progress of a flood in near real-time and increasing the possibilities of getting cloud-free data. Since the early application of NOAA data for studying the 1973 flood in the Mississippi [87], many successful applications of NOAA/AVHRR data for flooded area mapping, using time series data and various indexes (e.g. NDVI and NDWI), have been reported in the literature [88][57][89][90].

Table 7 ASTER technical specifications

(source: https://asterweb.jpl.nasa.gov/)

Band	Wavelength (μm)	Pixel size (m)	Description
VNIR_Band1	0,520–0,600	15	Visible green/yellow
VNIR_Band2	0,630–0,690		Visible red
VNIR_Band3N	0,760–0,860		Near infrared
VNIR_Band3B	0,760–0,860		
SWIR_Band4	1,600–1,700	30	Short-wave infrared
SWIR_Band5	2,145–2,185		
SWIR_Band6	2,185–2,225		
SWIR_Band7	2,235–2,285		
SWIR_Band8	2,295–2,365		
SWIR_Band9	2,360–2,430		
TIR_Band10	8,125–8,475	90	Long-wave infrared or thermal IR
TIR_Band11	8,475–8,825		
TIR_Band12	8,925–9,275		
TIR_Band13	10,250–10,950		
TIR_Band14	10,950–11,650		

Table 8 NOOA/AVHRR sensors spectral range

(source: http://edc2.usgs.gov/1KM/avhrr_sensor.php)

Band	Wavelength (μm)		
	NOAA-6,8,10	**NOAA-7,9,11,12,14**	**NOAA-15,16,17,18,19**
1	0,58 - 0,68	0,58 - 0,68	0,58 - 0,68
2	0,725 - 1,10	0,725 - 1,10	0,725 - 1,10
3A	x	x	1,58-1,64
3B	3,55 - 3,93	3,55 - 3,93	3,55 - 3,93
4	10,50 - 11,50	10,3 - 11,3	10,50 - 11,50
5	band 4 repeated	11,5 - 12,5	11,5 - 12,5

Relatively few works have used very high-resolution optical sensors (e.g. IKONOS, QuickBird, WorldView, GeoEye, etc.) to study flooding [91][92][93]. The high costs may still be a limitation for obtaining very high resolution images, especially for multiple dates after the occurrence of main triggering events; therefore, the use of very high resolution images have not been very popular yet for flood mapping. However, products from these images have been used to assess the post-flood damage and recovery effort [29][94].

Microwave remote sensing (wavelength 0,75 - 30 cm) provides valuable information for flood mapping and monitoring not only because the data acquisition is

independent of daytime and weather conditions, but also for the high backscatter contrast that exists between water and other cover classes [55]. Water bodies act as a mirror-reflecting surface, their response is low (low backscatter) and then looks like a dark area. The earth, for its part, gives a much greater amount of radar energy due for example to the surface roughness and this generates the high contrast between soil surfaces and water [95].

In Table 9 The characteristics of some SAR satellite used for flood detection and monitoring are shown [96][97][98][99][100].

Table 9 Characteristics of some SAR satellite

Satellite	Launch (End of service)	Band	Wavelength (cm)	Spatial resolution (m)	Repeat cycle (days)
RADARSAT-1/RADARSAT-2	1995/2007 (2013)	C Band	5,6	8-100/1-100	24
ERS-1/ERS-2	1991/1995 (2000/2011)	C Band	5,6	30	35
Envisat	2002 (2012)	C Band	5,6	30	35
Sentinel-1A/Sentinel1B	2014/2016	C Band	5,5	5-100	12
Cosmo-SkyMed	2007/2008	X Band	3,1	1-30	16
TerraSAR-X/TanDEM-X	2007/2010	X Band	3,1	1-18	11
ALOS-PALSAR	2006 (2011)	L Band	23,6	7-100	46

Various SAR data have been used and tested to map the flood extent in versatile environments. A few techniques have been proposed in literature to obtain flood maps or to be used as a support to photo interpretation. Appropriate colour compositions are able to enhance the changes occurred in a multitemporal sequence, so as to locate and qualitatively evaluate flooded and non-flooded areas. The same region's multi-date SAR scenes can be projected to red, green and blue channels in producing a colour composite that can effectively show the progress of an inundation during a particular time period. This technique is quite easy to carry out and it gives a chance to readily detect those areas that remains water logged for a maximum time period [101].

For mapping the extent of flooded areas using SAR data and to provide a quantitative result classification, change-detection and segmentation methods must be used to take the contextual spatial arrangements of pixels into account [102]. Thresholding is one of the most commonly adopted methods to discriminate

between flooded and non-flooded areas [101][103][104]. This approach is founded on the low radar return from smooth open water bodies that behave as specular reflectors, but it does not provide satisfactory results in vegetated, forested and urban areas or in the presence of wind that roughens the water surface. Its advantage is represented by the computation efficiency that could make it suitable for rapid mapping purposes [105]. However, the choice of the threshold value is a critical aspect and it depends on environmental characteristics of the study area (e.g. land cover), as well as on system parameters (frequency band, polarization and observation angle) [106].

The coherence and amplitude change detection capabilities of SAR are generally exploited by using two images acquired pre and post the event [107][108]. The amplitude approach classifies as flooded the areas where the backscattering coefficient of the second image is considerably decreased with respect to first one [55]; therefore, the choice of the threshold values is again crucial. Techniques based on the coherence generally mark as inundated the areas where the coherence between the two images is very low [109]. Algorithms founded on segmentation techniques were also developed to delineate the boundaries of an inundated area [42][110][111].

The most common problem in identifying flood extent from SAR images is associated with the relation between radar wavelength and roughness of the terrain and water body [112]. Normally, pure and calm water acts as a specular reflector to the radar signals thus the radar antenna receives no backscatter and the water appears in dark tone in the images. The appearance of the rough water surface is brighter than the appearance of the calm water. During floods, bad and windy condition usually prevails over the affected area. Wind induced ripples in the water surface frequently creates problems for the interpreter to determine the threshold value to delineate the flooded area [101]. Forest cover also poses an obstacle to accurately identify inundated areas from a SAR image. If vegetation emerges from the water surface or when detecting flooded forests, the observed surfaces may appear bright in SAR images because of the enhancement of the double bounce effect involving the floodwater and any vertical structure. The

situation can be even more complicated in flooded urban areas, where both specular and multiple reflections of the radar energy may occur [112]. In mountains, slopes positioned perpendicular to the radar beam only appear bright and all other areas appear as dark or shaded. This fact can constitute a problem in identifying the flooded areas in the mountains: due to its shaded appearance, it is very common to erroneously identify the mountainous areas as inundated [113].

Optical data contain information on the reflective and emissive characteristics of the targets in terms of spectral intensity. This spectral information is related to the chemical composition and moisture content of the observed target. On the other hand, SAR data contain information on the geometric structure, surface roughness and dielectric properties of natural and man-made objects [114]. Therefore, a wide spectrum of data can be available for the same observed scene.

The integration of microwave and optical sensors may provide complementary data for a better understanding of the observed surface, by decreasing the uncertainty related to the single source and producing more detailed information than each of the component considered alone [115].

In recent years, flood mapping efforts synthesize the advantages of both optical and microwave remote sensing technologies for better results and accuracy [116][117]. Optical and SAR image fusion has been performed at three different processing levels: pixel level, feature level and decision level, using a wide variety of techniques [118]. *Yonghua et al*. (2007) used the principal components analysis and the intensity, hue and saturation method for Landsat ETM+ infrared bands and Radarsat data fusion, in order to extract flooded areas and water bodies [119]. For the same purpose, *Dey et al.* (2008) provided a decision fusion approach for combing classification results from Radarsat and Landsat ETM+ [120]. A similar flood mapping approach was presented by *Kuehn et al*. (2002) using the object oriented technology for the fusion of individual classification of SAR and ASTER images [121].

Although studies and techniques related to the multi-sensor analysis are numerous, the use of data acquired by different sensors is not straight forward and often requires iterative experiments to obtain at an optimal result.

2.2 Case of study: flood prone area in Dhaka district (Bangladesh)

Due to the increase in world population and the progressive development of national economies from merely agricultural systems, many cities have been undergoing a rapid and often uncontrolled growth. The conversion of arable land into urban areas, the destruction of habitats and the decrease of spontaneous vegetation cover are the main consequences of the urban sprawl. In the last few decades, land use/cover changes, due to human activities, occurred more rapidly in developing countries than in the developed world. Like other developing countries, Bangladesh has been experiencing rapid urbanization and Dhaka, its capital, is expected to grow by 2020 to more than 50 times its size in 1950 [122]. In fact, in recent decades a rapid increase in urban population has occurred in Dhaka, 6,6 million people in 1990 and 16,9 in 2014. The rural-urban migration has significantly contributed to this growth; the city's population is growing by 1400 new arrivals a day [7] and it is estimated that in 2030 Dhaka will have almost 27,4 million of inhabitants [6]. Unfortunately, the absence of an appropriate urban planning has been further contributing to an urban sprawl, resulting in widespread environmental problems throughout the city [123]. The increase in impervious surfaces, resulting from the rapid and uncontrolled urbanization, is not only threatening the agricultural land but also the local watershed, damaging and reducing the local water resources and exacerbating the impacts of water flows during the monsoon season, that typically affects the territory from May to October. Moreover, most parts of Dhaka city have already been occupied. As a result, new areas are being reclaimed by both government and private agencies. In many cases, the practice for developing these new areas is just to fill lowlands (i.e., ditches, lakes etc.) with dredged material; therefore, silty sand collected from riverbed and riverbank are pumped and transferred to the point of deposition [124][125] (Figure 8).

Due to the high pressure on urban space, many flood-vulnerable urban fringe areas have been overcrowded by squatter settlements which lack most of the effective flood-proofing devices and alleviation measures [126] (Figure 9).

In this kind of context, satellite images can support the monitoring of highly dynamic phenomena related both natural events and to anthropogenic aspects, which are difficult to assess on a large scale in a different way. The contribute of multi-temporal Landsat images for mapping and monitoring flood prone areas in Dhaka district and for detecting the impact of urbanization and land use/cover changes on surface water system is described in the later sections.

Figure 8 Barges pump sand from the river bed to be distributed across lowlands (left); The Pink City an example of new built-up area in the East of Dhaka (right).

(source: http://www.kierantimberlake.com/files/pages/262/sandfill-2.jpg; http://static.panoramio.com/photos/large/61130031.jpg)

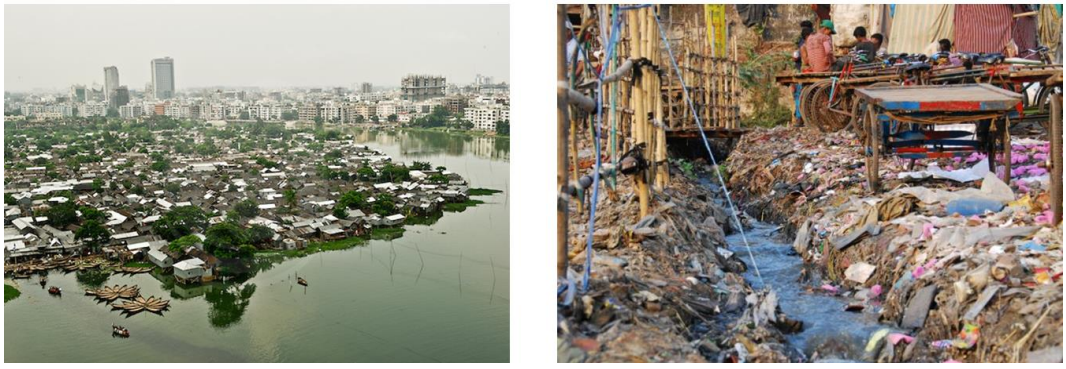

Figure 9 Korial the largest slum in Dhaka (left); Raw sewage drains from slum neighbourhood directly onto the trash-strewn banks of the Buriganga River (right).

(source: http://rippleeffectimages.photoshelter.com/img/pixel.gif; http://www.cbsnews.com/news/dhaka-bangladesh-fastest-growing-city-in-the-world/)

2.2.1 The study area

Regionally, the study area is located in the center of Bangladesh between 23°54'7''N, 90°18'28''E and 23°39'38''N, 90°31'32''E. It covers about 591 km^2 and includes Dhaka, the capital of Bangladesh (Figure 10). Dhaka lies in sub-tropical

monsoon zone under humid climatic condition. The city experienced about 2.000 mm annual rainfall, of which, more than 80% occurs during the monsoon season from May to October [127]. Dhaka is situated on an alluvial terrace, called Modhupur, and it is surrounded by the Tongi Canal to the North, the Buriganga River to the South, the Balu River to the East and the Turag River to the West. The surface elevation of this area ranges from 0,5 to 12 m. Therefore, these lowlands, which serve as detention basin, with the occurrence of heavy monsoon rains, make the territory severely exposed to flooding [128].

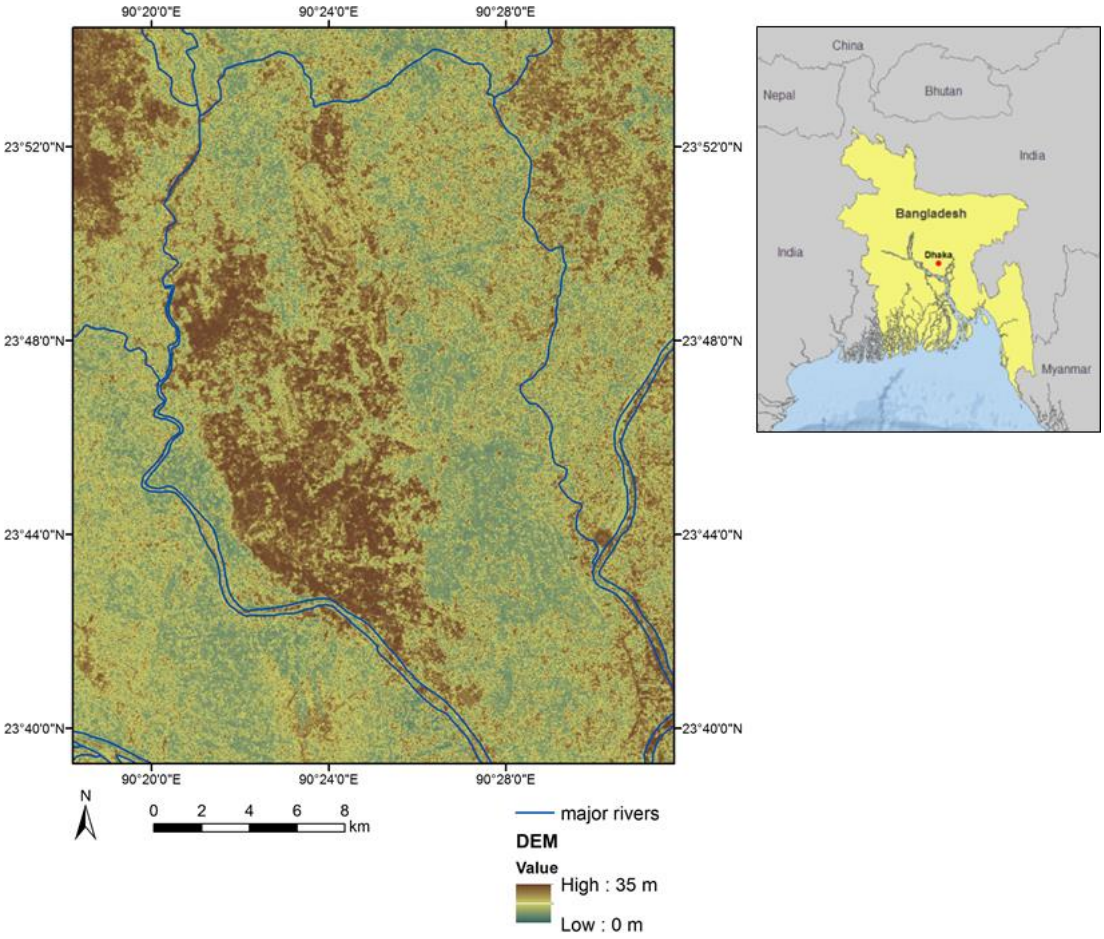

Figure 10 The study area in Dhaka district (Bangladesh).

2.2.2 Data and methodology

A Landsat time-series was processed by means of per-pixel classification in order to analyse the evolution of the study area during an ordinary monsoon season and to investigate the impacts induced by the urban growth on the surface water system. Post-classification change detection approach was then performed to compare the

multitemporal land use/cover maps thus to quantify the flooded areas and long term changes of water system.

2.2.2.1 Data collection

For mapping routinely flooded areas during an ordinary monsoon season, a Landsat image acquired in October 2009 (post-monsoon) was collected and then compared with two images of 2010, of January and February respectively, which show the territory three/four months after flooding. In order to evaluate and monitor long term changes on surface water system due to the urban growth and land use/cover changes, three Landsat images of 2000, 2009 and 2013 were used. For this purpose, images acquired in November/October, when the side effects of the monsoon rains are more evident, were chosen (Table 10).

These five images were chosen among the available time-series with limited cloud-cover from the free Landsat Archive [129]. In addition, geospatial information provided by ITHACA [49] were used; they include land use map, administrative subdivisions (*Thana*) and major rivers. These data, referred to the local geodetic system Everest_Adj_1937, were projected in UTM-WGS 84, to allow the comparison with satellite images.

Table 10 List of the collected satellite images and their specific employment.

Date	Satellite	Sensor	Resolution	Product level	Application
26.11.2000	Landsat7	ETM+	30 m	1T	land use/cover changes impact on water system
26.10.2009	Landsat5	TM	30 m	1T	monitoring ordinary flood land use/cover changes impact on water system
30.01.2010	Landsat5	TM	30 m	1T	monitoring ordinary flood
15.02.2010	Landsat5	TM	30 m	1T	monitoring ordinary flood
06.11.2013	Landsat8	OLI	30 m	1T	land use/cover changes impact on water system

2.2.2.2 Image processing

The Landsat L1T products consist of geometrically corrected images, which are coherent each other, being orthorectified by the same dataset (GLS2000). The multispectral bands were calibrated to Top Of Atmosphere (TOA) reflectance, while TIR bands were calibrated to radiance and then normalized in respect to the

maximum value. The size of a Landsat scene is 170 km x 185 km, therefore all the images were cropped on the study area.

All the images were processed independently of each other using the pixel-based classification using maximum likelihood with a threshold equal to 0,95 in order to produce land use/cover maps (Figure 11).

The training samples or Region Of Interest (ROI) for the classification were derived only from the classified image itself therefore the atmospheric correction was unnecessary [130][131]. The thermal band of Landsat imagery was included in the classification process [132], because it was able to improve the separability of the classes in the investigated area, as demonstrated by the ROI separability indexes showed in Table 12; for each class-row the first line of the table reports the separability indexes using only the six TM multispectral bands, whereas the second line (grey) shows the same indexes computed on the six multispectral bands plus the thermal band 6.

Seven basic informative classes were identified by photointerpretation and spectral profile analyses, and for each one some training sites were selected. In Table 11 these classes are described and the training sites used for each classification are listed. The images of 2010, acquired far from monsoon season, show no flooded areas, thus Water_1 and Water_2 classes were replaced with a single one, called Water, which represents the permanent water bodies in the study area.

The image processing was performed using ENVI 5.2 software [133].

Table 11 Description of the informative classes adopted for land use/cover maps and training sites used for each classification.

Class	Description	Training sites for each image				
		26.11.2000	26.10.2009	30.01.2010	15.02.2010	06.11.2013
Build up	Urban areas, buildings, roads, slum, airports etc.	16/628	18/753	18/753	18/797	17/719
Bare soil	Excavation areas, filled area, exposed soil.	7/337	16/643	17/659	17/659	20/444
Vegetation	Deep vegetated areas (deciduous, coniferous, palm forests, etc.).	9/533	16/643	12/524	14/569	11/458
Cultivated land	Agricultural areas, fallow lands and crop fields.	7/526	11/688	9/551	11/613	8/407
Water_1	Water with suspended solids and sediment transport (river, creeks, flooded areas).	12/618	15/550	-	-	14/426
Water_2	Water in contact with vegetation (irrigation ditches, lakes, flooded vegetated areas).	22/713	16/602	-	-	20/413
Water	Permanent water bodies (river, creeks, ditches, lakes)	-	-	23/629	25/639	-
Wetland/ lowland	Low and wet areas, periodically flooded areas.	-	-	16/461	14/436	-
		n polygons/n pixels				

Table 12 Example of ROI separability indexes for Landsat of October 2009 using only the six TM multispectral bands and computed on the six multispectral bands plus the thermal band.

	Build up	Bare soil	Vegetation	Cultivated land	Water_1	Water_2
Build-up		1,85191006	1,99991367	1,98393738	1,98685897	1,99999834
	(+thermal)	1,86720849	1,99993167	1,99062438	1,98894909	1,99999999
Bare soil			1,99994757	1,81527047	1,99944104	1,99995637
		(+thermal)	1,99996853	1,94384719	1,99946876	1,99997308
Vegetation				1,84188508	1,99998385	1,99999186
			(+thermal)	1,85958818	1,99998703	1,99999778
Cultivated land					1,99994127	1,99999999
				(+thermal)	1,99998389	2,00000000
Water_1						1,82833533
					(+thermal)	1,88551565

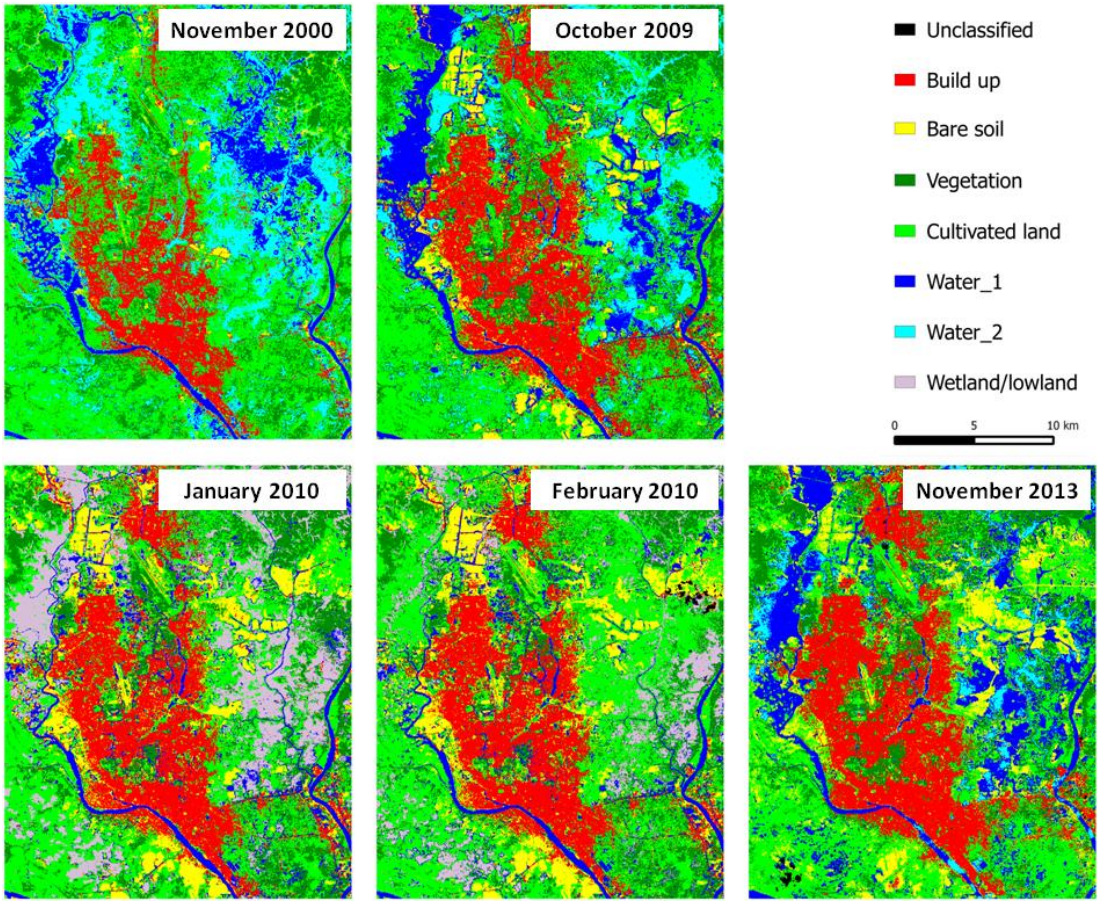

Figure 11 Multi-temporal land use/cover map of Dhaka district.

2.2.2.3 Accuracy assessment: map validation

Ground truth data were not available for the study area, therefore a rigorous validation was not possible. However, for a first assessment of the classification accuracy, a number of check points was identified on the Landsat images and their land cover class was verified by photointerpretation of high-resolution colour images (Figure 12). In particular, for each class, about one hundred ground truth points were selected and the confusion matrixes were compiled.

The high-resolution images have been available since 2001 and they have covered the entire study area only since 2004. Therefore, the 2000 map validation was not possible. For all the other an accuracy higher than 90% was achieved (Table 13,Table 14, Table 15, Table 16).

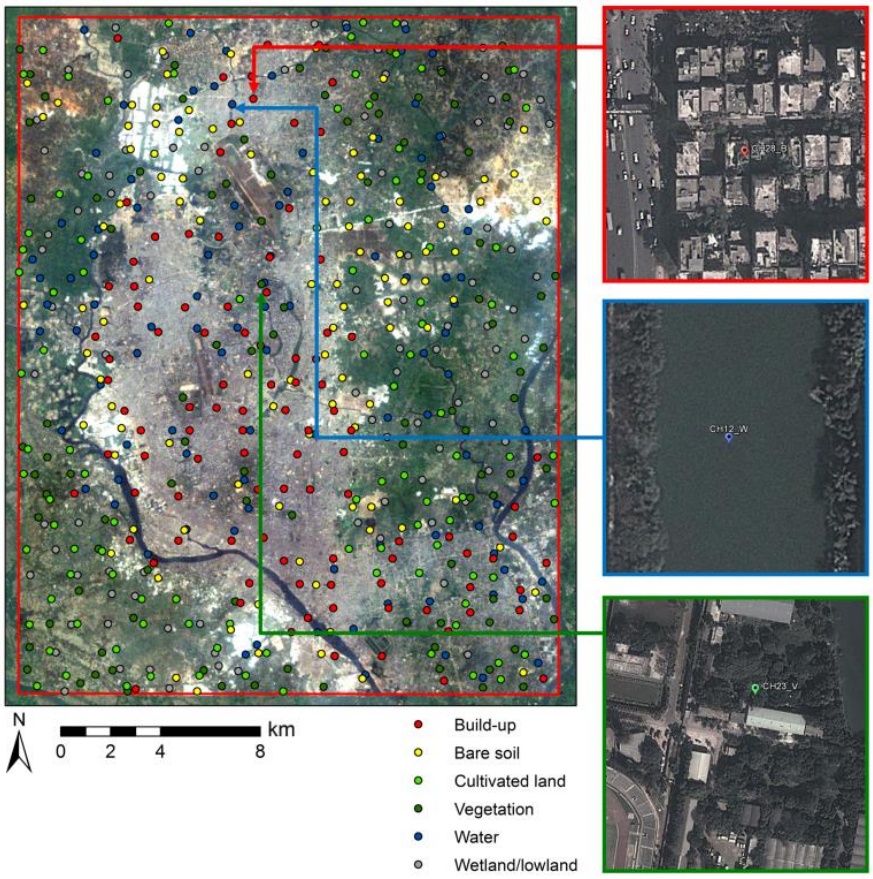

Figure 12 Ground truth points in February Landsat image (left); three examples extracted from high resolution images (right).

Table 13 Confusion matrix for 26-10-2009 map.

26-10-2009	**Ground Truth (Pixels)**					
Class	Build up	Bare soil	Vegetation	Cultivated land	Water	**Total**
Unclassified	0	1	0	0	0	1
Build up	102	5	0	0	4	111
Bare soil	0	94	0	0	0	94
Vegetation	2	0	96	2	4	104
Cultivated land	3	1	6	101	2	113
Water	3	0	1	0	93	97
Total	110	101	103	103	103	520
Overall Accuracy	(486/520)	93,46%				
Kappa Coefficient	0,918					

Class	**Commission (Pixels)**	**Omission (Pixels)**	**Prod. Acc. (Pixels)**	**User Acc. (Pixels)**
Build up	9/111	8/110	102/110	102/111
Bare soil	0/94	7/101	94/101	94/94
Vegetation	8/104	7/103	96/103	96/104
Cultivated land	12/113	2/103	101/103	101/113
Water	4/97	10/103	93/103	93/97

Table 14 Confusion matrix for 30-01-2010 map.

30-01-2010	Ground Truth (Pixels)						
Class	Build up	Bare soil	Vegetation	Cultivated land	Water	Wetland/lowland	**Total**
Unclassified	0	0	0	0	0	0	0
Build up	99	5	0	0	3	2	109
Bare soil	0	99	0	0	0	0	99
Vegetation	2	0	100	3	3	0	108
Cultivated land	3	0	4	99	0	1	107
Water	3	0	1	0	89	8	101
Wetland/lowland	0	0	0	0	6	91	97
Total	107	104	105	102	101	102	621
Overall Accuracy	(577/621)	92,91%					
Kappa Coefficient	0,915						

Class	Commission (Pixels)	Omission (Pixels)	Prod. Acc. (Pixels)	User Acc. (Pixels)
Build up	10/109	8/107	99/107	99/109
Bare soil	0/99	5/104	99/104	99/99
Vegetation	8/108	5/105	100/105	100/108
Cultivated land	8/107	3/102	99/102	99/107
Water	12/101	12/101	89/101	89/101
Wetland/lowland	6/97	11/102	91/102	91/97

Table 15 Confusion matrix for 15-02-2010 map.

15-02-2010	Ground Truth (Pixels)						
Class	Build up	Bare soil	Vegetation	Cultivated land	Water	Wetland/lowland	**Total**
Unclassified	0	0	0	0	0	0	0
Build up	86	1	0	0	3	2	92
Bare soil	2	100	0	0	0	0	102
Vegetation	4	0	89	3	3	1	100
Cultivated land	7	0	6	94	2	2	111
Water	1	0	1	0	84	7	93
Wetland/lowland	0	0	1	1	6	83	91
Total	100	101	97	98	98	95	589
Overall Accuracy	(536/589)	91,00%					
Kappa Coefficient	0,892						

Class	Commission (Pixels)	Omission (Pixels)	Prod. Acc. (Pixels)	User Acc. (Pixels)
Build up	6/92	14/100	86/100	86/92
Bare soil	2/102	1/101	100/101	100/102
Vegetation	11/100	8/97	89/97	89/100
Cultivated land	17/111	4/98	94/98	94/111
Water	9/93	14/98	84/98	84/93
Wetland/lowland	8/91	12/95	83/95	83/91

Table 16 Confusion matrix for 06-11-2013 map.

06-11-2013	Ground Truth (Pixels)					
Class	Build up	Bare soil	Vegetation	Cultivated land	Water	**Total**
Unclassified	0	0	0	0	0	0
Build up	97	4	0	0	5	106
Bare soil	2	96	0	0	0	98
Vegetation	4	0	91	4	2	101
Cultivated land	4	0	7	90	2	103
Water	4	0	0	0	92	96
Total	111	100	98	94	101	504
Overall Accuracy	(466/504)	92,46%				
Kappa Coefficient	0,9057					

Class	**Commission (Pixels)**	**Omission (Pixels)**	**Prod. Acc. (Pixels)**	**User Acc. (Pixels)**
Build up	9/106	14/111	97/111	97/106
Bare soil	2/98	4/100	96/100	96/98
Vegetation	10/101	7/98	91/98	91/101
Cultivated land	13/103	4/94	90/94	90/103
Water	4/96	9/101	92/101	92/96

From the confusion matrix, some observations about the errors affecting the classification come out. Commission errors were outlined between Vegetation and Cultivated classes and they are probably due to a similar spectral pattern of trees or plants and certain plantations. A similar situation occurs in the 2010 maps for Water and Wetland/lowland classes.

Isolated houses in dense vegetated areas or small canals running through built-up areas or extensive cultivated land were not detected, because of the spatial resolution of Landsat images.

Commission errors affects the Bare soil class; in particular, in correspondence of sandy or clayey material saturated with water (river banks or filling material in contact with water), the classifier incorrectly detects urban areas. This can be explained considering that the aggregate on the river banks and mixtures of sand clay and water are used to produce bricks or as construction material in the slum shacks. Therefore, the error resulting from the confusion between Bare soil and Build-up classes depends on the impossibility to distinguish between very similar materials that have almost coincident spectral characteristics (Figure 13). The same

problem occurs for Water and Wetland/lowland classes at low water levels with a sandy bottom.

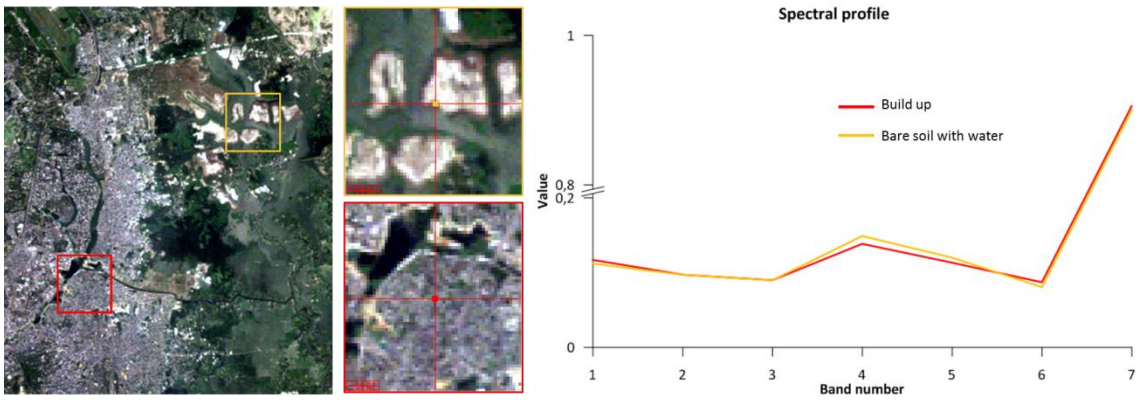

Figure 13 Spectral profile comparison between pixels belonging to filling material in contact with water (yellow) and urban areas (red).

2.2.3 Results

The maps of Dhaka district, obtained from the classification of the Landsat images, were compared through change detection analyses for mapping systematically flooded areas due to the monsoon rains and for evaluating the impacts of the rapid urban growth on the surface water system. For the change detection purpose, water classes were merged into a single class.

2.2.3.1 Ordinary monsoon season flooding

Comparing post-monsoon map of October 2009 with January and February 2010 maps, the water bodies which are permanently present in the area and the areas routinely flooded during the monsoon season were identified and quantified.

In the three classified maps, pixels belonging to Water class were isolated and coloured respectively in red, green and blue in a new combined representation (Figure 14). In the generated image, permanent water bodies appear in white colour because the corresponding pixels are classified as water in all the three maps. The flooded areas were identified by subtracting the permanent water bodies from the Water class of October 2009 in GIS environment. To verify the correctness of the procedure, the obtained data related to water bodies were compared with the vector map of the major rivers. In particular, the water bodies

always present in the territory occupy 27,2 km^2, whereas the flooding affects 115 km^2.

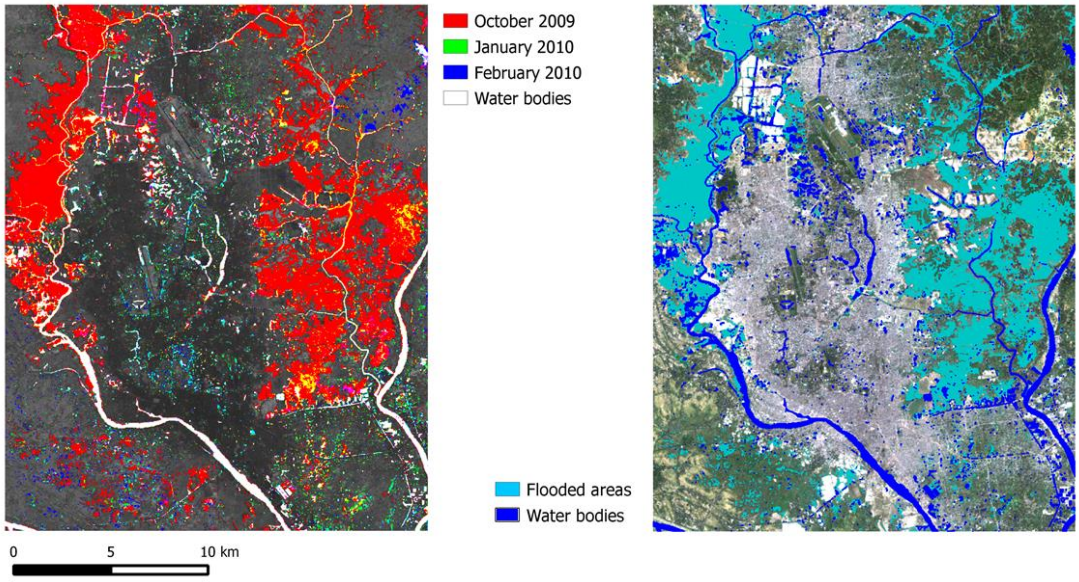

Figure 14 Overlapping of the Water class pixels in the three Landsat maps (October 2009, January 2010 and February 2010) combined in a RGB composition (left); the resulting permanent water bodies and flooded areas (right).

Through the comparison between the 2009 map and the two subsequent maps of 2010, the evolution of flooding was also investigated. In October, Water class (water bodies and flooding) covers about 142 km^2 of the studied area. Between October and January, Water class is reduced by 89,3 km^2 (Table 17), leaving space mainly to cultivated fields (17,1 km^2) and large wetlands (65,3 km^2) (Figure 15). Between October and February, the Water class recession is equal to 96 km^2 (Table 18). Even in this case, the space occupied by the flooding is replaced by wetlands and fields but in different proportions. Compared to October-January period, the cultivated fields increased (46,7 km^2) and wetland decreased (33,3 km^2) (Figure 15). Therefore, after four months, the flooded areas in October appear as areas of intense agricultural activity; they are extensive cultivations of boro rice, identified combining the land use data provided by ITHACA (Figure 16). In fact, the exploitation of naturally flooded areas for rice cultivation is a common practice in Bangladesh [134].

Table 17 October 2009 - January 2010 land use/cover changes matrix (km^2).

		October 2009							
		Build up	Bare soil	Vegetation	Cultivated land	Water	Wetland/ lowland	Unclass.	Total
January 2010	Unclass.	0,0	0,0	0,0	0,1	0,0	0,0	0,1	0,2
	Build up	90,2	5,5	2,0	6,4	5,9	0,0	0,0	110,0
	Bare soil	6,9	28,1	2,5	23,8	3,8	0,0	0,3	65,4
	Vegetation	1,3	0,5	55,1	31,3	7,4	0,0	0,0	95,6
	Cultivated land	10,6	3,0	15,4	122,9	21,9	0,0	0,1	173,9
	Water	1,9	0,8	7,5	4,8	38,0	0,0	0,0	**53,0**
	Wetland/lowland	0,2	0,8	9,3	17,6	65,3	0,0	0,0	93,1
	Total	111,2	38,7	91,7	206,9	**142,2**	0,0	0,5	
	Class Changes	21,0	10,6	36,6	84,0	104,2	0,0	0,4	
	Image Diff.	-1,1	26,7	3,9	-33,1	**-89,3**	0,0	-0,3	

Table 18 October 2009 - February 2010 land use/cover changes matrix (km^2).

		October 2009							
		Build up	Bare soil	Vegetation	Cultivated land	Water	Wetland/ lowland	Unclass.	Total
February 2010	Unclass.	0,0	0,2	0,2	0,6	0,3	0,0	0,0	1,4
	Build up	88,2	6,0	1,8	5,5	4,3	0,0	0,1	105,8
	Bare soil	7,6	26,6	2,5	28,2	4,4	0,0	0,3	69,7
	Vegetation	3,7	1,0	50,4	30,8	15,6	0,0	0,0	101,5
	Cultivated land	10,1	3,8	23,8	124,0	52,2	0,0	0,1	213,9
	Water	1,5	0,8	6,4	5,5	32,0	0,0	0,0	**46,2**
	Wetland/lowland	0,1	0,4	6,5	12,4	33,3	0,0	0,0	52,7
	Total	111,2	38,7	91,7	206,9	**142,2**	0,0	0,5	
	Class Changes	23,0	12,1	41,3	83,0	110,2	0,0	0,5	
	Image Diff.	-5,4	31,0	9,8	7,0	**-96,0**	0,0	0,9	

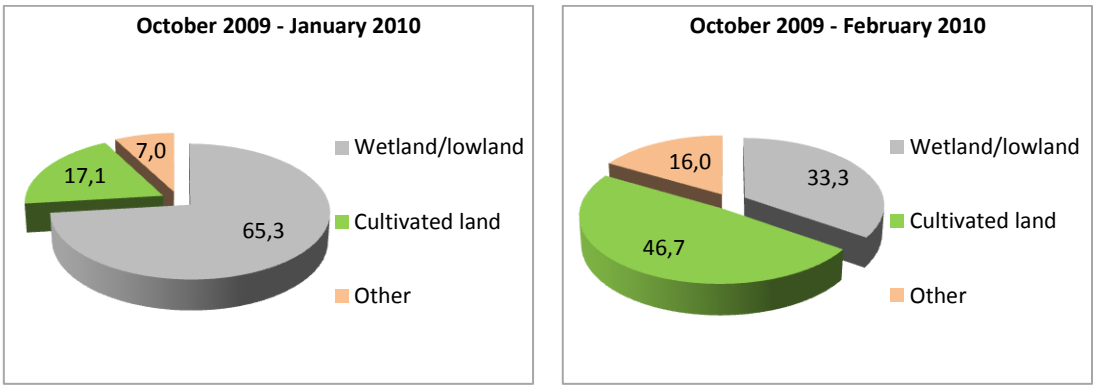

Figure 15 Water class reduction (km^2) between October and January (left) and between October and February (right).

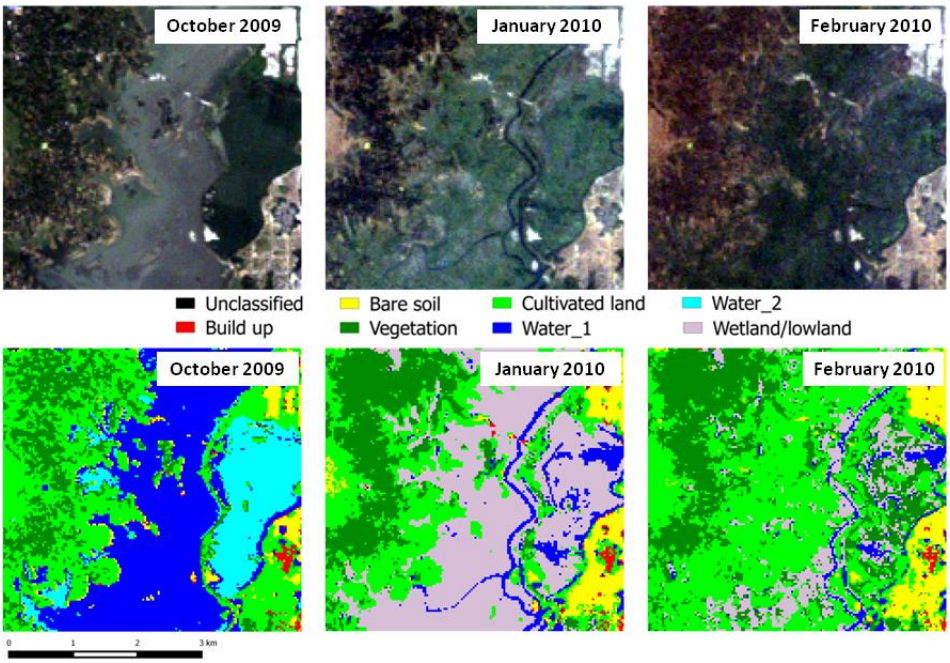

Figure 16 A portion of the Dhaka district classifications showing widespread flooding in October 2009, becoming wetland in January and cultivated land in February 2010.

2.2.3.2 Long term monitoring of the Dhaka district surface water system

To evaluate the impacts of the urbanization and the land use/cover conversion on the water system, land use transition matrixes were performed comparing 2000, 2009 and 2013 maps (Table 19, Table 20, Table 21). From this comparison the pronounced increase of built-up areas and areas taken up by bare soil was observed. Vegetated areas remained almost unchanged, whereas water areas and cultivated lands experienced a reduction (Table 22 and Figure 17).

Table 19 Land use/cover change matrix (km^2) between the 2000 and 2009 maps.

		2000						
		Build up	Bare soil	Vegetation	Cultivated land	Water	Unclass.	Total
2009	Unclass.	0,0	0,0	0,1	0,2	0,1	0,0	0,5
	Build up	60,1	2,6	4,5	38,0	5,9	0,0	111,2
	Bare soil	4,2	2,8	2,0	13,1	16,7	0,0	38,7
	Vegetation	1,9	0,8	46,9	33,0	9,1	0,0	91,7
	Cultivated land	5,5	6,2	37,1	127,8	30,3	0,1	206,9
	Water	3,2	1,7	4,8	19,9	112,6	0,0	142,2
	Total	74,8	14,1	95,4	232,0	174,7	0,2	
	Class Changes	14,7	11,3	48,5	104,2	62,1	0,2	
	Image Diff.	36,3	24,6	-3,7	-25,0	-32,5	0,3	

Table 20 Land use/cover change matrix (km^2) between the 2009 and 2013 maps.

		2009						
		Build up	Bare soil	Vegetation	Cultivated land	Water	Unclass.	Total
2013	Unclass.	0,2	0,3	0,1	1,0	0,2	0,2	2,1
	Build up	93,7	7,4	2,4	11,8	3,5	0,0	118,8
	Bare soil	4,5	15,2	5,0	25,7	16,0	0,1	66,4
	Vegetation	3,9	1,0	53,4	31,1	2,5	0,0	91,8
	Cultivated land	8,2	13,9	23,4	122,2	23,7	0,1	191,4
	Water	0,6	1,0	7,5	15,1	96,4	0,0	120,6
	Total	111,2	38,7	91,7	206,9	142,2	0,5	
	Class Changes	17,5	23,5	38,3	84,8	45,8	0,3	
	Image Diff.	7,7	27,7	0,2	-15,5	-21,6	1,6	

Table 21 Land use/cover change matrix (km^2) between the 2000 and 2013 maps.

		2000						
		Build up	Bare soil	Vegetation	Cultivated land	Water	Unclass.	Total
2013	Unclass.	0,2	0,1	0,2	1,2	0,4	0,0	2,1
	Build up	62,8	3,6	5,0	40,9	6,5	0,0	118,8
	Bare soil	3,3	2,9	6,4	25,8	28,0	0,0	66,4
	Vegetation	2,0	0,7	46,7	37,5	4,9	0,0	91,8
	Cultivated land	4,9	5,3	31,6	108,2	41,4	0,1	191,4
	Water	1,6	1,5	5,5	18,5	93,5	0,0	120,6
	Total	74,8	14,1	95,4	232,0	174,7	0,2	
	Class Changes	12,0	11,2	48,7	123,8	81,2	0,2	
	Image Diff.	44,0	52,3	-3,6	-40,5	-54,1	1,9	

Table 22 Summary of land use/cover type areas for 2000, 2009 and 2013 and land use/cover change between 2000-2009 and 2009-2013.

Class	2000		2009		2013		Land use/cover change (km^2)		Total changes (km^2)
	Area (km^2)	% of total land	Area (km^2)	% of total land	Area (km^2)	% of total land	2000-2009	2009-2013	2000-2013
Unclass.	0,2	0,0	0,5	0,1	2,1	0,3	0,3	1,6	1,9
Build up	74,8	12,7	111,2	18,8	118,8	20,1	36,3	7,7	44,0
Bare soil	14,1	2,4	38,7	6,5	66,4	11,2	24,6	27,7	52,3
Vegetation	95,4	16,1	91,7	15,5	91,8	15,5	-3,7	0,1	-3,6
Cultivated land	232,0	39,2	206,9	35,0	191,4	32,4	-25,0	-15,5	-40,5
Water	174,7	29,6	142,2	24,1	120,6	20,4	-32,5	-21,6	-54,1
Total	591,2	100,0	591,2	100,0	591,2	100,0			

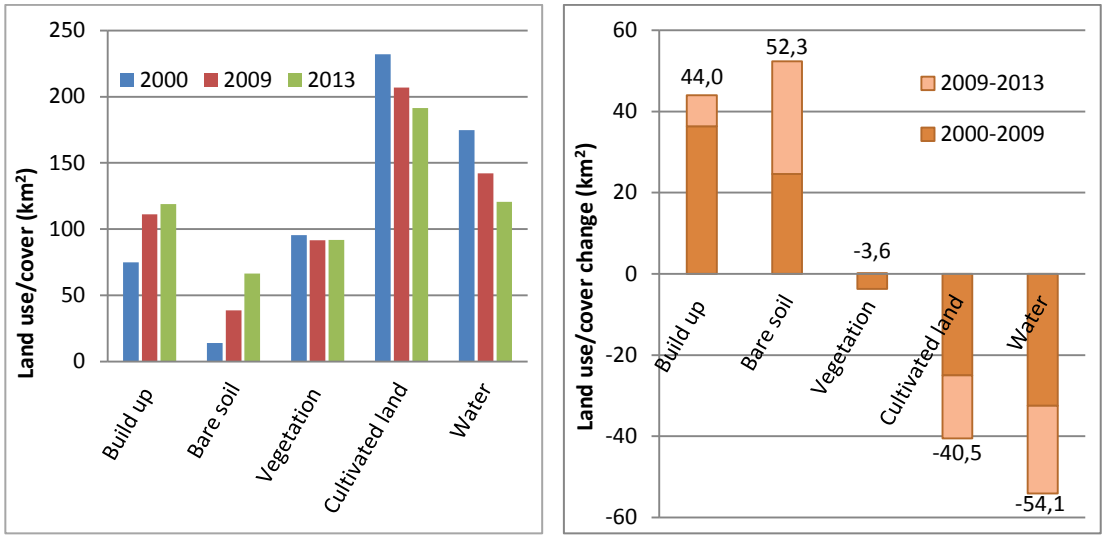

Figure 17 Land use/cover type areas for 2000, 2009 and 2013 (left) and total land use/cover changes (right).

During 2000-2009 period Build-up class increased approximately by 49%, from 74,8 km^2 to 111,2 km^2, and Bare soil class grew more than double, from 14,1 km^2 to 38,7 km^2. In the years 2009-2013, while the growth of built-up areas was moderate (7,7 km^2), just in four years the surface occupied by bare soil increased from 38,7 km^2 to 66,4 km^2 with a similar trend recorded in the decade 2000-2009. Simultaneously, the reduction of cultivated field equal to 25 km^2 and 15,5 km^2 was observed between 2000-2009 and 2009-2013 respectively. Furthermore, the Water class decreased by 32,5 km^2 and 21,6 km^2 in the two time intervals investigated (Figure 17).

The analysis of land use/cover conversion matrixes revealed that the urban growth is the main cause of the reduction of cultivated areas. In fact, Build up class increased by 44 km^2 between 2000-2013 and the 82% of them (36 km^2) were composed by cultivated fields in 2000.The increase of bare soil was mostly due to the development of new areas created filling low land with aggregate extracted from riverbed and riverbank. In particular, these expansions encroached systematically flooded areas and cultivated fields; in the period 2000-2013 Bare soil class increased by 52,3 km^2, of which the 51% (26,5 km^2) and the 39% (20,5 km^2) respectively came from Water and Cultivated Land classes (Figure 18 and Figure 19). The results obtained by means of change detection analysis revealed the high increasing of the urbanization rate which is the main cause of the agricultural land

reduction; moreover, the achieved statistics confirmed that most parts of Dhaka city have already been occupied; therefore, to satisfy the requests of new constructing areas, especially by government and private agencies, the topography of large zones in city outskirts was modified. From the multitemporal land use/cover maps comparison it was possible to verify that this practice is performed filling with aggregate material flood prone lowlands and cultivated fields. This is also confirmed by the large increase of Bare soil class recorded for the period 2000-2013.

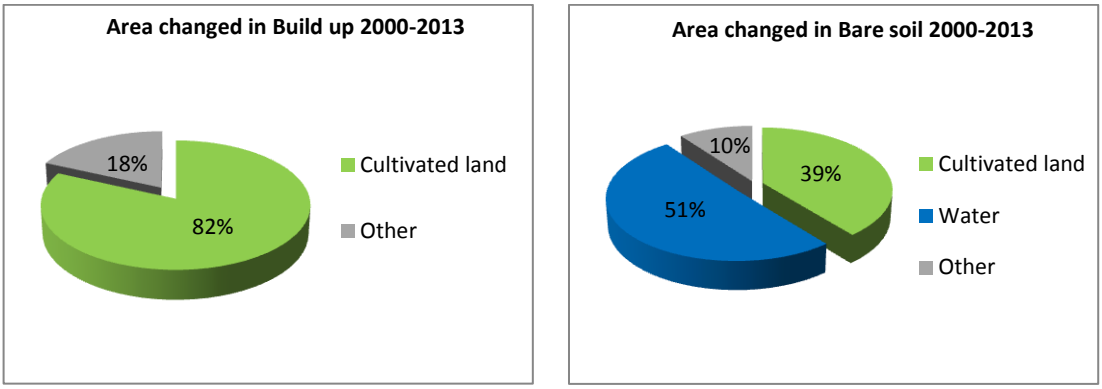

Figure 18 Land use/cover types (%) converted in Build-up (left) and Bare soil (right) between 2000-2013.

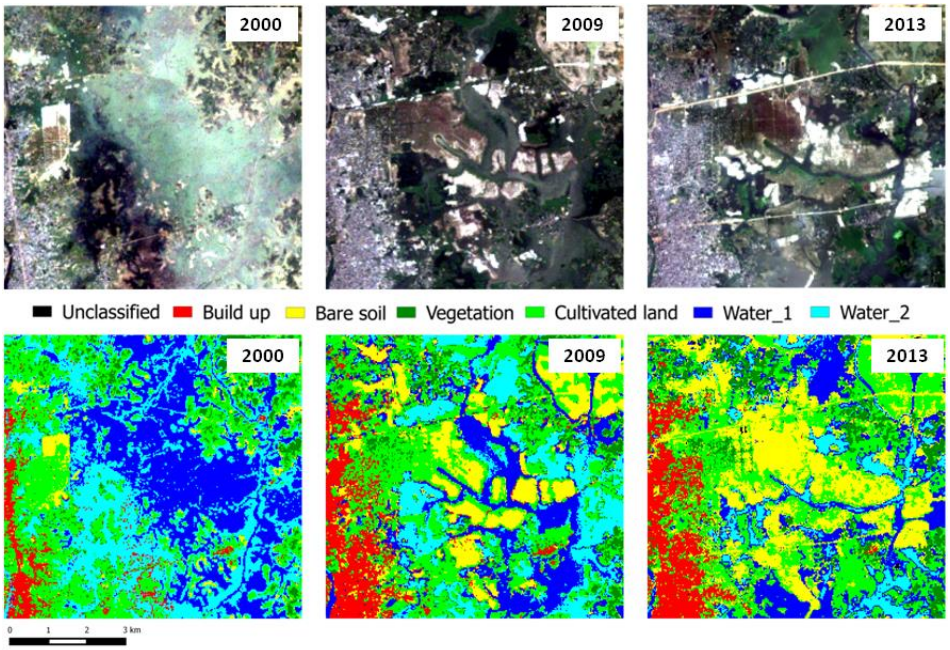

Figure 19 The development of a new areas in the North-East of Dhaka district during 2000, 2009 and 2013.

2.2.4 Considerations

The results of the presented experiment highlight the potential of satellite remote sensing data for mapping and monitoring flood prone areas.

By means of Landsat time series processing, performed after the Maximum Likelihood classification, it was possible to generate multitemporal land use/cover maps of Dhaka district. Firstly, the comparison between these thematic maps allowed to analyse the evolution of the territory during an ordinary monsoon season which generally occurs in the study area from May to October. The maximum flooding extension was delineated and the water recession, after three and four months from the monsoon occurrence, was assessed. Then, the long term monitoring of the Dhaka district was performed in order to evaluate the impacts of the urbanization and the land use/cover conversion on the surface water system. Change matrixes were computed using post-classification change detection procedures in order to quantify the spatial phenomena under investigation.

Despite this process suffers the lack of ground reference data, the validation procedure, performed collecting ground truth points by photointerpretation, showed accuracy values exceeding the 90%, confirming the effectiveness of Landsat images for the identification of the different types of coverage.

Flooding maps, statistics and various information about the study area, obtained as described in the previous sections, may be useful for supporting suitable urban planning and decision making in respect to recurrent flooding events, for the identification of flood risk mitigation actions and to establish emergency strategies. Moreover, the procedure followed in this work could be reproduced in future image acquisitions for the long term monitoring of the study area, of particular interest in recovery and rehabilitation perspective.

This work is an example of using satellite images as a support for the generation of new products and for updating existing databases in order to make available more detailed information concerning a territory, with particular reference to those areas, such as Dhaka district, characterized by ongoing phenomena related both to anthropogenic aspects and natural events.

The proposed methodology may be applied in other region affected by similar risk and characterized by marked seasonality, if a cloud-free multispectral time series (coupled with a certain number of high resolution images for training site purpose) is available.

CHAPTER 3

FLOOD DAMAGE ASSESSMENT

During and immediately following a disaster, timely and detailed situation reports are required to locate and identify the affected areas and then to implement corresponding damage mitigation measures and to address emergency situations such as dealing with diversion of flood water, evacuation, rescue, resettlement, water pollution, health hazards and handling the interruption of utilities. This is the most delicate management category since it involves rescue operations and the safety of people and property. After flood, re-building destroyed or damaged facilities and adjustments of the existing infrastructure occur. The time factor is not as critical as during a disaster [135].

Flood damages can be classified into direct and indirect damages. Direct damages are those which occur due to the physical contact of flood water with humans, property or any other objects. Indirect damages are induced by the direct impacts and occur, in space or time, outside the flood event. The costs of direct impacts are generally easier to quantify than indirect costs since indirect impacts may have effects on time scales of months and years. Both types can be further subdivided into tangible and intangible damages: tangible damages concerning man-made capital or resource flows which can be easily specified in monetary terms, whereas intangible damages are difficult to transfer to monetary values [136][137]. Table 23 shows some examples for the different types of damage.

Flood damage assessments can be performed on different spatial scales related to the spatial extent of the affected areas, the management level and specific objectives for which a study is meant to provide decision support (Table 24). Micro-scale damages are calculated for single affected properties (building, infrastructure etc.); meso-scale assessment is based on spatial aggregations such as land use units, e.g. residential or industrial areas, or administrative units; their size is in the order of magnitude of 1 ha to 1 km^2; macro-scale damages are evaluated for large-scale spatial units; typically, administrative units are used, e.g. municipalities, regions,

countries. Macro-scale analyses aim at providing decision support for national flood mitigation policies, meso-scale analyses are to support decisions on large-scale flood mitigation strategies and the objective of micro-scale analyses is the assessment of single flood protection measures. *Messner et al.* (2007) give recommendations for the choice of the appropriate approach [137].

Table 23 Flood damages categories and some examples.

(source: adapted from *Merz et al*., 2010 [136])

	Tangible	Intangible
Direct	Damage to buildings, contents, infrastructure Erosion of agricultural soil Destruction of harvest Damage to livestock Business interruption inside flooded areas Clean up costs and land and environment recovery	Loss of life Health effects Psychological distress Damage to cultural heritage Negative effects on ecosystems
Indirect	Loss of industrial production Traffic disruption Disruption of public services outside flooded areas Induced production losses to companies outside flooded area Loss of tax revenue due to migration of companies in the aftermath of floods	Loss of trust in authorities Inconvenience of post-flood recovery Increased vulnerability of survivors

Table 24 Characteristics of macro, meso and micro scale approaches of flood damage assessment.

(source: *Messner et al.*, 2007 [137])

Scale	Size of research area	Management level	Demands on precision	Amount of resources per unit of area	Amount of input data
macro	(inter-) national	comprehensive flood mitigation policies	low	low	low
meso	regional	large-scale flood mitigation strategies	medium	medium	medium
micro	local	single protection measures	high	high	high

In this context, satellite remote sensing data, together with an operational GIS, can effectively help to plan many tasks. For mapping purposes, a pre-flood scene and a post-flood image can be compared to delineate the inundated areas. Then flood inundation maps can be exploited to define spatial extent of flooding and to identify the worst flood affected areas; moreover, using GIS to integrate the information extracted from remote sensing data and other available datasets, an evaluation of the flooding impact can be performed. For example, by overlaying flood inundation map and the administrative boundaries or land use/land cover maps, the submerged properties, crop areas, rail and road network affected by flooding etc.

can be identified for the damage assessment as well as for planning rescue operations and recovery actions.

3.1 Post-flood damage evaluation by processing satellite images

Numerous studies have shown the effectiveness of the satellite images collected before-during-after the flood, if they are available, in determining flood damage in different environments. Medium resolution data can be processed to establish the extent of the flood damages and to delineate new flood boundaries. *Pantaleoni et al*. (2007) used Landsat data along with change detection analysis to quantify agricultural damage in relation to flooding in Indiana [138]. *Gianinetto et al*. (2006) developed an integrated approach using slope data obtained from a Digital Elevation Model (DEM) with multitemporal Landsat images for post-flood damage evaluation [66]. Using overlay (intersection) operations in GIS environment between flood map extracted from MODIS and topographic maps, the districts, land cover/use categories, forest and agricultural lands, railway and roads, settlements and people affected by 2011 flood in Sindh province (Pakistan) have been quantified by *Haq et al.* (2012) [139].

High resolution data are suitable for identifying locations and the degree of damages. They can also be used as reference maps to rebuild bridges, roads, homes and facilities. Unsupervised method of change detection technique over very high resolution images has been proposed by *Scarsi et al.* (2014) for separating and quantifying different kinds of change occurred after the 2013 severe flood event in Colorado [140]. *Chen et al.* (2005) used a unsupervised classification on before and after 2004 tsunami SPOT5 images, quantifying the damaged land use types using an automatic change detection method [28]. Land use/cover data from a high resolution images may allow accurate flood damage assessments; *Van der Sande et al*. (2003) used the land cover information extracted from the IKONOS image in combination with water depth and the values of estimated costs obtained from the literature to assess the damage costs [91].

3.2 Case of study: The Bangladesh floods of 2004

Bangladesh is located in South-East Asia and is bordered by India to its West, North and East and by Myanmar to its South-East. To its South, it faces the Bay of Bengal. Bangladesh is the world's eighth-most populous country, with almost 157 million people and among the most densely populated countries [11].

According to the World Risk Report published in 2014 among the 171 countries Bangladesh was ranked 5 because of lives and properties losses caused by natural disasters with repeated frequency in short intervals [7]. Almost every year natural disasters occur, such as floods, tropical cyclones, tornadoes, tidal waves, and their impact is compounded by soil degradation and erosion and human factors such as deforestation and urbanization [141] (Figure 20). As shown in Figure 21, among the natural disasters that occurred in Bangladesh between 1983-2014, floods were the most harmful both in terms of people affected and economic losses.

Number of events	251
Number of people killed	192.426
Average killed per year	6.207
Number of people affected	335.150.064
Average affected per year	10.811.292
Economic Damage (US$ X 1.000)	17.092.500
Economic Damage per year (US$ X 1.000)	551.371

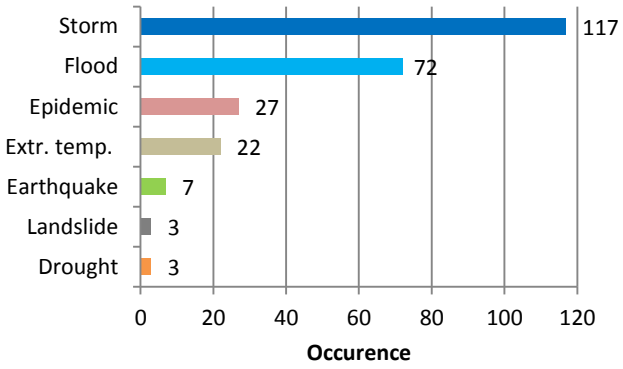

Figure 20 Human and economic losses due to natural disasters (left) and occurrence of natural disasters type (right) reported between 1983 and 2014.

(source: Emergency Events Database EM-DAT, http://www.emdat.be/)

Bangladesh suffers annual flooding and once every three to five years, up to two-thirds of Bangladesh is inundated by floods that cause substantial damage to infrastructure, housing, livelihoods and agriculture [142].

There are some main causes that make this country dangerously subject to flooding: Bangladesh is located on an alluvial plain which contains almost 250 perennial rivers; most of the country surface elevation is less than 5 m above sea level, only 13% of its territory, in the North and East, is hilly and high above sea

level; heavy monsoon rains affect the country from May to September; the rapid increase in river discharge due to the Himalaya snowmelt during spring [8].

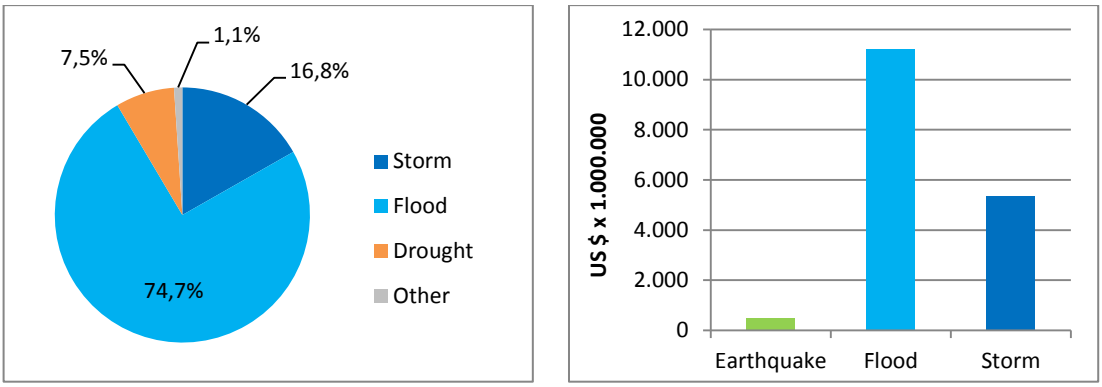

Figure 21 Percentage of people affected by disaster type (left) and estimated economic damages reported by disaster type (right) for the period 1983-2014.

(source: Emergency Events Database EM-DAT, http://www.emdat.be/)

Three main rivers flow in Bangladesh: the Ganges, whose lower course is known as the Padma; the Brahmaputra, whose lower reaches is known as the Jamuna and the Meghna, in the East of the Padma-Jumana area, half of which lies in Bangladesh (Figure 22). Due to its location at the tail end of the delta formed by these rivers, the timing, location, and extent of flooding depends on the precipitation in the entire basin. Nearly 80% of the country's annual precipitation occurs during the summer monsoon season, when these rivers have a combined peak flow of 180.000 m^3/sec, the second highest in the world [143][144].

Bangladesh generally experiences different types of flood. Flash floods carry a heavy sediment load, raising the level of river beds, and are caused by heavy monsoon rains falling on mountains and hill next to the floodplain.This type of flood occurs mostly in some northern area and south-eastern part of the country. In particular, the northern and north-eastern trans-boundary hill streams are susceptible to flash floods from the adjacent hills in India in the pre-monsoon months of April and May. River flood is a most common phenomenon in the country. Normally, 25-30% of the area is inundated during monsoon season along the river; in case of extreme flood events 50-70% of the country is inundated extending the flooded areas far beyond the riverbanks. Some of the worst floods have occurred during the years 1988, 1998, 2004, 2007 and 2010 [145] (Figure 23). The areas adjacent to estuaries and

tidal rivers in the South-West and South-central parts of the country experience tidal floods twice a day due to astronomical tide from the Bay of Bengal. The coastal land is prone to occasional cyclonic storm-surge floods due to tropical cyclones in the Bay of Bengal during April to June and September to November [146].

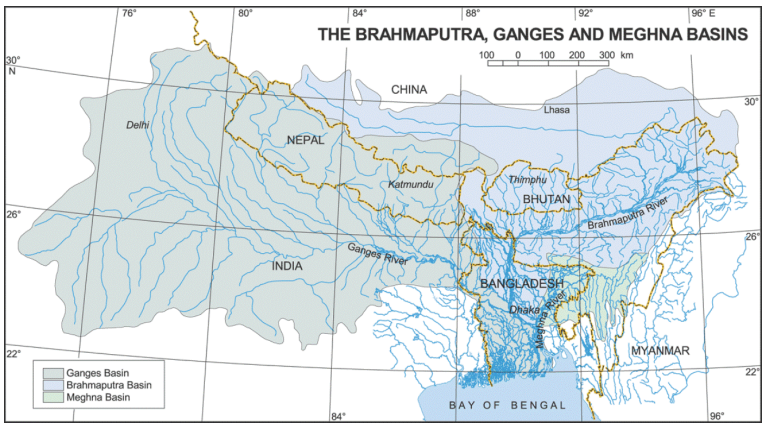

Figure 22 Brahmaputra, Ganges and Meghna Basins.

(source: http://maps-of-bangladesh.blogspot.it/)

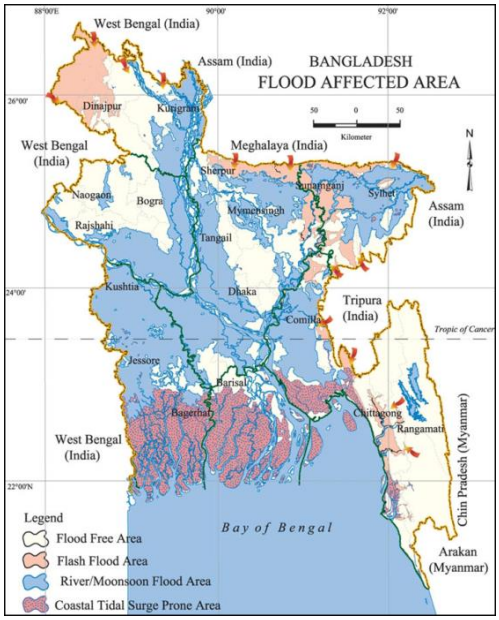

Figure 23 Types of flood in Bangladesh.

(source: http://en.banglapedia.org/index.php?title=Natural_Hazard)

More than 60% of the available labor works in the agriculture sector and 70% of the whole population lives in agricultural districts [8]. The performance of the agriculture sector is in turn heavily dependent on the characteristics of the annual floods. The floodwaters bring alluvial sediment which makes floodplains very fertile

but floods frequently severe causing loss of life and economic damage. Agricultural damage due to flooding has decreased with changes in cropping patterns, particularly the shift from deep water aman rice, highly susceptible to floods, to boro rice, which is harvested before the monsoon season starts. On the other hand, rapid and uncontrolled urbanization, weak environmental management, poor maintenance of infrastructure and increasing population in the floodplains may hinder flood reduction efforts and contribute to additional physical and economic losses after major floods [147].

3.2.1 2004 floods

The 2004 floods commenced around 8 July. This followed early flooding in the northwest districts of Bangladesh in April, that had destroyed much of the main annual boro rice crop in that region just before it was harvested. They rose more swiftly than usual in the same area, and in the northern districts either side of the Brahmaputra/Jamuna River. Water persisted in these regions for some 3 to 4 weeks and gradually drained southerly, causing severe flooding in the central Bangladesh and Dhaka city, especially affecting districts near to the two confluence points of the three great rivers. The high water level and widest extent of the flood was reached on 24 July. The water had receded in most places by mid-August, although it persisted and stagnated in areas behind protective embankments without adequate drainage. In total 39 of 64 districts and 36 million people i.e. the 26% of the total population (137 million of people in 2004) were affected [148][149] (Figure 24). In mid-September, a localised depression caused continuous torrential rain and high winds over a six-day period, bringing renewed flooding to many parts of central Bangladesh, but also flooding areas never normal flooded by the rivers, including Dhaka and other urban areas and some of the most productive agricultural land [147].

In the 39 flood-affected districts, about 4 million housing units were fully/partially damaged. The flood washed away houses particularly at the riverbanks and in certain cases, due to severe erosion, the land was also washed away. The combination of inundation, flash flooding, and long, heavy spells of rainfall caused

numerous damages to the transport infrastructure. Roads were the worst affected infrastructure by the flooding; railway infrastructure also suffered some localized damage on part of the network, while inland water transport infrastructure suffered limited damage.

Figure 24 Affected districts by 2004 floods.

(source: World Bank, 2005 [147])

For rural areas and secondary towns, it was estimated that 200.000 public hand pumps were damaged and wells were damaged mostly due to collapse of the platform, soil erosion and siltation. Obstructions to drainage channels, mixing of sewage with flood water and infiltration of contaminants into the water supply networks and ground water tanks caused serious health risks to the citizens of Dhaka. Severe damage occurred to flood control and irrigation structures, comprising 2.537 km of embankments (147 km completely damaged), 555 km of irrigation-drainage systems (219 km fully damaged), 45 km of riverbank protection works (10 km fully damaged), and 435 water control structures (35 fully damaged). About 4,9 million families were affected in the crops, livestock and fisheries sub-sectors. Damage to crops caused significant production loss of the aus and aman rice crops, jute, summer vegetables, papaya, bananas and sugarcane (Table 25)[147][148].

Table 25 Comparison of losses resulting from the 1988, 1998 and 2004 floods.

(source: World Bank, 2005 [147])

Loss	1988	1998	2004
Land inundated (%)	60	68	38
No. of people affected	45.000.000	31.000.000	36.000.000
Deaths	2.300	1.100	747
No. of homes damaged/destroyed	7.200.000	980.000	4.000.000
Roads damaged (km)	13.000	15.927	27.970
No. Livestock killed	172.000	26.564	8.318
Crops damaged (million hectares)	2,12	1,74	1,3
Rice production losses (million metric tons)	1,65	2,06	1
Total losses (US $ x 1000)	1.400.000	2.000.000	2.300.000

In the following sections, the use of satellite remote sensing data for the post-flood damage assessment in a central area of Bangladesh is described. The vulnerability of different land use/cover types is highlighted and the inundated areas for each affected district are quantified.

3.2.2 The study area

The analysis of the 2004 floods was conducted on a large area, about 3.845 km^2, between 23°51’4’’N, 90°12’6’’E and 23°12’45’’N, 90°39’41’’E. This study area extends between Dhaka and the confluence of the main branch of the Ganges River (Padma) and the Meghna River (Figure 25).

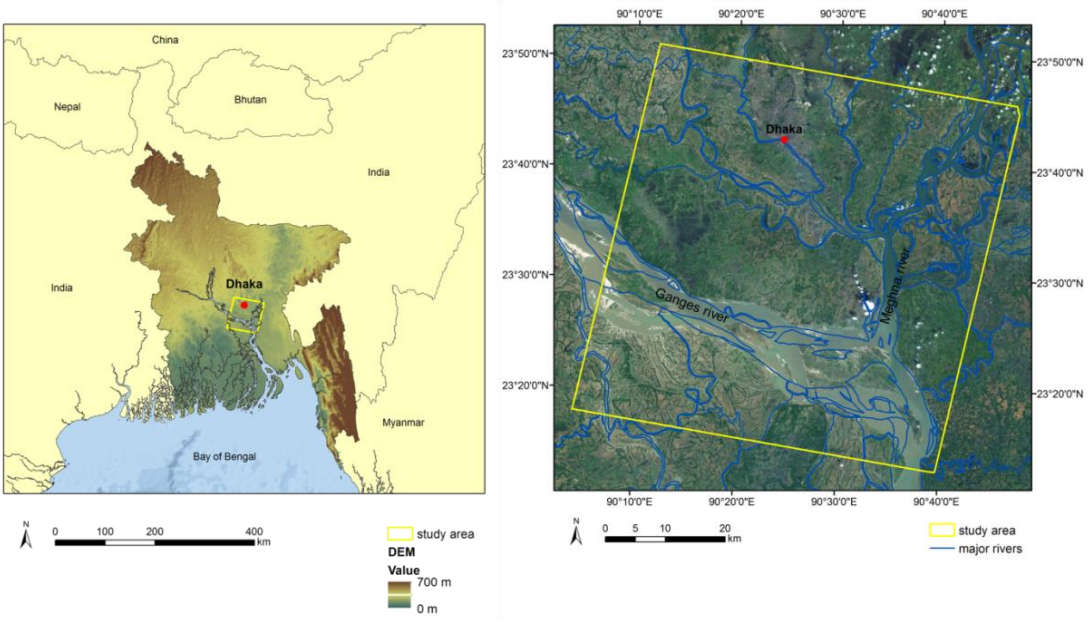

Figure 25 Location of the study area for the 2004 floods analysis.

3.2.3 Data and methodology

In order to detect the inundated areas due to the 2004 floods, a post-event ASTER image was processed. A pre-flood Landsat image was further classified to produce the reference water bodies map. The comparison between the water classes allowed to identify and quantify the flooded areas. Moreover, using overly operations in GIS environment, the flooded areas for each district in the study area were computed and the vulnerability of land use/cover type was highlighted.

3.2.3.1 Data collection

The Landsat image acquired on 24 March 2003 and the ASTER image of 20 October 2004 were collected for analysing the 2004 flooding event; the Landsat image was classified to provide a pre-event setting of water bodies and the ASTER image was processed to map the post-event situation after three months (Table 26).

In addition, land use map, administrative subdivisions (*Thana*) and major rivers provided by ITHACA were used after projected them in UTM-WGS 84 from the local geodetic system Everest_Adj_1937.

Table 26 Satellite images used for studying the 2004 flood.

Date	Satellite	Sensor	Spatial resolution	Product level
24.03.2003	Landsat7	ETM+	30 m	1T
20.10.2004	Terra	ASTER VNIR ASTER TIR	15 m 90 m	1A

3.2.3.2 Image processing

The water extraction in the ASTER image was performed using the three VNIR bands and the five TIR bands, which were subjected to radiometric calibration and normalization respectively. The 8 bands were orthorectified by the ENVI software using the ASTER GDEM of Bangladesh and were resampled to 30 m by a bilinear interpolation. As long as reliable GCPs of sufficient accuracy were not available, an image to image registration was performed, to ensure consistency with the Landsat data. For this purpose 13 tie points were defined, reaching a RMS error by 0,5 pixels, therefore an affine transformation was applied. Moreover, for the ASTER image before the classification the 8 bit VNIR bands were calibrated to TOA

reflectance, while the 12 bit TIR bands were normalized in respect to the maximum value. Even if the physical meaning is not coherent, this pre-processing results in a 8-band stack, with digital numbers ranging between 0 and 1, and it improves the numerical stability of the classification algorithm.

The Landsat multispectral bands were calibrated to Top Of Atmosphere (TOA) reflectance, while TIR band was calibrated to radiance and then normalized in respect to the maximum value.

The images were processed independently using the maximum likelihood classification setting the threshold equal to 0,95, in order to produce pre and post flooding land use/cover maps (Figure 26). Six basic informative classes were identified (Build-up, Bare soil, Vegetation, Cultivated land, Water_1, Water_2). The training samples are derived only from the classified image itself therefore atmospheric correction was not performed [130][131].

Table 27 Description of the informative classes adopted for land use/cover maps and training sites used for each classification.

Class	Description	Training sites	
		24.03.2003	20.10.2004
Build-up	Urban areas, buildings, roads, slum, airports etc.	7/866	6/914
Bare soil	Excavation areas, filled area, exposed soil.	5/822	7/733
Vegetation	Deep vegetated areas (deciduous, coniferous, palm forests, etc.).	8/628	7/708
Cultivated land	Agricultural areas, fallow lands and crop fields.	8/744	8/744
Water_1	Water with suspended solids and sediment transport (river, creeks, flooded areas).	11/975	6/1203
Water_2	Water in contact with vegetation (irrigation ditches, lakes, flooded vegetated areas).	-	4/721
		n polygons/n pixels	

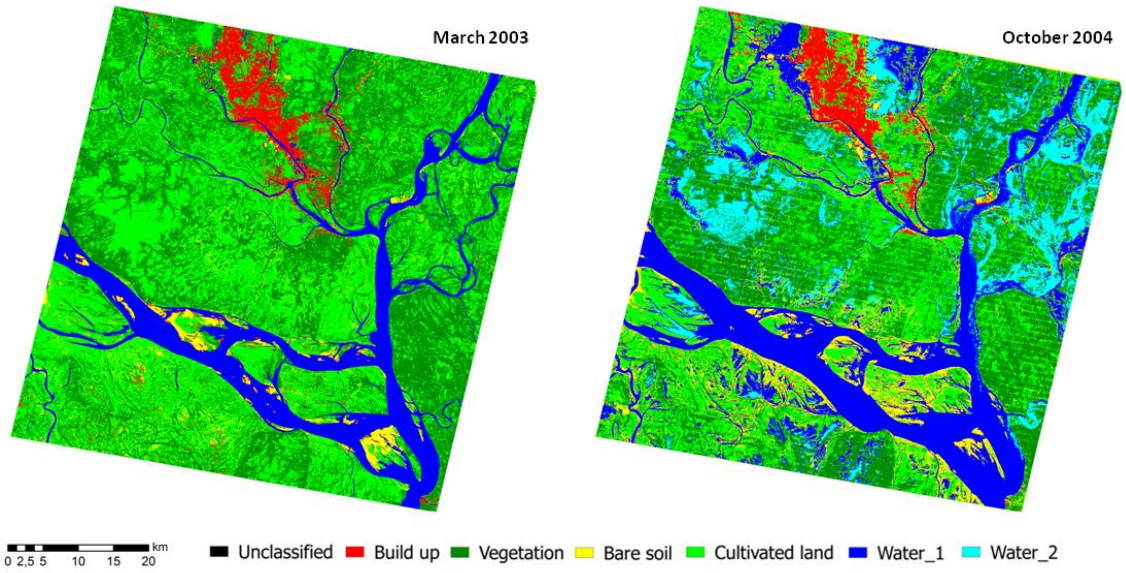

Figure 26 Pre and post-event land use/cover maps obtained classifying the March 2003 Landsat image (left) and the October 2004 Aster image (right).

3.2.4 Results

In the maps obtained from the Landsat and Aster images classification, water classes were extracted and exported in a GIS environment as vector layers: the water class in the 2003 map indicates water bodies in the pre-event condition; the water class resulting from the 2004 map includes permanent water bodies and flooding. Using an operation of overlay intersection, the vector layer of the water present in both maps, which represents the permanent water bodies, was obtained. Using the symmetrical difference between the layer above mentioned and the water class in the 2004 map, the flooding was identified. The permanent water bodies cover about 477 km^2 and the floods affect almost 840 km^2 i.e. the 22% of the whole study area (Figure 27).

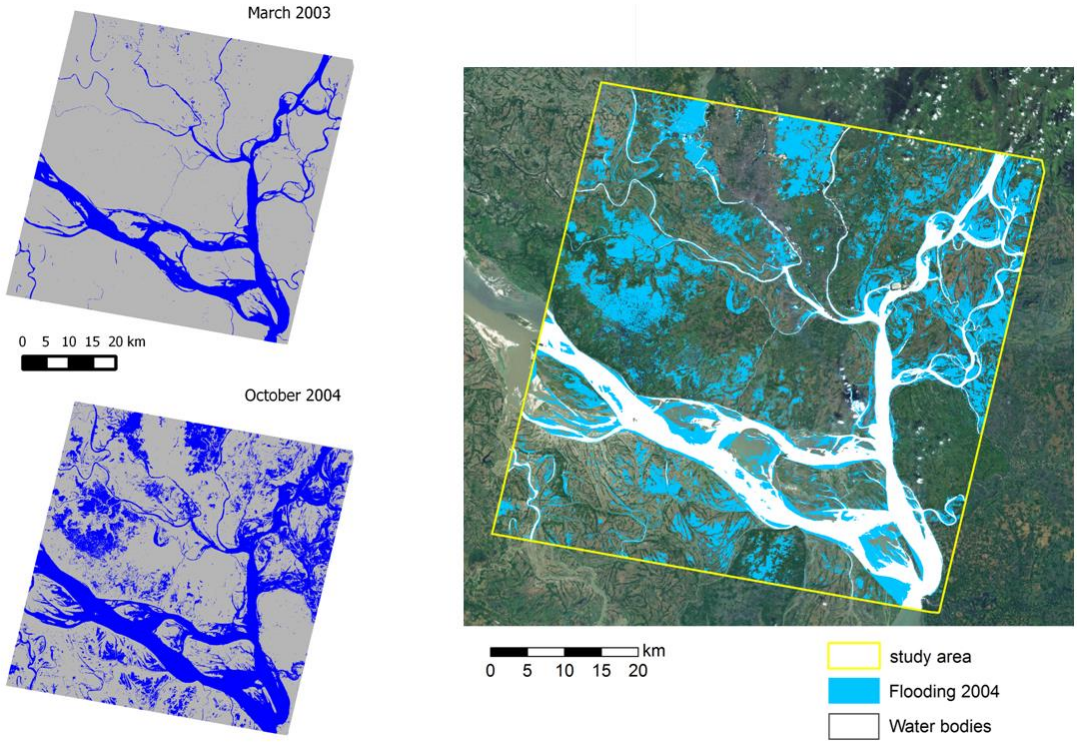

Figure 27 Pre-event setting of water bodies by Landsat 24 March 2003 and post-event setting of water bodies by ASTER 20 October 2004 (left); overlay of the two classifications to distinguish between permanent water bodies and flooded areas (right).

The flooding extension was thereafter associated with the administrative divisions and for each *Thana* in the study area, the flooded area was quantified (Figure 29). The population density data available within administrative subdivisions was then used to evaluate affected people (Table 28); for the study area, a total of 1.737.195 affected people was found. The flooding areas were also associated with the land use data of Bangladesh provided by ITHACA and the vulnerability of the type of land use/cover was highlighted (Figure 30). Moreover, land use/cover types affected by flooding were calculated for each *Thana* (Table 28).

The lands intended for rice cultivation are the most damaged by the flood. In particular, 320,9 km^2 (43 %) and 400,3 km^2 (53,6 %) of total flooded area, equal to 747 km^2, correspond to boro and aman crops respectively. This sum is not equal to the estimate mentioned before (840 km^2) because in the land use/cover vector layer the river beds have a different shape, compared with the permanent water bodies derived from the satellite images. The incongruity may be due to the time lag and the different data source (Figure 28).

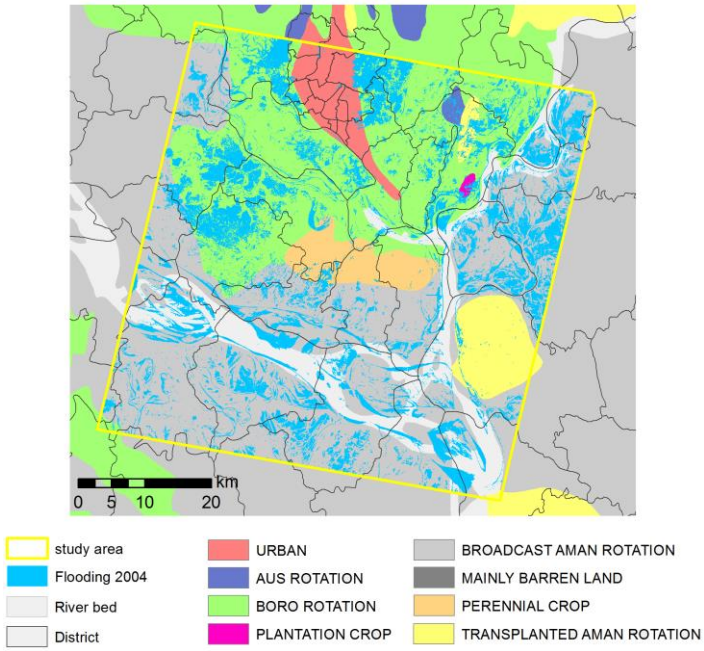

Figure 28 Overlay of 2004 flooding and administrative subdivisions and land use/cover map provided by ITHACA.

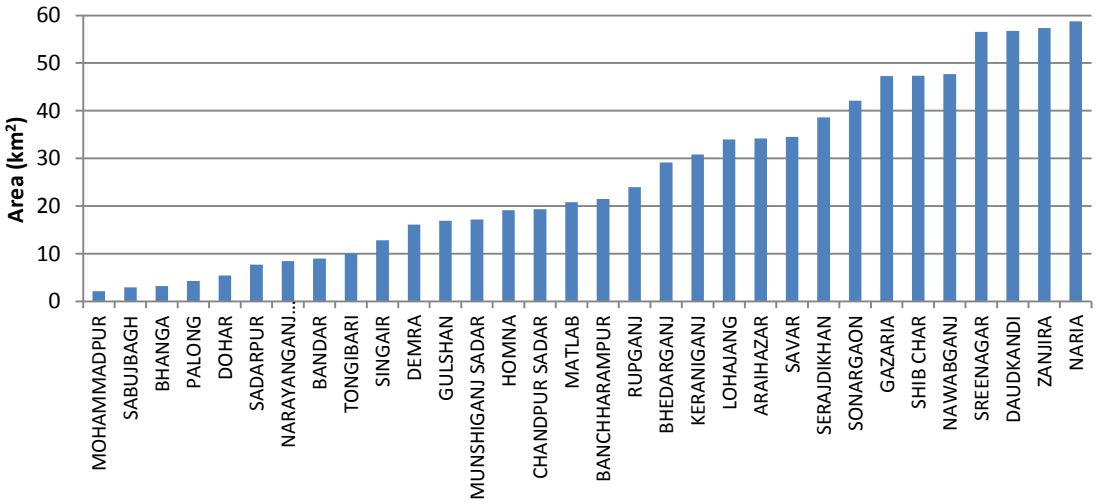

Figure 29 *Thana* affected by the 2004 floods (flooded area extension major to 2 km^2).

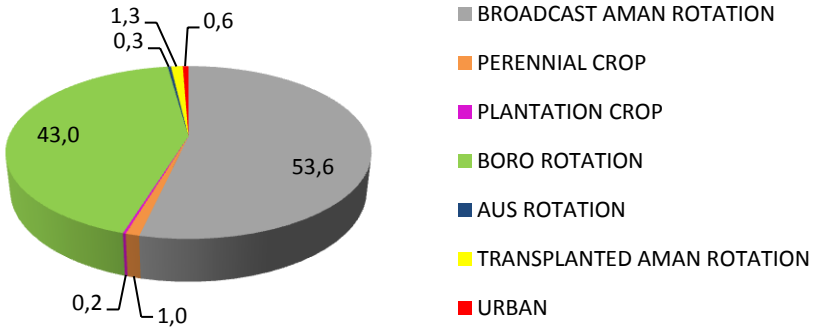

Figure 30 Land use/cover type affected by the 2004 flooding event (%).

Table 28 Example of information extracted by integrating flood map, administrative subdivisions and land use/cover categories.

Thana name	Pop. density (people/km^2)	Flooded areas (km^2)	Affected people	Affected land use/cover Type	(km^2)
DHANMONDI	35.900	0,89	32.059	BORO ROTATION	0,88
				URBAN	0,01
MIRPUR	41.247	0,92	38.064	BORO ROTATION	0,64
				URBAN	0,28
MOHAMMADPUR	48.798	2,11	102.781	BORO ROTATION	2,10
				URBAN	0,01
SABUJBAGH	20.101	2,96	59.508	BORO ROTATION	2,15
				URBAN	0,81
⋮	⋮	⋮		⋮	⋮
SAVAR	1.891	34,48	65.190	BROADCAST AMAN ROTATION	1,36
				BORO ROTATION	32,88
				AUS ROTATION	0,24
SERAJDIKHAN	1.547	38,63	59.746	BROADCAST AMAN ROTATION	0,01
				BORO ROTATION	35,95
				PERENNIAL CROP	2,67
NAWABGANJ	1.158	47,70	55.254	BROADCAST AMAN ROTATION	7,84
				BORO ROTATION	39,86
SREENAGAR	1.245	56,54	70.379	BROADCAST AMAN ROTATION	6,40
				BORO ROTATION	50,07
				PERENNIAL CROP	0,07
DAUDKANDI	1.333	56,78	75.669	BROADCAST AMAN ROTATION	56,78
Total		**839,85**	**1.737.195**		

3.2.5 Considerations

Two multispectral satellite images, Landsat and ASTER, collected before and after 2004 floods respectively, were processed by means of per-pixel supervised classification for mapping pre-event setting of water bodies and post-event water bodies extension. The comparison of these maps allowed to separate surfaces cover by water belonging to permanent water bodies and flooded areas. Flooding extension was then used along with administrative subdivisions and the land use/cover map of Bangladesh to evaluate inundated areas for each districts, land use/cover types most affected by flooding and to provide information about the number of people involved.

The achieved results demonstrate the effectiveness of satellite images, acquired before and after flood occurrence, in detecting and quantifying flooded areas. In particular, medium spatial resolution images have proved useful for large scale view of flood phenomena; inundated zones, which extend to several square kilometres, can be mapped very effectively. Emergency managers can get an overview of the most affected areas and disaster-mapping organizations can use these overview maps to target high-resolution satellite acquisitions.

The study confirmed the GIS capability to store, integrate and analyze different geospatial data such as flood and land use/cover maps, demographic data etc. which are crucial information for the damage assessment during response phase. By overlaying flood map and the population density data, the number of potentially affected people can be obtained in order to implement rescue operations and distribute the humanitarian help. Intersection operations between flooding and land use/cover type provide the extension of the damaged land use/cover types and these information can be employed to quantify losses in monetary values. These products can also support recovery planning and assist the restoration of infrastructural services and the relocation of affected settlements. Moreover, damage assessment maps can provide valuable information to delineate new flood boundaries, useful for producing flood risk maps.

The presented procedure for post-flood damage assessment corroborates that geospatial techniques can be an effective alternative to conventional hydrological flood damage evaluations, particularly for countries lacking detailed spatial data and in case of large areas involved. The use of remote sensing data for analyzing flood phenomena provides a high potential for developing countries since it is difficult for their governments update databases by traditional surveying and mapping methods which are both costly and time consuming. The approach could be applied to future flood events since the GIS system allows the rapid update of the information used for the damage estimation.

A last observation is that the procedure focused on optical images for mapping flood extension. Monsoon season, as well as in Bangladesh, is mainly cloudy weather, and therefore the adoption of satellite optical observations could result in

the lack of data acquisitions. Radar imagery could be in this case a suitable alternative for flood extension mapping (section 2.1).

CHAPTER 4

FLOOD RISK ASSESSMENT

Flood hazard will impact different types of elements-at-risk and it is therefore important to calculate the risk for different sectors/environments (e.g. housing, agriculture, transportation, education, health, tourism, protected areas, forests, wetlands, etc.). The methodology for conducting risk assessments can be broadly classified into quantitative and qualitative approaches [150].

Quantitative approaches aim at expressing the risk in quantitative terms, either as probabilities or as expected losses. They use numerical modelling, such as hydraulic, hydrological and hydro-dynamic models and Digital Terrain Models (DTM) to perform flood hazards with exceedance probability. The output is then integrated with land use or property information to derive flood loss functions, essential to determine flood risk [151][152][153].

Qualitative methods, typically, employs gauge records, satellite data, or both, along with the elevation model to derive flood extent and depth. Information such as elements at risk (e.g. population density, buildings) can subsequently be integrated within a GIS to develop spatial coexistence models for flood risk assessment [58]. Qualitative methods depend on expert opinions and consider a number of factors that have an influence on the flood risk. These approaches are mostly based on the development of so-called risk indices [154][155]. Some qualitative approaches, however, incorporate the idea of ranking and weighting and may become semi-quantitative in nature [150].

Quantitative methods are able to provide superior results, but they can require more a-priori data and detailed morphological information together with advanced numerical models, while the qualitative and/or semi-quantitative approaches are relatively simple to implement within a GIS and capable to handle different data depending on its availability [156]. The latter methods have proved to be useful for regional studies and for the initial screening process to identify hazards and risks [14][157][158][159]. Furthermore, the majority of flood risk research, particularly in developing countries, is based on these approaches. However, quantitative

methods are popular within the hydrological community [153]. A reasonable explanation is that quality data are often lacking in developing countries, where the possibility of obtaining reliable numerical data is often limited [155].

4.1 Semi-quantitative approaches: Multi-Criteria Analysis (MCA)

Multi-Criteria Analysis (MCA) or Multi-Criteria Evaluation (MCE) is a decision-making tool, used in environmental systems analysis to evaluate a problem by giving an order of preference for multiple alternatives, on the basis of several criteria that may have different units [160]. The purpose of an MCA is to compare and rank alternative options and to evaluate their consequences, according to the criteria established. Two procedures are common in MCA. The first involves Boolean overlay, whereby all criteria are reduced to logical statements of suitability/target and then combined by means of one or more logical operators such as intersection (AND) and union (OR). With the second procedure, continuous criteria (factors) are standardized to a common numeric range, and then combined by means of a weighted average. The result is a continuous mapping of suitability/target that may then be masked by one or more Boolean constraints to accommodate qualitative criteria, and finally threshold to yield a final decision [161]. A comprehensive review and classification of refereed journal articles, covering spatial multi-criteria decision analysis, can be found in *Malczewski* (2006) [162].

Various MCA techniques such as Analytical Hierarchy Process (AHP), Weighting Linear Combination (WLC), Ordered Weighting Averaging (OWA) etc., have been used for flood susceptibility and vulnerability analysis and risk mapping [163][164][165][166]. In this context, GIS systems with their ability to handle spatial data are a suitable tool for incorporating all the factors to be analysed, for an effective implementation of MCA methods for flood risk assessment [167].

Among these methods, AHP is one of the widely used multi-criteria decision making tools because of its simplicity in implementation and interpretation, the capability in handling scarcity of quality data and the efficiency in regional studies [167][150].

Introduced and developed by *Saaty* in 1980, the AHP procedure implements a pair wise comparison technique for deriving the priorities of the criteria in terms of their

importance in achieving the goal (Figure 31). In the AHP, the decision making process starts with dividing the problem into issues, which may optionally be divided further to form a hierarchy of issues. The pairwise comparison matrix is used for comparing the alternatives and defining the importance of each one relative to the others. In order to help the decision maker to assess the pair-wise comparisons, Saaty proposed a nine point intensity scale of importance between two elements [168]. The suggested numbers to express degree of preference between the two elements are shown in Table 29. Because the user gives judgments subjectively, the logical consistency of these evaluations is tested in the last stage. The ultimate outcome of the AHP is a relative score for each decision alternative, which can be used in the subsequent decision making process [155][156][169].

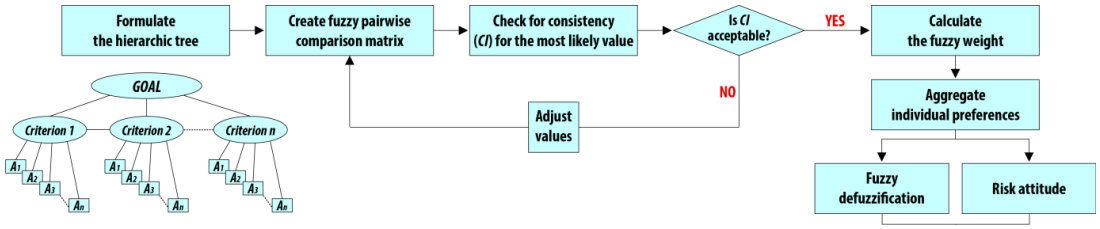

Figure 31 Analytic Hierarchy Process (AHP) flowchart.

(source: adapted from *Siddayao et al*., 2014 [156])

Siddayao et al. (2014) combine AHP with GIS to assess flood risk in the municipality of Enrile (Philippines). Despite the lack of weather stations and rain gauges data, they provide valuable information about flood risk considering two types of data sources: graphical data, i.e. political administration map and topographic map, and document data such as population and socio-economic statistics [156]. To model and predict the magnitude of flood risk areas, *Ouma and Tateishi* (2014) proposed an integrated AHP and GIS analysis techniques for the case of Eldoret municipality (Kenya). The flood risk vulnerability mapping follows a multi-parametric approach and integrates some of the flooding causative factors such as rainfall distribution, elevation and slope, drainage network and density, land-use/land-cover and soil type. From the vulnerability mapping, urban flood risk index (UFRI) for the case study area, which is determined by the degree of vulnerability and exposure is also derived [155]. *Wang et al.* (2011) applied a MCA methodology along with GIS for

the assessment of a mesoscale regional flood risk index for the Dongting Lake region (China) using a fuzzy analytic hierarchy process (FAHP) to achieve the weight of each factor causing floods [150].

Table 29 Nine-point intensity of importance scale.

(source: adapted from *Ouma and Tateishi*, 2014 [155])

Intensity of importance	Definition	Description
1	Equally important	Equally contribute to the objective
3	Moderately more important	Experience and judgment slightly favor one over the other
5	Strongly more important	Experience and judgment strongly favor one over the other
7	Very strong more important	Experience and judgment very strongly favor one over the other
9	Extremely more important	The evidence favoring one over the other is of the highest possible validity
2,4,6,8	Intermediate values	When compromise is needed
Reciprocals of above	If element i has one of the above numbers assigned to it when compared with element j, then j has the reciprocal value when compared with i	-
Ratios (1.1–1.9)	If the elements are very close	May be difficult to assign the best value, but when compared with other contrasting elements the size of the small numbers would not be too noticeable, yet they can still indicate the relative importance of the elements

4.2 Case of study: flood hazard map of a portion of Yialias river catchment area, Cyprus

The island of Cyprus is located in the north-eastern corner of the Mediterranean Sea and, therefore, has a typical eastern Mediterranean climate: the combined temperature rainfall regime is characterized by cool-to-mild wet winters and warm-to-hot dry summers [170]. Despite Cyprus is characterized by long and frequent dry periods, it also suffers from flooding events [9]. Almost every year, localised and in some cases more widespread flooding affect parts of Cyprus, causing damages to properties, destruction to infrastructure and housing and sometimes the loss of human life. Various factors, such as the meteorological situation and type and

intensity of precipitation, the geomorphology, the geology and the human intervention to the territory are responsible for flood events.

Flood events are typical during the cold season while, during the hot season, local thunderstorms are common, with some even resulting in floods generally inland. During the thirteen-year period (1994-2006) analysed by *Savvidou et al.* (2008), 43 cases of flooding were reported mainly over urbanized areas. As shown in Figure 32, the frequency of flooding events increased considerably between 2000-2010, in comparison with the period 1970-2000. The number of victims also increased (Figure 33) [171].

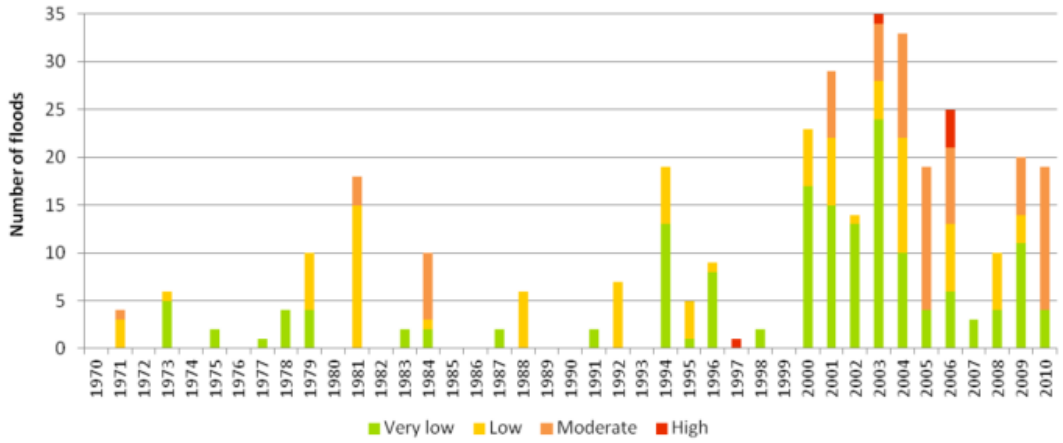

Figure 32 Number of flooding events per year in Cyprus (1970-2010).

(source: CYPADAPT project report, 2012 [171])

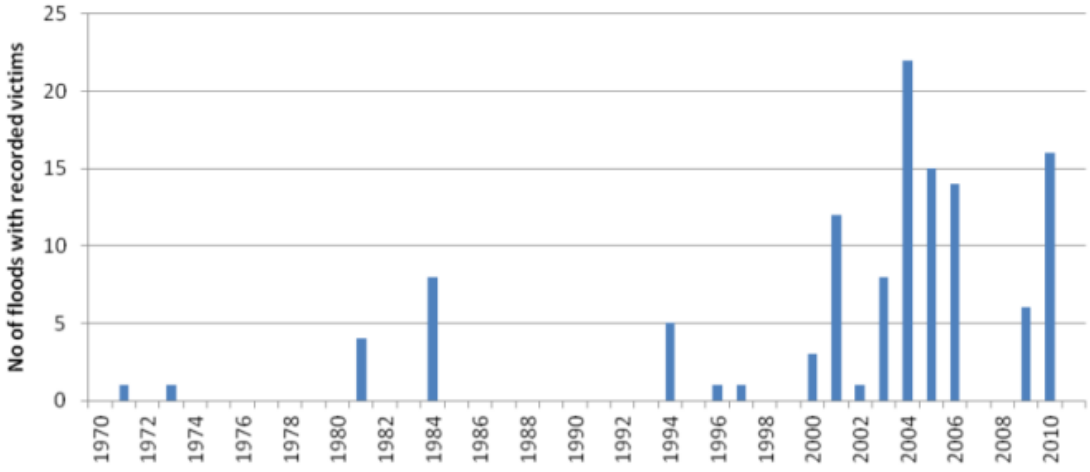

Figure 33 Number of flooding events with recorded victims in Cyprus (1970-2010).

(source: CYPADAPT project report, 2012 [171])

There are no perennial rivers, while there are numerous seasonal rivers. Most rivers flow 3-4 months a year and they are dry during the rest of the year. Therefore, the occurrence of heavy rainfalls commonly results in debris transport and blockage of structures, such as culverts and bridge openings, generally undersized for these flow rates (Figure 34). Moreover, the urbanization of the catchment area and the degradation of the natural environment, resulting in the increase of flooding runoff volume and in the decrease of the time of water flow, exacerbate the flood impacts.

Figure 34 Post-flood debris removing in Polis (Paphos) December 2012 (left); river overflow in Ayios Theodoros (Larnaca) September 2013 (right).

(source: http://www.cyprus-storms.net/)

The lack of appropriate model of residential development, with incomplete man-made drainage systems and the shortage of its maintenance, are the main causes of widespread flooding in urban areas, during extreme weather conditions. In particular, the urban centres are more sensitive to flood risk mainly due to their dense structuring and the restriction of green space, the elimination of natural waterways for the construction of roads, the deficient or even absent storm water drainage system and the covering of waterways and drain entrances with garbage. On the other hand, mountain areas (central part of the island) are less sensitive to floods, given that the inclination of terrain, together with the infiltration capacity of forested areas, decrease the probability of flooding events (Figure 35).

In compliance with the Floods Directive 2007/60/EC, the Water Development Department (WDD) of the Ministry of Agriculture, Natural Resources and Environment (Republic of Cyprus, Nicosia) identified 19 areas around the island as "Areas with Potential Significant Flood Risk" (Figure 36). The corresponding linear

extension is about 135 km and these areas are distributed uniformly in respect to all the urban centres of Cyprus (no mountain areas included). They mainly refer to river parts that pass through built-up areas and are characterized by frequent and significant flash floods [171].

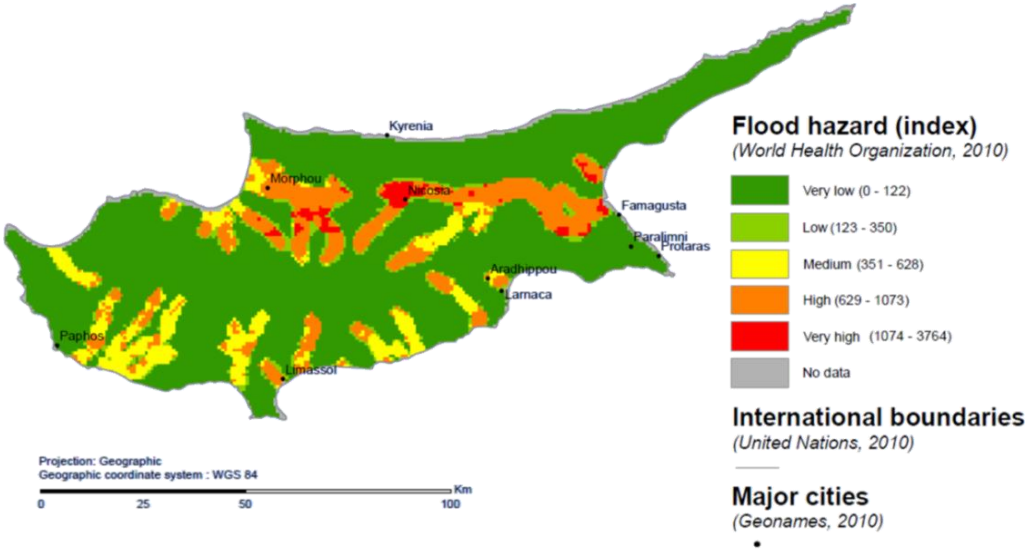

Hazard intensity levels and number and percentage of people exposed					
Very high	High	Medium	Low	Very low	No data
185 389 (21.07 %)	183 380 (20.85 %)	27 752 (3.15 %)	77 684 (8.83 %)	378 452 (43.02 %)	27 066 (3.08 %)

Figure 35 Cyprus flood hazard distribution map and the population (number and percentage of people) exposed to hazards by level of intensity.

(source: World Health Organization Regional Office for Europe, 2010 [172])

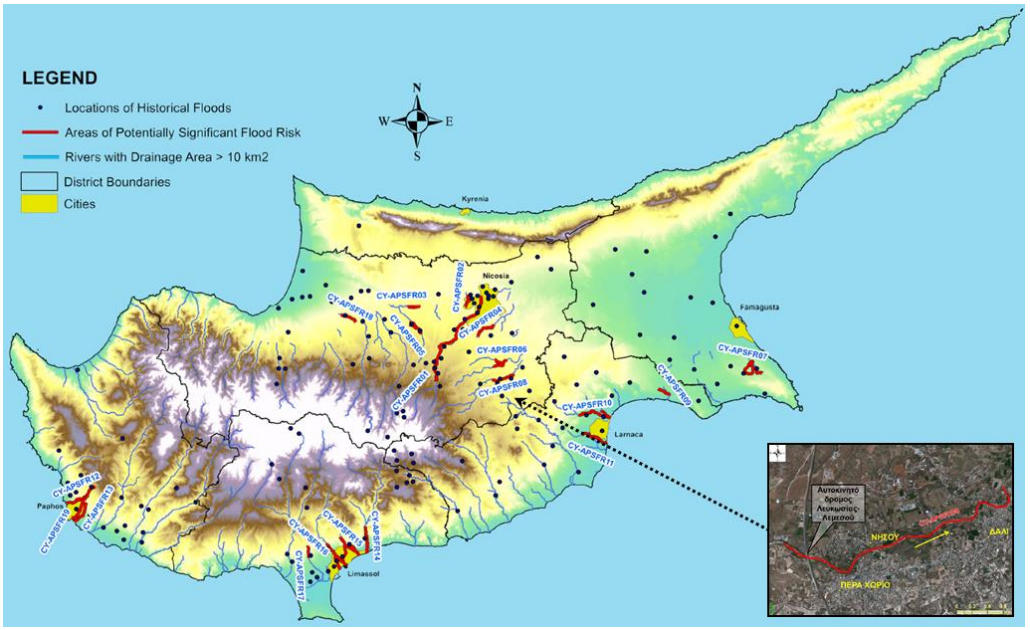

Figure 36 Areas with potential significant flood risk in Cyprus.

(source: Water Development Department, 2011 [173])

In the following sections, the use of satellite remote sensing data coupled with MCA technique for flood hazard map purpose is described. The case study concerns a portion of the Yialias river watershed basin, in Nicosia district, including one of the above mentioned areas, identified by the WDD, for which potential significant flood risk exists.

4.2.1 The study area

Located in the central part of the Cyprus island, 20 km towards the South of the capital Nicosia, the study area is about 70 km^2 in size. Specifically, it is situated between longitudes 33°16'37'' and 33°26'47'' and latitudes 34°56'18'' and 35°2'51''.

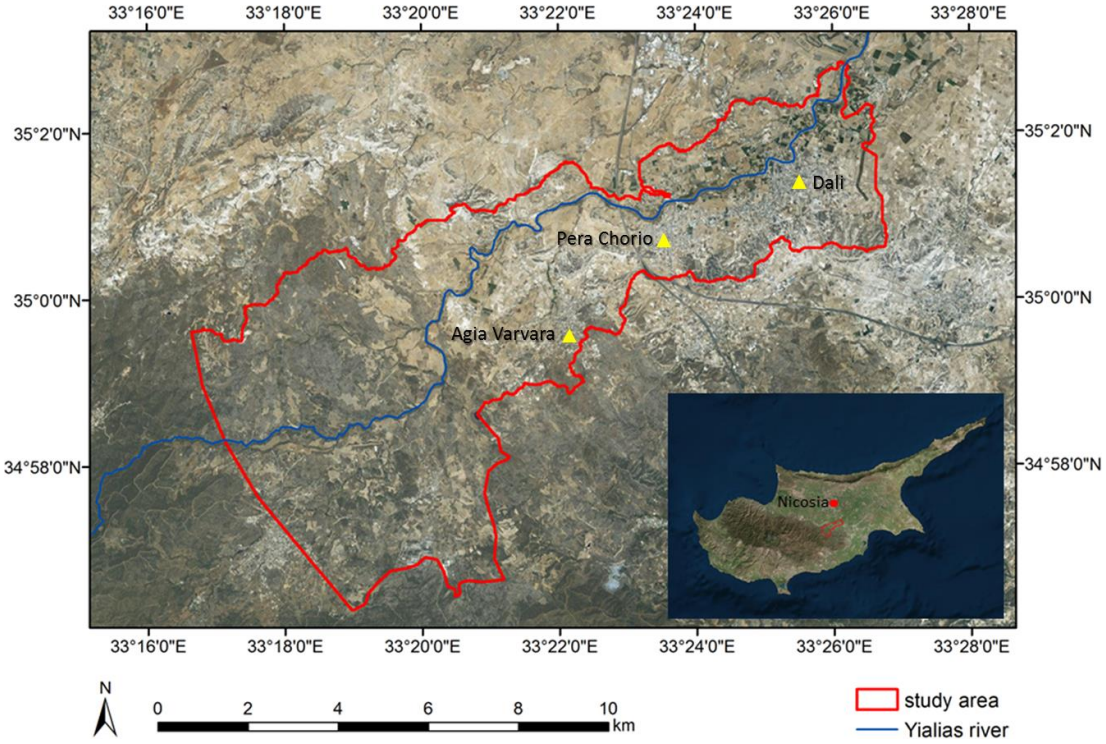

Figure 37 Location of the study area.

This area is the portion of the Yialias river watershed basin including Agia Varvara, Pera Chorio and Dali villages (Figure 38).

The elevation ranges from 193 to 482 m a.s.l. with steep and smooth zones in the upstream and downstream areas respectively. From West to East metamorphic and volcanic rocks outcrop followed by sedimentary units such as marl-chalk and alluvium/colluviums deposits (Figure 39).

Figure 38 Typical landscapes of the study area (Pera Chorio).

Figure 39 Volcanic rock (left) and marl/chalk (right) outcrops.

Figure 40 Yialias river trough Dali village during summer (left) and winter (right).

(source for the right figure: http://www.panoramio.com/photo/66227319)

As the most of the island rivers, the Yialias has an intermittent stream being dry during the summer season (Figure 40). During the last 20 years three extreme floods occurred in this area, especially in the downstream part. According to historical data the most extreme events took place on December 1992, February

2003 and October 2009. All these extreme floods caused significant damage to properties and constructions [174][175].

4.2.2 Data and methodology

In order to produce an easily-readable and rapidly-accessible flood hazard map of the study area, the MCA methodology was performed considering some parameters that control water routing when high peak flows exceed the drainage system capacity [176]. Five flood-causing factors were selected: slope, distance to channels, drainage texture, geology and land cover, referring to previous research works and also considering the available data [156].

According to the rate of contribution of each parameter to the flood hazard, ranking values were assigned to each different class of each parameters. Moreover, a pair wise comparison technique was used to derive the criteria priorities in terms of their importance in achieving the goal.

Processing the DEM of the study area in GIS environment, slope, stream network and therefore distance to main channels and drainage texture data were generated; the land cover map was obtained classifying the very high resolution satellite image GeoEye-1; the geology map was obtained converting polygon features to raster. The Figure 41 shows the methodology workflow.

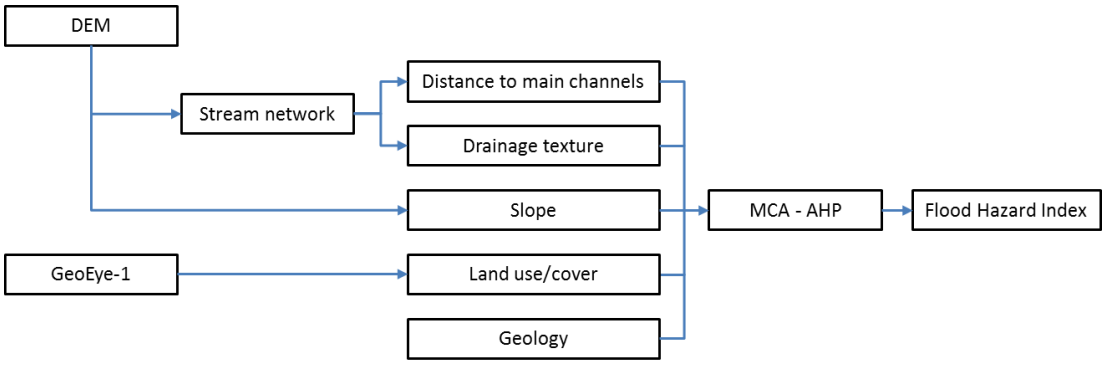

Figure 41 Methodology workflow.

4.2.2.1 Data collection

For the purposes of the study, a very high resolution GeoEye-1 image acquired on 11th December 2011 (pixel size approximately of 1,65 m for VIS and NIR bands) was processed for land cover map purpose. The Digital Elevation Model (DEM) with a spatial resolution equal to 5 m, developed by the Department of Civil Engineering

and Geomatics - Cyprus University of Technology using GeoEye-1 stereoscopic images, was used for generating quantitative geomorphologic parameters such as slope and drainage network. The Department of Civil Engineering and Geomatics of Cyprus also provided the 1:250.000 geological map of the study area produced by the Geological Survey Department.

4.2.2.2 Image processing: object-oriented classification

Before the classification, the GeoEye-1 was subjected to radiometric calibration (TOA reflectance) and the four bands were orthorectified by the ENVI software using the 5 m pixel size DEM of the study area considering an average geoidal undulation equal to 28 m (based on the EGM2008 gravity model). The orthorectified image was the resampled to 2 m by a bilinear interpolation.

To produce the land use/cover map of the study, area the satellite image was classified by an object-oriented classification approach performed with eCognition 8.9 software (Figure 42)[177].

Object-oriented procedure is an evolving technology where textural and contextual/relational information is used in addition to spectral information for classifying data[178]. It is particularly useful for extracting and mapping features from high spatial but low spectral resolution images [179]. Object-oriented classification is driven by an understanding of image objects rather than pixels, i.e. homogeneous groups of contiguous pixels that have similar spectral and/or spatial characteristics. They form building blocks consisting of abstract information that can be used at different image object levels. Image objects can be extracted by using different segmentation algorithms; the basic task of them is to merge homogenous pixels into image elements to enable the differentiation between heterogeneous neighbouring regions [180]. Segmentation can be carried out in hierarchical scales with semantic relationships between objects at different levels, allowing for effective multi-spatial resolution analysis. The accuracy of the classification depends directly on the segments and an erroneous segmentation will result in inaccurate classification. Segmentation phase is followed by the image

objects classification based on the different features such as spectral, shape, texture, hierarchical and contextual information above mentioned [179].

A semi-automated, hierarchical, multi-level object-based classification was implemented as process tree (Figure 43).

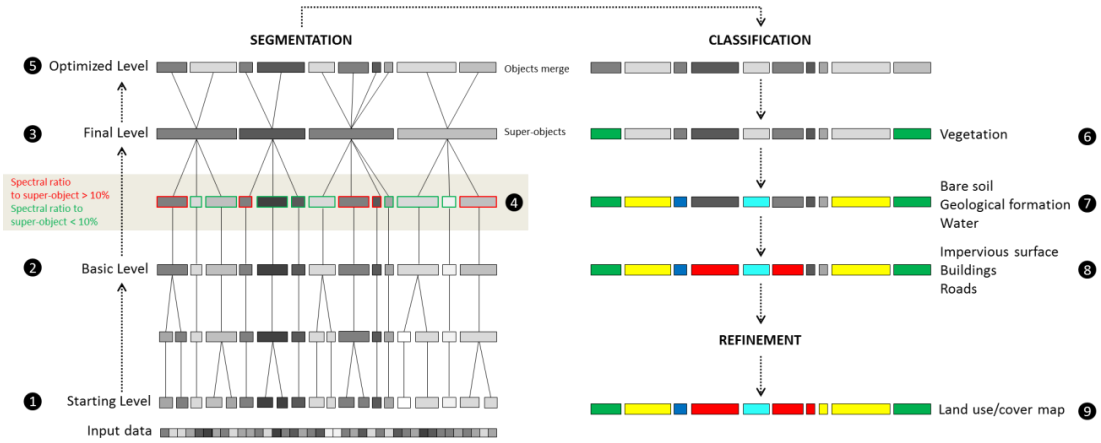

Figure 42 The object-oriented classification workflow.

(source: modified from *Taubenböck et al.*, 2010 [181])

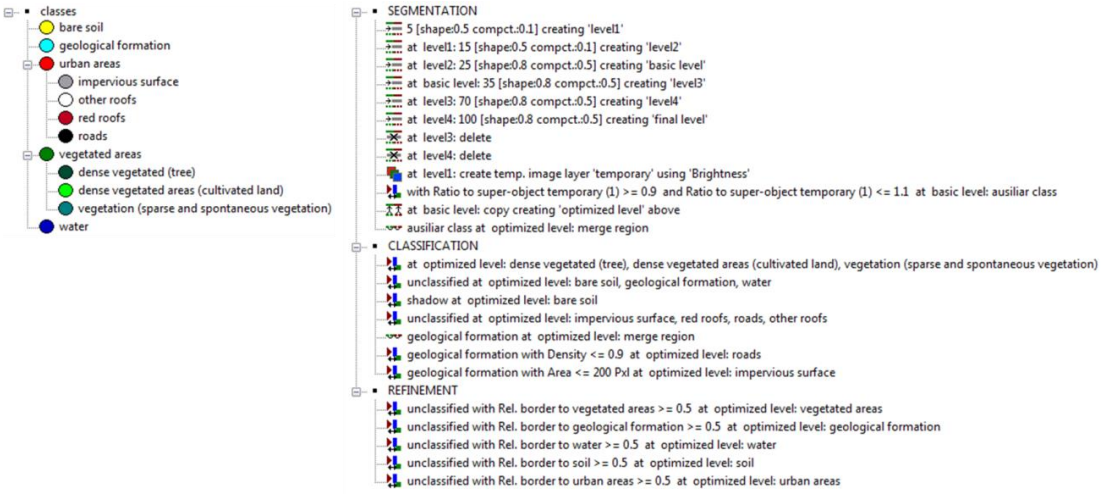

Figure 43 Class Hierarchy (left) and Process Tree (right).

The multiresolution segmentation algorithm, a bottom-up region growing technique, was used to generate the image objects [182]. Through this algorithm both spectral and shape heterogeneity can be taken into account through user-defined colour and shape parameters. Moreover, user can control the scale parameter to define the acceptable level of heterogeneity: a larger scale parameter results in larger objects than setting small scale values. The eCognition multiresolution segmentation starts with one-pixel objects and in numerous

subsequent steps, smaller image objects are merged into bigger ones. Throughout this pairwise clustering process, the underlying optimization procedure minimizes the weighted heterogeneity of resulting image objects. In each step, that pair of adjacent image objects is merged which results in the smallest growth of the defined heterogeneity. If the smallest growth exceeds the threshold defined by the scale parameter, the process stops [183]. Depending on the specific application, this method could not yield a perfect partition of the scene but it could produce either too much and small regions (over-segmentation) or too less and large segments (under-segmentation) [180]; therefore, it could be difficult to obtain objects closer to the spatial, spectral and textural characteristics of the real-world structures in a single segmentation phase.

In order to overcome this limitation and then to achieve image objects similar to the real-world elements, a multilevel segmentation procedure was performed. The main idea of multilevel analysis is that, for each level of detail, it is possible to identify different objects that are peculiar to the considered level and that should not appear in other levels [184].

In the implemented multilevel approach each superior level was generated by using a higher scale parameter. The main aim was the generation of two basic segmentation levels, the basic level (number 2 in Figure 42) and final level number 3 in Figure 42), with a significantly increased scale parameter. Whenever a sub-object in the basic level shows a significant spectral difference (“Brightness” higher/lower than 10%) to its super-object on the final level the corresponding segments are reduced at the final level to their original spatial configuration. Thus, this segment stays exactly the same shape as in the basic level, while segments with no significant spectral difference (“Brightness” lower than 10%) from the super-object are merged [185]. The final output is one single level, the optimized level (number 5 in Figure 42), comprising large segments in homogeneous areas and distinctively smaller image objects representing small-scale structures and heterogeneous regions (Figure 44).

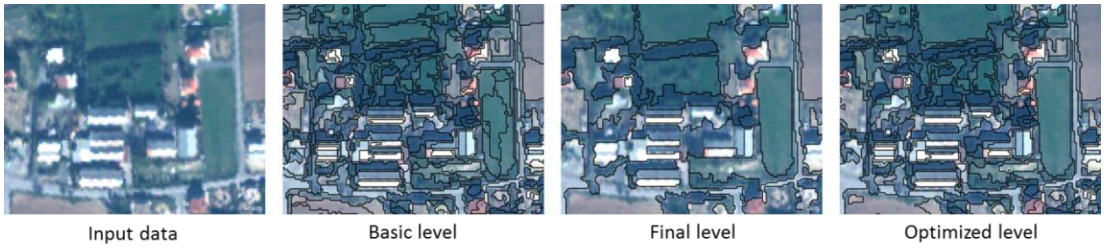

Figure 44 Multilevel segmentation approach.

The classification procedure was then applied to the image objects at the optimized level. In particular, for each class different attributes were considered setting specific thresholds (Figure 45). In the first step vegetated areas were identified; then the rules for the geological formation, bare soil and water classification were applied on the resulting unclassified objects. Finally, generic impervious surfaces, building (red and other roofs) and roads were classified in order to detect the urban areas.

Specific rules were applied to avoid misclassification between marl/chalk (geological formation) and impervious surfaces due to their similar spectral response [174]. In particular, the image objects belonging to the geological formation class were merged; therefore, using shape rules small objects and elongated objects were assigned to impervious surface and roads classes respectively.

Some rules based on contextual features were used to refine the classification results (number 9 in Figure 42).

Figure 55 (right) shows the final land use/cover map.

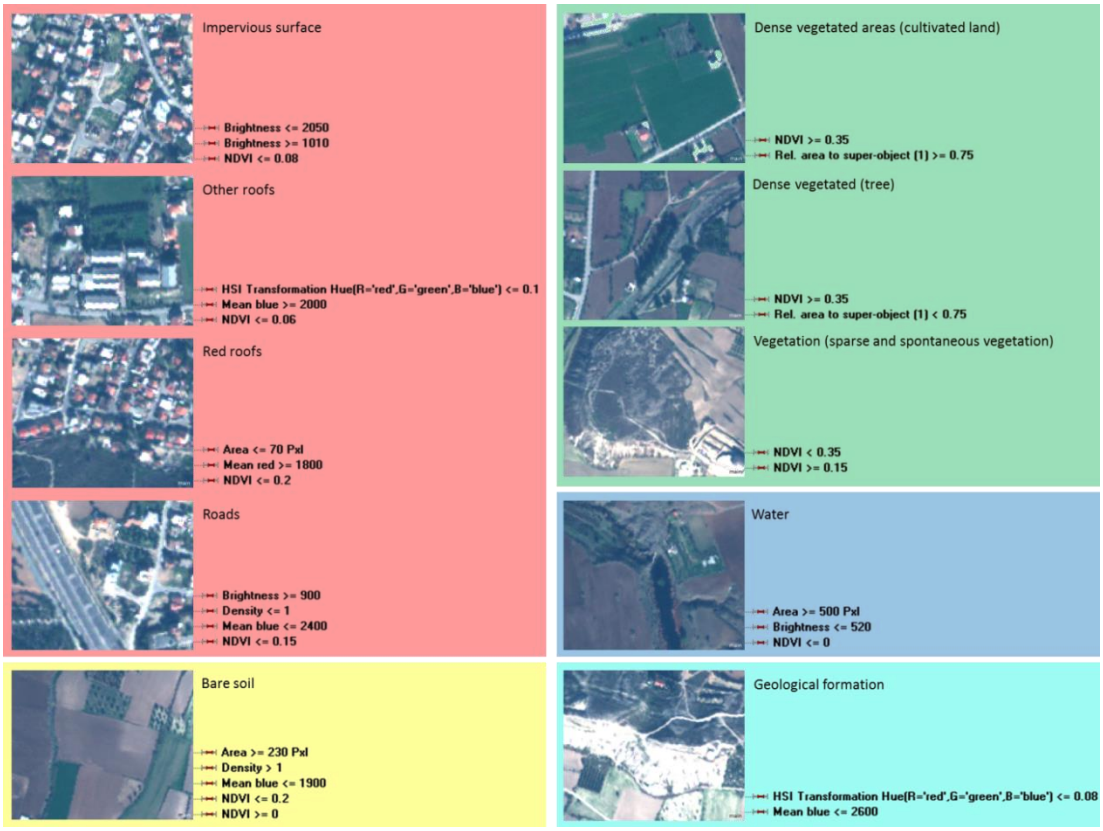

Figure 45 Features and threshold used in the classification rule-set.

The map validation was performed using a number of check points, selected by means of the photointerpretation of the high resolution colour image, acquired on 3rd December 2011. Moreover, field campaigns, carried out during July 2014, helped to verify the cover class of the check points. Since the limited extension of water bodies, the Water class accuracy was verified overlaying it directly on the high resolution image (Figure 47). Therefore, the confusion matrix was computed for urban areas, vegetation, soil and geological formation classes (Table 30).

An overall accuracy equal to the 89,5% was achieved. Relevant errors are attributable to the commission of the geological formation class. Some urban areas, in particular portions of roads or impervious surfaces, remain in the geological formation class even after applying the geometric rules to avoid this misclassification. Moreover, probably due to the presence of aggregates containing marl/chalk, some image objects belonging to bare soil were assigned to the geological formation class (Figure 48).

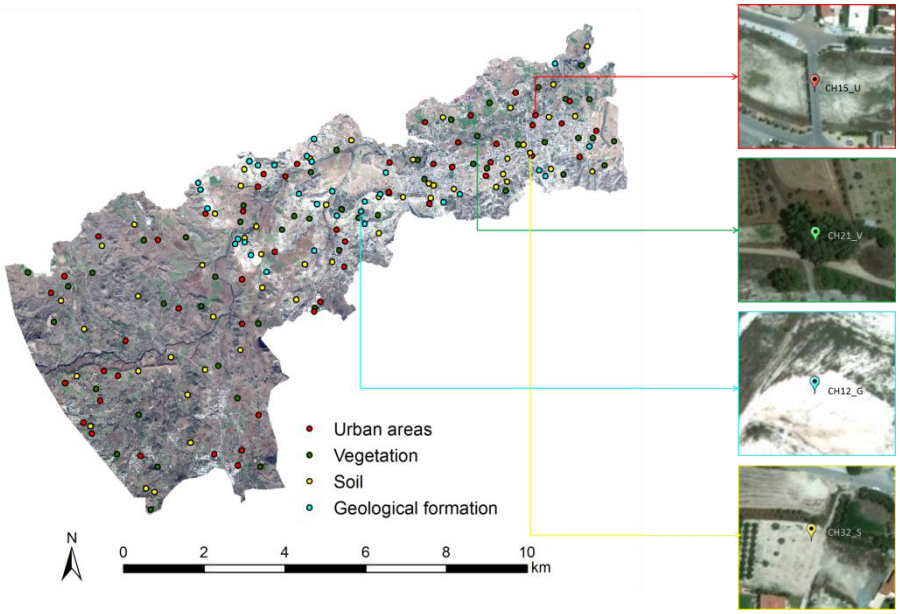

Figure 46 Ground truth points in the GeoEye-1 (left) and four examples extracted from high resolution image of 3rd December 2011 (right).

Table 30 Confusion matrix for the land use/cover map.

11-12-2011	**Ground Truth (Pixels)**				
Class	Urban areas	Vegetation	Soil	Geological formation	Total
Urban areas	43	0	1	0	44
Vegetation	0	47	3	0	50
Soil	1	3	43	0	47
Geological formation	6	0	5	30	41
Total	50	50	52	30	182
Overall Accuracy	(163/182)	89,56%			
Kappa Coefficient	0,860				

Class	**Commission (Pixels)**	**Omission (Pixels)**	**Prod. Acc. (Pixels)**	**User Acc. (Pixels)**
Urban areas	1/44	7/50	43/50	43/44
Vegetation	3/50	3/50	47/50	47/50
Soil	4/47	9/52	43/52	43/47
Geological formation	11/41	0/30	30/30	30/41

Figure 47 Example of water bodies overlaid to the GeoEye-1 and the high resolution of the 3-12-2011.

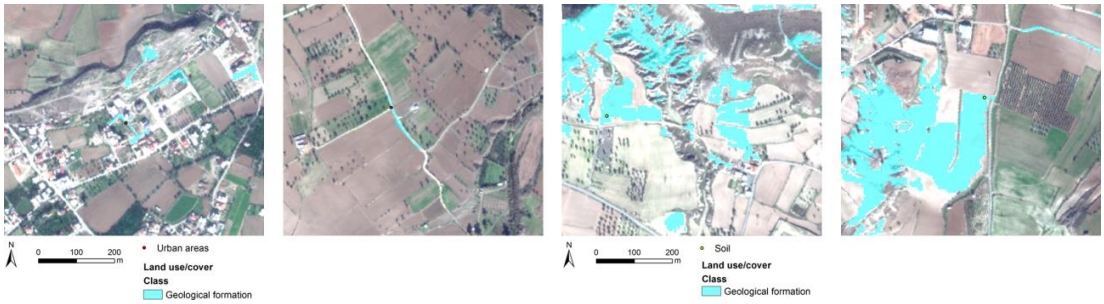

Figure 48 Examples of commission errors for the geological formation class in correspondence of urban areas (left) and soil (right) check points on the GeoEye-1.

4.2.2.3 Drainage network and morphometric parameters

The drainage network of the study area was automatically extracted from the DEM using a series of geoprocessing tools in GIS environment (Figure 49) [186]. The output of this technique produced the stream network and its classification based on Strahler system (Table 32) which designates a segment with no tributaries as a first-order stream, where two first-order stream segments join, they form a second-order stream segment and so on for the rest orders [187]. Moreover, the main linear and areal morphometric parameters, such as Drainage density (D_d), Stream frequency (F_s), Elongation ratio (R_e) and Form factor (R_f) were calculated as shown in Table 31 in order to characterized the study area [187][188][189].

Drainage density is an expression to indicate the closeness of spacing of streams and it varies with climate and vegetation, soil and rock properties, relief and landscape evolution processes [190]. Low D_d values generally indicate areas of highly resistant or permeable sub-soil material, dense vegetation and low relief; high D_d is the result of weak or impermeable sub-surface material, sparse vegetation and mountainous relief [191]. A D_d value equal to 2,19 km/km^2 was

obtained. Therefore, according to the Strahler classification, the study area is characterized by low drainage density (less than 5) suggesting rock formation with high permeability, low relief and dense vegetation. This consideration is further confirmed by a low F_s value.

Elongation ratio determines the shape of the watershed and generally ranges from values less than 0,5 to 1 for more elongated with high relief basins and circular with very low relief basins respectively [189]. Regions with low values are susceptible to more erosion whereas regions with high values correspond to high infiltration capacity and low runoff [192]. For the study area the R_e is equal to 0,62 indicating that the basin is elongated with relatively moderate relief and erosion. The low form factor equal to 0,30 confirms the elongated shape of the region [193].

Table 31 Some linear and areal morphometric parameters of the study area.

Parameter	Formula	Value	Reference
Perimeter (km)	P	75,32	
Area (km^2)	A	70,11	
Stream total number	N_u	185,00	Strahler (1964)
Stream total length (km)	L_u	153,20	Horton (1945)
Basin length (km)	L_b	15,20	Schumm (1956)
Drainage density (km/km^2)	$D_d = L_u/A$	2,19	Horton (1945)
Stream frequency (km^{-2})	$F_s = N_u/A$	2,64	Horton (1945)
Elongation ratio	$R_e = 2*(A/\pi)^{1/2}/L_b$	0,62	Schumm (1956)
Form factor	$R_f = A/L_b$^2	0,30	Horton (1945)

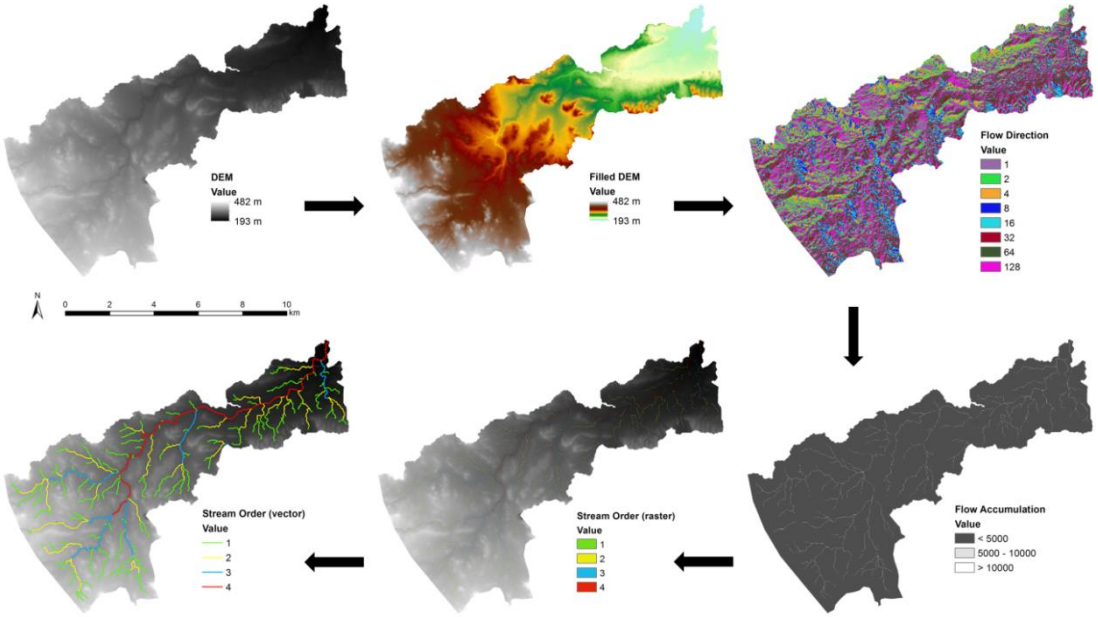

Figure 49 Extraction of drainage network from DEM.

Table 32 Stream network parameters.

Stream order	Number of stream	Number of stream (%)	Total length (km)	Mean stream length (km)
1	145	78,38	77,13	0,53
2	32	17,3	40,27	1,26
3	7	3,78	17,79	2,54
4	1	0,54	18,01	18,01

The stream network was processed within the bearing, azimuth and drainage (bAd) calculator tool to extract the drainage texture (T) of the study area, one of the criteria considered for the flood hazard map [194]. Following Smith formula, T was calculated as the product of the stream frequency and the drainage density [195]. T depends upon a number of natural factors such as climate, rainfall, vegetation, rock and soil type, infiltration capacity, relief and stage of development; soft or weak rocks unprotected by vegetation produce a fine texture, whereas massive and resistant rocks cause coarse texture [196].

The program calculates this parameter in a defined grid with a side length of 1 km. In order to generate the T spatial map, the calculated values were interpolated in GIS environment using Inverse Distance Weight (IDW) algorithm (Figure 50). The output cell size was set equal to 5 m.

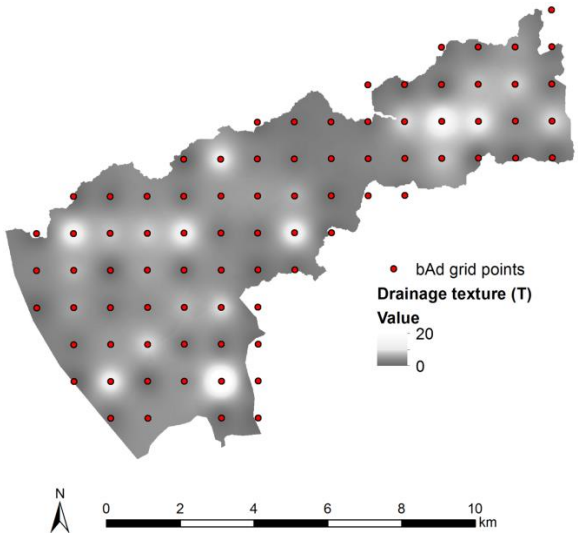

Figure 50 The grid points of bAd output and the drainage texture maps for the study area.

4.2.3 Multi-criteria analysis

The MCA analysis, performed to generate the Flood Hazard Index (FHI), incorporates slope, distance to channels, drainage texture, geology and land cover maps.

A GIS-based AHP approach was used for comparing each criterion map and determining its weight values. Finally, criteria maps and weight values were combined using a weighted linear combination:

$$FHI = \sum w_i * x_i$$

Where w_i = weight of factor i and x_i = score of factor i.

4.2.3.1 Criteria maps preparation

Because criteria were measured on different scales, the factor maps were reclassified in order to be correlated with the flood hazard. Therefore, according to the rate of contribution of each parameter to the flood hazard, rank values were assigned to each different class of each parameter (Table 33).

Slope is considered a crucial information to identify those zones that have shown high susceptibility to flooding over the years due to the low slope gradient [176]. The slope influences the direction and the amount of surface runoff reaching a site. It has a dominant effect on the contribution of rainfall to stream flow conditioning the duration of overland flow, the infiltration and the subsurface flow. Rainfall or

excess of water from a river gathers in correspondence of area characterized by low slope values; conversely, areas with high slope gradients do not permit the water accumulation. Thus, flat areas are highly subjected to water logging and flood occurrences compared to steep zones which are more exposed to surface runoff [155]. The slope map was prepared in GIS environment in percent grade using the 5 m pixel DEM of the study area; the values were subdivided into five classes as shown in Table 33 and Figure 51.

According to the records of the Department of Water Development of Cyprus the most affected areas during flooding event in Yialias River are those near the main channel as a consequence of water overflow. The main channels were extracted from the drainage network layer among streams of 3^{th} and 4^{th} orders. Thus, all the areas from both sides of the channels were mapped in GIS environment calculating the Euclidean distance. Rank value was assigned to each zone in relation to its proximity to the channels (Table 33 and Figure 52).

Drainage texture (also defined Infiltration number) is an important parameter in observing the infiltration characteristic of the basin. It is inversely proportional to the infiltration capacity; therefore, high values indicate a very low infiltration capacity resulting in high runoff triggering flooding [190][197]. Based on Smith classification of drainage texture, T values below 4 are designed as coarse; 4 – 10 as intermediate; above 10 as fine and above 15 as ultra-fine texture ultra-fine texture; values exceed 10 and 15 have fine to ultrafine texture possibly formed by the cumulative effect of various geomorphological processes [186]. According to these considerations, drainage texture map was subdivided into four class and reclassified assigning the rank values (Table 33 and Figure 53).

The geological map of the study area was obtained converting to raster the 1:250.000 map produced by the Geological Survey Department. Then, it was unified to major geological formations which were ranked considering their rate of hydraulic conductivity [198](Table 33 and Figure 54).

Rainwater runoff is much more likely on bare fields than those with a good crop cover. The presence of thick vegetative cover reduces the amount of runoff. On the other hand, impermeable surfaces such as concrete absorbs almost no water at all.

Impervious surfaces such as buildings, roads and generally urban constructions decreases the soil infiltration capacity increasing the runoff. Urbanization typically leads to the decrease in lag time and the increase in the peak discharge [155][158][199]. In compliance of these previous considerations, the land use/cover map of the study area, obtained by the GeoEye-1 processing and resampled to 5 m pixel size using mode statistic, was reclassified (Table 33 and Figure 55).

Table 33 Rank value for each criterion.

Factor	Classes	Rank
Slope (%)	< 2	9
	2 – 5	6
	5 - 8	4
	> 8	2
Distance to main channels (m)	< 50	9
	50 – 100	7
	100 – 200	6
	200 – 500	5
	500 – 1000	4
	> 1000	2
Drainage texture	<4	2
	4-10	4
	10-15	7
	>15	9
Geology	Schists	9
	Marls, Chalks	8
	Igneous rock	7
	Volcanic rocks	6
	Fanglomerate	5
	Alluvium	4
	Limestones	3
	Sandstones	2
Land use/cover	Urban areas	9
	Geological formation	7
	Soil	6
	Vegetation	4

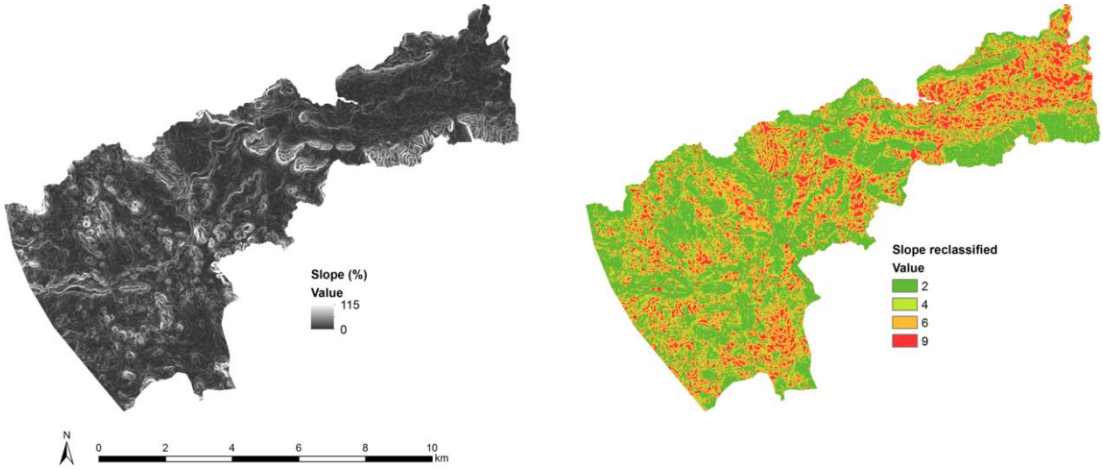

Figure 51 Slope map (left) and the reclassified map (right).

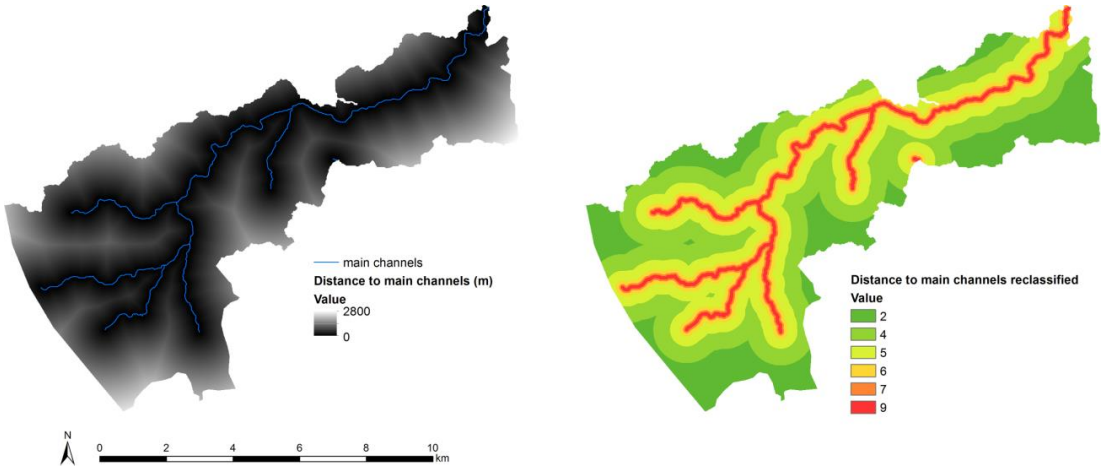

Figure 52 Distance to main channels map (left) and the reclassified map (right).

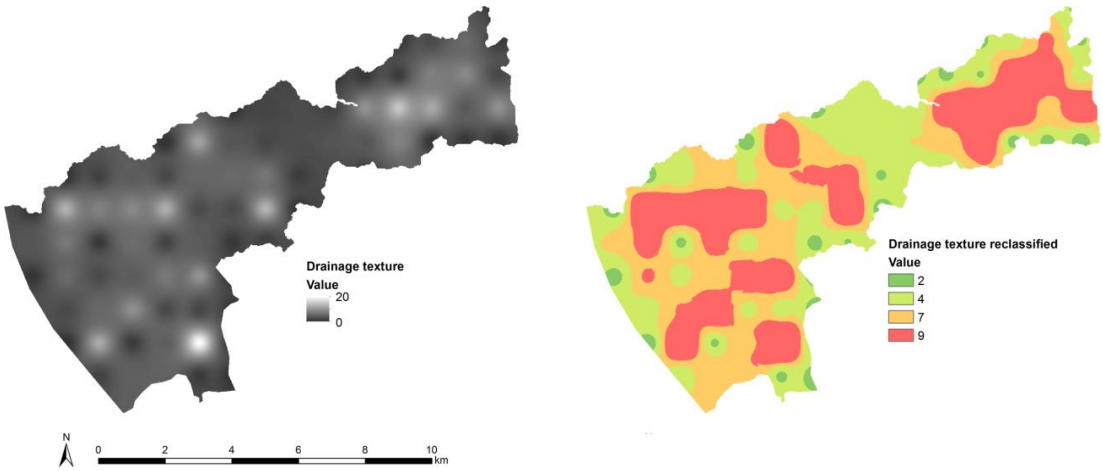

Figure 53 Drainage texture map (left) and the reclassified map (right).

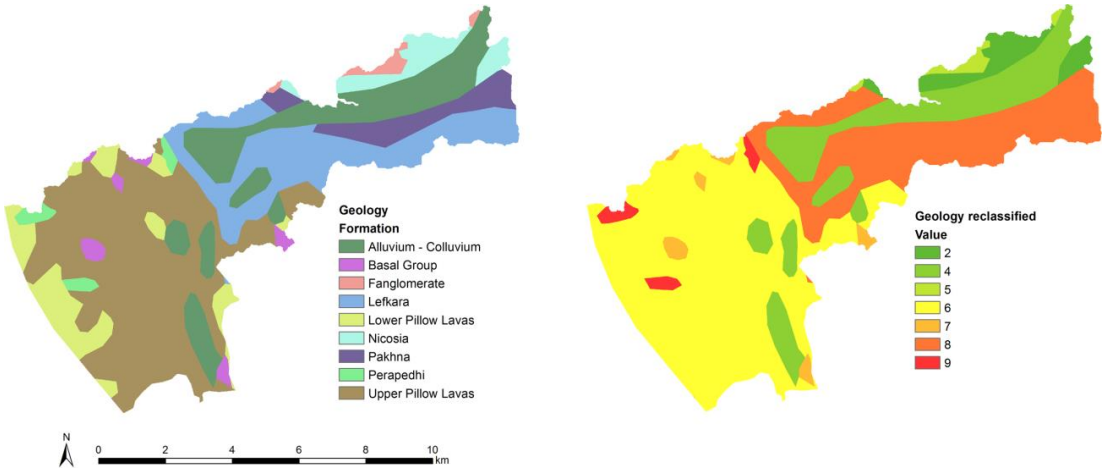

Figure 54 Geological map (left) and the reclassified map (right).

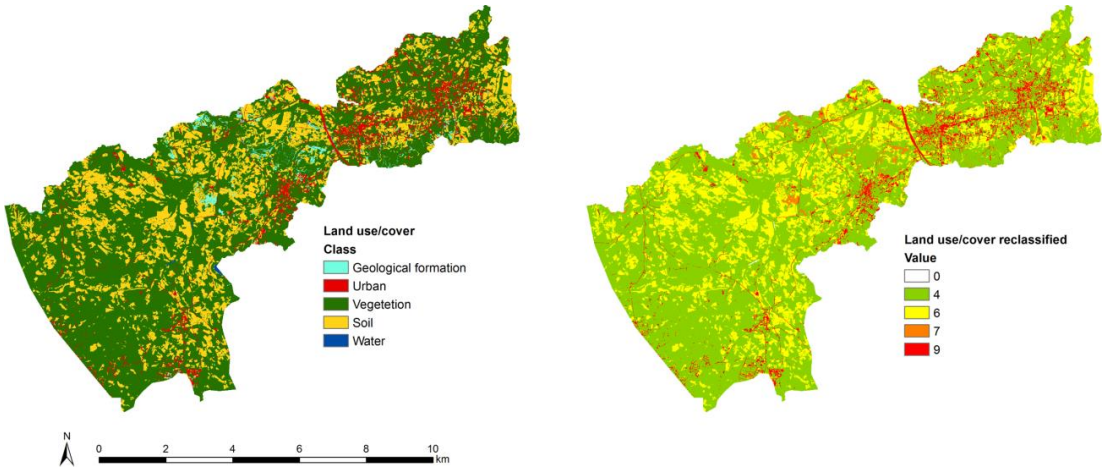

Figure 55 Land use/cover map (left) and the reclassified map (right).

4.2.3.2 AHP application

After the rank values assignation, the AHP method was used for extracting the weight of each criterion in order to consider its relative importance in the FHI calculation (4.1).

In developing weights, the pairwise comparison matrix was compiled evaluating every possible pairing. The relative importance between two criteria involved in determining the stated objective was quantified using the nine-point continuous scale (Table 34). Pairwise judgments were based on the information available and the author knowledge and experience.

The weight of each criterion can be derived by taking the principal eigenvector of the square reciprocal matrix of pairwise comparisons between the criteria. A good approximation to this result was achieved by summing the values in each column of

the pairwise comparison matrix; dividing each element in the matrix by its column total (normalized pairwise comparison matrix); and finally computing the average of the elements in each row of the normalized matrix (Table 34) [200].

To determine the degree of consistency that was used in developing the ratings consistency ratio (CR) was calculated. CR defines the probability that the matrix ratings were randomly generated and *Saaty* suggests that matrices with CR ratings greater than 0,10 should be re-evaluated. It is defined as:

$$CR = \frac{CI}{RI}$$

RI (Random Index) is the consistency index of the randomly generated pairwise comparison matrix which depends on the number of elements compared. In this case RI is equal to 1,12 [155]. CI (Consistency Index) provides a measure of departure from consistency:

$$CI = \frac{\lambda - n}{n - 1}$$

Where λ is the average value of the consistency vector and n is the number of criteria. The estimation of the CR involved the determination of the weighted sum vector by multiplying the weight for the first criterion times the first column of the original pairwise comparison matrix, then multiplying the second weight times the second column of the original pairwise matrix, and so on to the fifth weight; the sum of these values over the rows; finally, the determination of the consistency vector by dividing the weighted sum vector by the criterion weights previously determined (Table 34). A CR equal to 0,055 was achieved therefore the pairwise matrix is consistent.

Table 34 Application of AHP approach: pairwise matrix, consistency indicators and final weights.

	Slope	Distance to main channels	Drainage texture	Geology	Land cover	Weight
Slope	1	1/3	5	7	3	0,260
Distance to main channels	3	1	7	9	5	0,503
Drainage texture	1/5	1/7	1	3	1/3	0,068
Geology	1/7	1/9	1/3	1	1/5	0,035
Land use/cover	1/3	1/5	3	5	1	0,134

AHP Indicators **λ** = 5,248 **CI** = 0,062 **CR** = 0,055

Once the weights for the factors were determined, the FHI was computed in GIS environment in form of digital map (Figure 56). The FHI was calculated through the weighted linear combination of the decision factors:

$$FHI = 0{,}260 * Slope + 0{,}503 * Distance\ to\ main\ channels + 0{,}068 * Drainage\ texture + 0{,}035 * Geology + 0{,}134 * Land\ use/cover$$

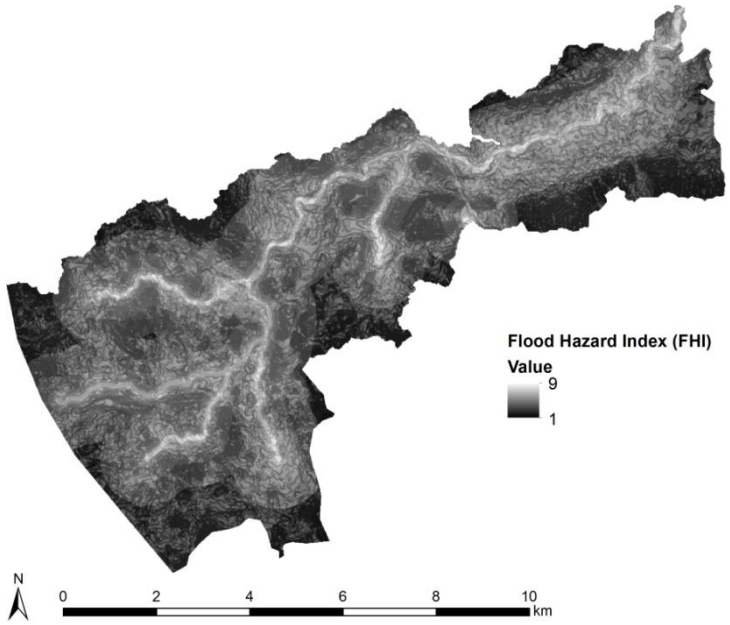

Figure 56 The FHI digital map.

4.2.4 Results

The calculated FHI values were found to be range between 1,83 – 8,96. The higher pixels value of FHI are the higher susceptible to floods conversely the lower pixels value are the lower susceptible.

For a visual and easy interpretation, qualitative hazard categories were derived by setting specific FHI thresholds. The boundaries values of each hazard class were identified computing the FHI cumulative frequency diagram (Figure 57). In particular, considering the first derivative of this curve, that allowed to identify inherent clustering pattern within the data, the FHI break values were defined. Seven hazard categories ranging from Very Low to Very High were finally used to generate the flood hazard zoning map (Figure 58).

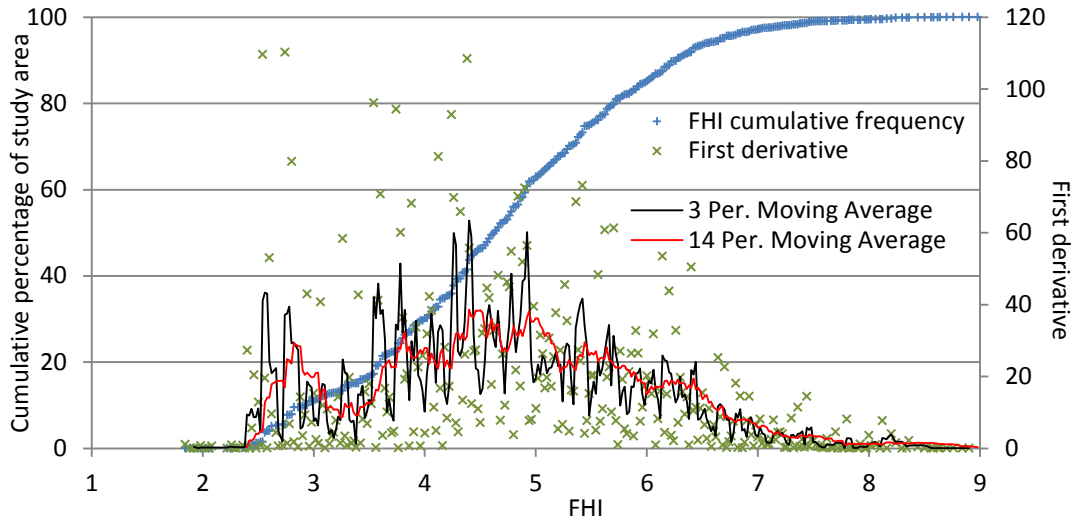

Figure 57 FHI cumulative frequency diagram.

Table 35 Classification of flood hazard index into qualitative hazard categories.

FHI values	Flood Hazard categories
< 2,8	Very Low
2,8 - 4,4	Low
4,4 - 4,9	Low to Moderate
4,9 - 5,7	Moderate
5,7 - 6,3	Moderate to High
6,3 - 7,5	High
> 7,5	Very High

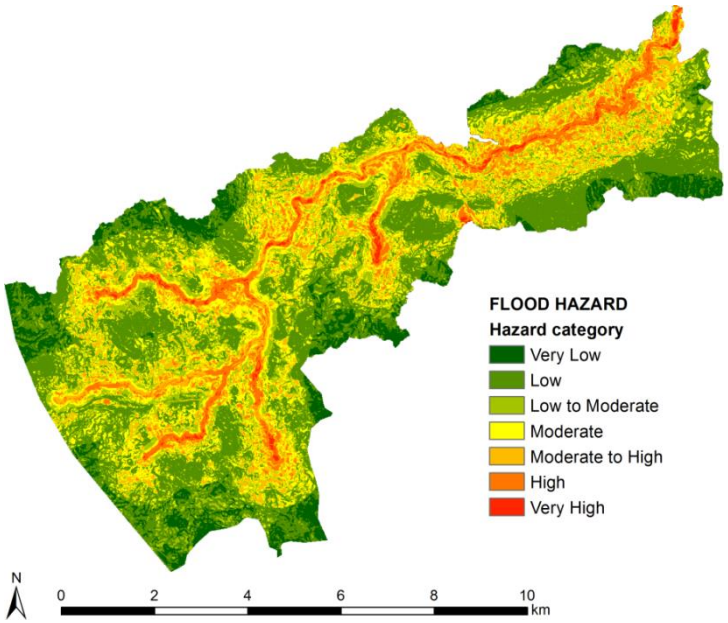

Figure 58 Flood hazard zoning map.

Table 36 shows the summary statistics computed for each hazard class, in term of covered area and percentage of the whole study area under investigation. Moreover, information about flood hazard relating to land use/cover type, obtained by GIS zonal overlay, are presented (Figure 59).

The discrepancy between the study area extension (70,11 km^2) and the total extension of the hazard mapped zones (69,91 km^2) depends on the fact that about 0,2 km^2 belongs to Water class for which it was not relevant the FHI computation.

The situation seems to be alarming in the whole length of the river, with particular reference to some sections in Phera Chorio and Dali villages where extensive anthropogenic interventions can be observed in correspondence of the riverbed (Figure 60).

Table 36 Flood hazard categories and land/use cover map comparison.

	Vegetation	Soil	Geological formation	Urban areas	**Total (km^2)**	**Total (%)**
Very Low	5,24	0,22	0,00	0,00	5,47	7,8
Low	18,30	5,34	0,49	0,85	24,98	35,7
Low to Moderate	7,11	3,09	0,22	0,53	10,95	15,7
Moderate	7,82	5,02	0,19	1,31	14,33	20,5
Moderate to High	4,65	2,34	0,07	0,57	7,63	10,9
High	3,17	1,73	0,04	0,88	5,83	8,3
Very High	0,45	0,19	0,00	0,07	0,72	1,0
Total (km^2)	46,75	17,93	1,03	4,20	69,91	100,0

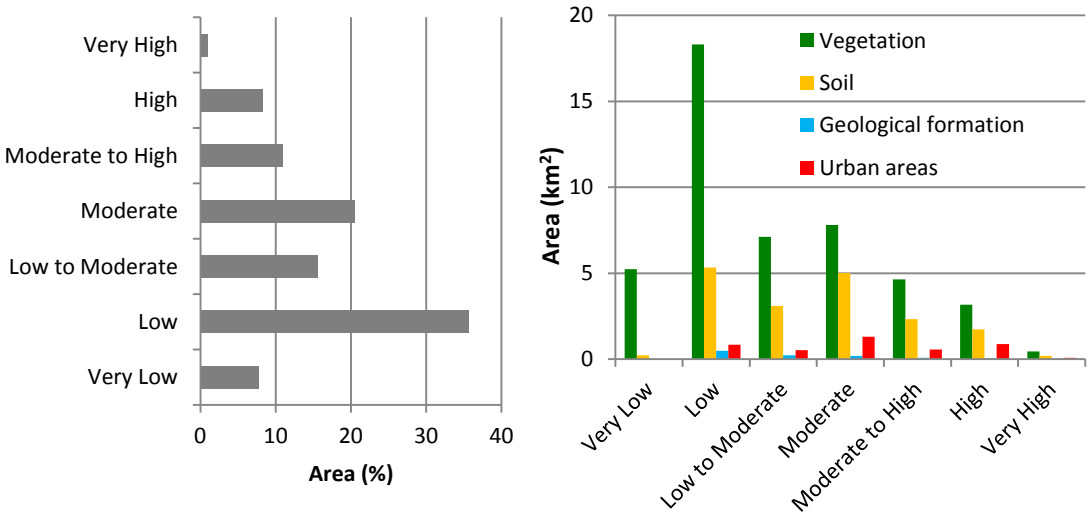

Figure 59 Percentage of study area (left) and land use/cover type (km^2) covered by each flood hazard class (right).

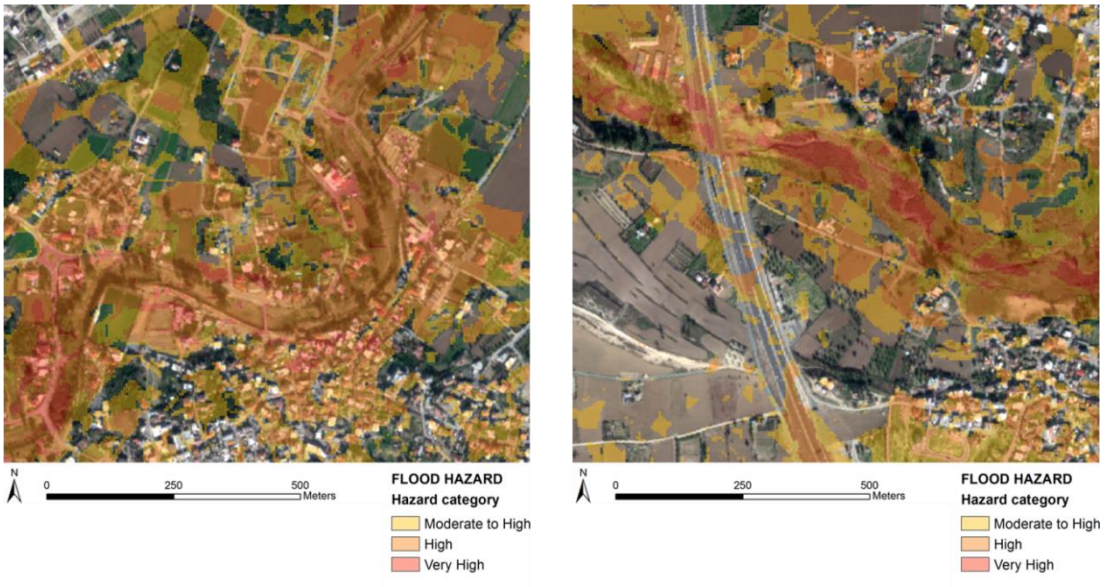

Figure 60 Flood hazard categories superimposed to GeoEye-1 satellite image; Dali village (left) and a section of the Nicosia - Limassol highway near Pera Chorio village (right).

4.2.5 Considerations

Multi-Criteria Analysis (MCA) assisted by GIS was performed to produce easily-readable and rapidly-accessible flood hazard map of the study area. Five flood-causing factors: slope, distance to main channels, drainage texture, geology and land use/cover, were considered by means of weighted linear combination to compute the Flood Hazard Index (FHI). The Analytic Hierarchy Process (AHP) approach was used for assigning the rank values to each class of the parameters and then for deriving the relative importance, the weight of each criterion in the FHI calculation. Once achieved the weight for the criteria, FHI was computed and was presented in form of flood hazard zoning map where specific FHI value ranges were associated to seven hazard categories.

To prepare necessary layers for the MCA approach, an integrated remote sensing and GIS technique was applied. Processing the 5 m pixel size DEM, slope, distance to main channels and drainage texture map were obtained. The land use/cover maps of the study area were obtained performing object-based supervised classification on the GeoEye-1 satellite image.

Regarding the classification procedure, a modular framework was created comprising two phases: segmentation and classification/refinement. A multilevel segmentation procedure was performed to achieve image objects similar to the

real-world elements; then, the classification was applied defining specific rules based on the spectral and contextual features of the image object. The modular structure developed for the procedure could be applied to other images because the user can adjust, in a simple and rapid way, segmentation parameters and rule thresholds depending on the input data.

The MCA/AHP approach was found to be useful for flood hazard assessment of the study area, where several data were not available. In fact, it has to be considered that, apart the geological map, all the other information were obtained from satellite remote sensing.

FHI was computed integrating morphological, land use/cover and topographic data, therefore it could be improved considering more information such as longer rainfall/flood records and by refining the AHP approach by working iteratively with the experts. However, the hazard zoning map can allow to deepen the knowledge about flood risk in the study area and it can be used as a first-stage analysis for identifying most vulnerable areas, to take decision in sustainable land management perspective and to formulate mitigation strategy. Moreover, specific surveys can be plan to perform more accurate analysis in correspondence of high flood hazard areas.

From the study results, it was observed that MCA/AHP along with GIS offers a flexible, step-by-step and transparent way for analysing complex problems. The technique applied can easily be extended to other areas, where other factors may be considered, depending on the availability of data.

CONCLUSIONS

The use of remote sensing for supporting various aspects of flood risk management was investigated in the present thesis. The research focused on the contribution of satellite images for three main applications: flood mapping and monitoring, flood damage assessment and flood risk assessment. Different geospatial approaches were developed regarding each phase examined.

In order to evaluate the potential of satellite remote sensing concerning flood prone areas mapping and monitoring, a Landsat time series, comprising five free cloud-cover satellite images, was collected and processed for Dhaka district territory (Bangladesh).

The image processing was performed by means of supervised classification technique, to generate multitemporal land-use/cover maps, and change detection procedure to compare them. The map of routinely flooded areas due to the heavy monsoon rains, which typically occur from May to October, was generated. Moreover, it was possible to map and quantify the recession of the water. From the comparison of three multitemporal maps (covering thirteen-year period) the impact of the urban growth and land use/cover changes on the water drainage system was analysed. Despite the lack of ground reference data, the validation procedure performed collecting ground truth points by photointerpretation, confirmed the effectiveness of Landsat images for land use/cover mapping. Moreover, they were found to be a relevant source for supporting flood detection and the monitoring of flood prone areas. The proposed methodology may be applied in other region affected by similar risk and characterized by marked seasonality, if a cloud-free multispectral time series is available.

The contribution of satellite remote sensing for the damage assessment purpose was investigated for the analysis of extreme floods occurred in Bangladesh in 2004. In this case, the research was performed by processing a Landsat image and an ASTER image in order to provide the pre-event and post-event setting of water bodies respectively. Using overlay operations in GIS environment, the flooded areas were identified and thereafter associated with the administrative divisions and land

use data of Bangladesh. The results demonstrated that satellite images, acquired before and after flooding occurrence, could allow to delineate inundated area which can be used along with other geospatial data, to support damage assessment and vulnerability analyses, which are essential for developing protective actions and mitigation plans against the flood risk.

Finally, the research focused on the use of remote sensing data for producing flood hazard maps. In this case, the study was conducted on a portion of Yialias river basin (Cyprus), often affected by flash flood. A Multi-Criteria Analysis (MCA), assisted by GIS, was performed to produce the hazard zoning map of the study area. Five flood-causing factors depending on the available data were considered: slope, distance to main channels, drainage texture land use and geology. The Analytic Hierarchy Process (AHP) technique was used for deriving the weight of each criterion in the computation of the Flood Hazard Index (FHI); then, FHI values were associated to seven hazard categories to generate easily-readable flood hazard map. Except for the geological map, the factors layers were obtained by processing a GeoEye-1 image and the Digital Elevation Model (DEM). In particular, the GeoEye-1 was classified using an object-based technique to extract land use/cover data, while geoprocessing tools in GIS environment were used to obtain the other factors from the DEM. This case study demonstrated the effectiveness and the benefit of using remote sensing data to provide valuable information concerning the hazard assessment when several data are not available. Furthermore, the MCA/AHP approach was found to be a fast and cost effective way to use remote sensing techniques, coupled with GIS, for constructing flood hazard map. It offers a flexible, step-by-step and transparent way for analysing and understanding spatial phenomena.

Natural flood disaster is common and cannot be stop. The research results highlighted the high potential of remote sensing techniques in providing valuable and objective data for flood risk management activities, relating to the identification of inundated areas, the monitoring of flood prone territory and the damage assessment after an event.

ACKNOWLEDGEMENTS

The author would like to thank ITHACA (Information Technology for Humanitarian Assistance, Cooperation and Action) and the Cyprus University of Technology - Department of Civil Engineering and Geomatics.

All the work was conducted thanks to the advices of Prof. Gabriele Bitelli who supervised the research activities.

Eng. Emanuele Mandanici gave priceless suggestions about image processing techniques.

Dr. Federico Cervi supported the multi-criteria analysis with fundamental advices.

Discussion about geospatial approaches with my colleague Eng. Alessandro Lambertini supported the research.

Thanks to my step-sisters Margherita Cecilia Spreafico and Rossella Casciere.

REFERENCES

[1] Münchener Rückversicherungs-Gesellschaft (Munich Re), "NatCatSERVICE Loss events worldwide 1980 – 2013," München, Germany, 2014.

[2] Münchener Rückversicherungs-Gesellschaft (Munich Re), "NATHAN World Map of Natural Hazards," München, Germany, 2011.

[3] C. Van Westen, "Remote sensing for natural disaster management," *Int. Arch. Photogramm. Remote Sens.*, vol. XXXIII, pp. 1609–1617, 2000.

[4] D. M. Tralli, R. G. Blom, V. Zlotnicki, A. Donnellan, and D. L. Evans, "Satellite remote sensing of earthquake, volcano, flood, landslide and coastal inundation hazards," *ISPRS J. Photogramm. Remote Sens.*, vol. 59, no. 4, pp. 185–198, Jun. 2005.

[5] J. Sanyal and X. X. Lu, "Application of Remote Sensing in Flood Management with Special Reference to Monsoon Asia: A Review," *Nat. Hazards*, vol. 33, no. 2, pp. 283–301, Oct. 2004.

[6] United Nations Department of Economic and Social Affairs (UN/DESA) Population Division, *World Urbanization Prospects: The 2014 Revision, Highlights*. New York: United Nations, 2014.

[7] M. Garschagen, P. Mucke, A. Schauber, T. Seibert, T. Welle, J. Birkmann, J. Rhyner, S. Kohler, T. Loster, D. Reinhard, and I. Matuschke, *WorldRiskReport 2014*. Bündnis Entwicklung Hilft (Alliance Development Works) and United Nations University – Institute for Environment and Human Security (UNU-EHS), 2014.

[8] J. Yoshitani, N. Takemoto, and T. Merabtene, "Factor Analysis of Water-related Disasters in Bangladesh," 2007.

[9] C. Price, A. Mugnai, K. Lagouvardos, and V. Kotroni, "High-impact floods and flash floods in Mediterranean countries: the FLASH preliminary database," *Adv. Geosci.*, vol. 23, pp. 1–9, 2010.

[10] B. Li and J. Liu, "Application of Remote Sensing Technique for Disaster Management," in *2006 IEEE International Symposium on Geoscience and Remote Sensing*, 2006, pp. 283–286.

[11] United Nations Department of Economic and Social Affairs (UN/DESA) Population Division, "World Population Prospects: The 2012 Revision. Volume I : Comprehensive Tables," New York, 2013.

[12] United Nations Inter-Agency Secretariat of the International Strategy for Disaster Reduction (UN/ISDR), *Living with Risk: A global review of disaster reduction initiatives*, vol. I. New York and Geneva: United Nations, 2004, pp. 16–30.

[13] A. Lavell, M. Oppenheimer, C. Diop, J. Hess, R. Lempert, J. Li, R. Muir-Wood, and S. Myeong, "Climate Change: New Dimensions in Disaster Risk, Exposure, Vulnerability, and Resilience," in *Managing the Risks of Extreme Events and Disasters to Advance Climate Change Adaptation*, C. B. Field, V. Barros, T. F. Stocker, D. Qi, D. J. Dokken, K. L. Ebi, M. D. Mastrandrea, K. J. Mach, G.-K. Plattner, S. K. Allen, M. Tigno, and P. M. Midgley, Eds. Cambridge, UK, and New York, NY, USA: Cambridge University Press, 2012, pp. 25–64.

[14] C. J. Van Westen, “Remote sensing and GIS for natural hazards assessment and disaster risk management,” in *Treatise on Geomorphology*, vol. 3, J. Shroder and M. P. Bishop, Eds. Elsevier, 2013, pp. 259–298.

[15] J. C. Villagrán de León, *Vulnerability. A Conceptual and Methodological Review*, vol. 4. Paffenholz, Bornheim, Germany, 2006.

[16] D. Crichton, “UK and Global Insurance Responses to Flood Hazard,” in *Non-structural measures for water management problems*, 2002, no. 56, pp. 239–251.

[17] M. Dilley, R. S. Chen, U. Deichmann, A. L. Lerner-Lam, M. Arnold, J. Agwe, P. Buys, O. Kjekstad, B. Lyon, and Y. Gregory, *Natural Disaster Hotspots. A Global Risk Analysis*. Washington, D.C. U.S.A., 2005.

[18] T. J. Cova, “GIS in emergency management,” in *Geographical Information Systems: Principles, Techniques, Applications, and Management*, P. A. Longley, M. F. Goodchild, D. J. Maguire, and D. V. Rhind, Eds. New York: John Wiley & Sons, 1999, pp. 845–858.

[19] D. E. Alexander, *Confronting Catastrophe: New perspectives on natural disasters.* Oxford New York: Oxford University Press, 2000.

[20] H. Taubenböck, J. Post, A. Roth, K. Zosseder, G. Strunz, and S. Dech, “A conceptual vulnerability and risk framework as outline to identify capabilities of remote sensing,” *Nat. Hazards Earth Syst. Sci.*, vol. 8, no. 3, pp. 409–420, May 2008.

[21] O. M. Bello and Y. A. Aina, “Satellite remote sensing as a tool in disaster management and sustainable development: towards a synergistic approach,” *Procedia - Soc. Behav. Sci.*, vol. 120, pp. 365–373, Mar. 2014.

[22] P. Boccardo, “New perspectives in emergency mapping,” *Eur. J. Remote Sens.*, vol. 46, pp. 571–582, Jul. 2013.

[23] K. E. Joyce, S. E. Belliss, S. V. Samsonov, S. J. McNeill, and P. J. Glassey, “A review of the status of satellite remote sensing and image processing techniques for mapping natural hazards and disasters,” *Prog. Phys. Geogr.*, vol. 33, no. 2, pp. 183–207, Jun. 2009.

[24] F. Dell’Acqua, C. Bignami, M. Chini, G. Lisini, D. A. Polli, and S. Stramondo, “Earthquake Damages Rapid Mapping by Satellite Remote Sensing Data: L’Aquila April 6th, 2009 Event,” *IEEE J. Sel. Top. Appl. Earth Obs. Remote Sens.*, vol. 4, no. 4, pp. 935–943, Dec. 2011.

[25] R. Casciere, F. Franci, and G. Bitelli, “Use of Landsat imagery to detect land cover changes for monitoring soil sealing; case study: Bologna province (Italy),” in *Proc. 2nd International Conference on Remote Sensing and Geoinformation of the Environment (RSCy2014)*, 2014, p. 92290V.

[26] H. Guo, Y. Chen, Q. Feng, Q. Lin, and F. Wang, “Assessment of damage to buildings and farms during the 2011 M 9.0 earthquake and tsunami in Japan from remote sensing data,” *Chinese Sci. Bull.*, vol. 56, no. 20, pp. 2138–2144, Jul. 2011.

[27] B. A. Margono, S. Turubanova, I. Zhuravleva, P. Potapov, A. Tyukavina, A. Baccini, S. Goetz, and M. C. Hansen, “Mapping and monitoring deforestation and forest degradation in Sumatra (Indonesia) using Landsat time series data sets from 1990 to 2010,” *Environ. Res. Lett.*, vol. 7, no. 3, Sep. 2012.

[28] P. Chen, S. C. Liew, and L. K. Kwoh, “Tsunami damage assessment using high resolution satellite imagery: a case study of Aceh, Indonesia,” in *IEEE International Geoscience and Remote Sensing Symposium, 2005*, 2005, vol. 2, pp. 1405–1408.

[29] D. Ehrlich, H. D. Guo, K. Molch, J. W. Ma, and M. Pesaresi, “Identifying damage caused by the 2008 Wenchuan earthquake from VHR remote sensing data,” *Int. J. Digit. Earth*, vol. 2, no. 4, pp. 309–326, Dec. 2009.

[30] A. M. F. Lagmay and Project NOAH Storm Surge Component Team, “Devastating storm surges of Typhoon Haiyan,” *Project NOAH Open-File Reports*, vol. 3, no. 6. pp. 45–56, Mar-2015.

[31] G. Bitelli, R. Camassi, L. Gusella, and A. Mognol, “IMAGE CHANGE DETECTION ON URBAN AREA : THE EARTHQUAKE CASE,” *Int. Arch. Photogramm. Remote Sens. Spat. Inf. Sci.*, vol. XXXV, no. Part B, pp. 692–697, 2004.

[32] K. E. Joyce, K. C. Wright, S. V. Samsonov, and V. G. Ambrosia, “Remote sensing and the disaster management cycle,” in *Advances in Geoscience and Remote Sensing*, G. Jedlovec, Ed. InTech, 2009, pp. 317–346.

[33] A. Stumpf and N. Kerle, “Object-oriented mapping of landslides using Random Forests,” *Remote Sens. Environ.*, vol. 115, no. 10, pp. 2564–2577, Oct. 2011.

[34] S. Lewis, “Remote sensing for natural disasters: Facts and figures.” [Online]. Available: http://www.scidev.net/global/earth-science/feature/remote-sensing-for-natural-disasters-facts-and-figures.html?from=related articles.

[35] D. Pieri and M. Abrams, “ASTER watches the world’s volcanoes: a new paradigm for volcanological observations from orbit,” *J. Volcanol. Geotherm. Res.*, vol. 135, no. 1–2, pp. 13–28, Jul. 2004.

[36] G. P. Petropoulos, W. Knorr, M. Scholze, L. Boschetti, and G. Karantounias, “Combining ASTER multispectral imagery analysis and support vector machines for rapid and cost-effective post-fire assessment: a case study from the Greek wildland fires of 2007,” *Nat. Hazards Earth Syst. Sci.*, vol. 10, no. 2, pp. 305–317, Feb. 2010.

[37] Natural Resources Canada, “Thermal Imaging,” 2014. [Online]. Available: http://www.nrcan.gc.ca/earth-sciences/geomatics/satellite-imagery-air-photos/satellite-imagery-products/educational-resources/9319.

[38] T. Strozzi, U. Wegmiiller, L. Tosl, G. Bitelli, and V. Spreckels, “Land Subsidence Monitoring with Differential SAR Interferometry,” *Photogramm. Eng. Remote Sens.*, vol. 67, no. 11, pp. 1261–1270, 2001.

[39] G. Bitelli, F. Bonsignore, S. Del Conte, F. Novali, I. Pellegrino, and L. Vittuari, “Integrated Use of Advanced InSAR and GPS Data for Subsidence Monitoring,” in *Engineering Geology for Society and Territory - Volume 5*, G. Lollino, A. Manconi, F. Guzzetti, M. Culshaw, P. Bobrowsky, and F. Luino, Eds. Springer International Publishing, 2015, pp. 147–150.

[40] M. C. Spreafico, F. Franci, G. Bitelli, A. L. Valentina Alena Girelli, C. C. Lucente, E. Mandanici, M. A. Tini, and L. Borgatti, “Remote Sensing Techniques in a Multidisciplinary Approach for the Preservation of Cultural Heritage Sites from Natural Hazard: The Case of Valmarecchia Rock Slabs (RN, Italy),” in *Engineering Geology for Society and Territory - Volume 8*, G. Lollino,

D. Giordan, C. Marunteanu, B. Christaras, I. Yoshinori, and C. Margottini, Eds. Springer International Publishing, 2015, pp. 317–321.

[41] C. Bignami, P. Burrato, V. Cannelli, M. Chini, E. Falcucci, A. Ferretti, S. Gori, C. Kyriakopoulos, D. Melini, M. Moro, F. Novali, M. Saroli, S. Stramondo, G. Valensise, and P. Vannoli, "2012 EMILIA EARTHQUAKES Coseismic deformation pattern of the Emilia 2012 seismic sequence imaged by Radarsat-1 interferometry," *Ann. Geophys.*, vol. 55, no. 4, pp. 789–795, 2012.

[42] S. Dellepiane, E. Angiati, and G. Vernazza, "Processing and segmentation of COSMO-SkyMed images for flood monitoring," in *2010 IEEE International Geoscience and Remote Sensing Symposium*, 2010, no. I, pp. 4807–4810.

[43] S. B. Serpico, S. Dellepiane, G. Boni, G. Moser, E. Angiati, and R. Rudari, "Information Extraction From Remote Sensing Images for Flood Monitoring and Damage Evaluation," *Proc. IEEE*, vol. 100, no. 10, pp. 2946–2970, Oct. 2012.

[44] "The International Charter." [Online]. Available: www.disasterscharter.org.

[45] "UNITAR's Operational Satellite Applications Programme - UNOSAT." [Online]. Available: www.unitar.org/unosat.

[46] "UN-SPIDER." [Online]. Available: www.un-spider.org.

[47] "Copernicus - The European Earth Observation Programme." [Online]. Available: www.copernicus.eu.

[48] "JAXA - Japan Aerospace Exploration Agency." [Online]. Available: http://global.jaxa.jp/article/special/sentinel_asia/index_e.html.

[49] "ITHACA - Information Technology for Humanitarian Assistance, Cooperation and Action." [Online]. Available: http://www.ithaca.polito.it/.

[50] "Center for Satellite Based Crisis Information." [Online]. Available: www.zki.dlr.de.

[51] "SERTIT." [Online]. Available: sertit.u-strasbg.fr.

[52] "Global Disaster Alert and Coordination System." [Online]. Available: www.gdacs.org.

[53] "Dartmouth Flood Observatory." [Online]. Available: floodobservatory.colorado.edu.

[54] O. Altan, R. Backhaus, P. Boccardo, F. G. Tonolo, J. Trinder, N. van Manen, S. Zlatanova, and Book, Eds., *The Value of Geoinformation for Disaster and Risk Management (VALID) Benefit Analysis and Stakeholder Assessment*. Copenhagen, Denmark: Joint Board of Geospatial Information Societies, 2013.

[55] J. Sanyal and X. X. Lu, "Application of Remote Sensing in Flood Management with Special Reference to Monsoon Asia: A Review," *Nat. Hazards*, vol. 33, no. 2, pp. 283–301, Oct. 2004.

[56] H. Taubenböck, M. Wurm, M. Netzband, H. Zwenzner, a. Roth, a. Rahman, and S. Dech, "Flood risks in urbanized areas – multi-sensoral approaches using remotely sensed data for risk assessment," *Nat. Hazards Earth Syst. Sci.*, vol. 11, no. 2, pp. 431–444, Feb. 2011.

[57] S. K. Jain, A. K. Saraf, A. Goswami, and T. Ahmad, “Flood inundation mapping using NOAA AVHRR data,” *Water Resour. Manag.*, vol. 20, no. 6, pp. 949–959, Sep. 2006.

[58] A. Dewan, “Hazards, Risk, and Vulnerability,” in *Floods in a Megacity: Geospatial Techniques in Assessing Hazards, Risk and Vulnerability*, Dordrecht: Springer Netherlands, 2013, pp. 35–74.

[59] B. Büchele, H. Kreibich, a. Kron, a. Thieken, J. Ihringer, P. Oberle, B. Merz, and F. Nestmann, “Flood-risk mapping: contributions towards an enhanced assessment of extreme events and associated risks,” *Nat. Hazards Earth Syst. Sci.*, vol. 6, no. 4, pp. 485–503, Jun. 2006.

[60] V. Bhanumurthy, P. Manjusree, and G. Srinivasa Rao, “Flood Disaster Management,” in *Remote Sensing Applications*, P. S. Roy, R. S. Dwivedi, and D.Vijayan, Eds. Hyderabad, India: National Remote Sensing Center, 2010, pp. 283–296.

[61] “Landsat mission.” [Online]. Available: http://landsat.usgs.gov/index.php.

[62] L. Smith, “Satellite remote sensing of river inundation area, stage, and discharge: A review,” *Hydrol. Process.*, vol. 11, pp. 1427–1439, 1997.

[63] P. S. Frazier and K. J. Page, “Water Body Detection and Delineation with Landsat TM Data,” *Photogramm. Eng. Remote Sens.*, vol. 66, no. 12, pp. 1461–1467, 2000.

[64] Y. Wang, J. D. Colby, and K. A. Mulcahy, “An efficient method for mapping flood extent in a coastal floodplain using Landsat TM and DEM data,” *Int. J. Remote Sens.*, vol. 23, no. 18, pp. 3681–3696, 2002.

[65] S. N. Goward, J. G. Masek, D. L. Williams, J. R. Irons, and R. J. Thompson, “The Landsat 7 mission. Terrestrial research and applications for the 21st century,” *Remote Sens. Environ.*, vol. 78, no. 1–2, pp. 3–12, Oct. 2001.

[66] M. Gianinetto, P. Villa, and G. Lechi, “Postflood damage evaluation using Landsat TM and ETM+ data integrated with DEM,” *IEEE Trans. Geosci. Remote Sens.*, vol. 44, no. 1, pp. 236–243, Jan. 2006.

[67] Y. Wang, “Using Landsat 7 TM data acquired days after a flood event to delineate the maximum flood extent on a coastal floodplain,” *Int. J. Remote Sens.*, vol. 25, no. 5, pp. 959–974, Mar. 2004.

[68] R. F. Thomas, R. T. Kingsford, Y. Lu, and S. J. Hunter, “Landsat mapping of annual inundation (1979–2006) of the Macquarie Marshes in semi-arid Australia,” *Int. J. Remote Sens.*, vol. 32, no. 16, pp. 4545–4569, Aug. 2011.

[69] G. Mallinis, I. Z. Gitas, V. Giannakopoulos, F. Maris, and M. Tsakiri-Strati, “An object-based approach for flood area delineation in a transboundary area using ENVISAT ASAR and LANDSAT TM data,” *Int. J. Digit. Earth*, vol. 6, no. 2, pp. 1–13, Dec. 2011.

[70] S. K. Jain, R. D. Singh, M. K. Jain, and a. K. Lohani, “Delineation of Flood-Prone Areas Using Remote Sensing Techniques,” *Water Resour. Manag.*, vol. 19, no. 4, pp. 333–347, Aug. 2005.

[71] H. A. Ganaie, H. Hashia, and D. Kalota, “Delineation of Flood Prone Area using Normalized Difference Water Index (NDWI) and Transect Method : A Case Study of Kashmir Valley,” *Int. J. Remote Sens. Appl.*, vol. 3, no. 2, pp. 53–58, 2013.

[72] L. T. K. Ho, M. Umitsu, and Y. Yamaguchi, “Flood hazard mapping by satellite images and SRTM DEM in the Vu Gia–Thu Bon alluvial plain, Central Vietnam,” *Int. Arch. Photogramm. Remote Sens. Spat. Inf. Sci.*, vol. XXXVIII, no. Part 8, pp. 275–280, 2010.

[73] J. A. M. De Brouder, “Flood study in the Meghna-Dhonagoda polder, Bangladesh,” in *15th Asian conference on remote sensing*, 1994, pp. 1–9.

[74] W. K. Michener and P. F. Houhoulis, “Detection of Vegetation Changes Associated with Extensive Flooding in a Forested Ecosystem,” *Photogramm. Eng. Remote Sens.*, vol. 63, no. 12, pp. 1363–1374, 1997.

[75] A. Dia, J. L. Kouame, J.-P. Rudant, and S. Wade, “Use of Satellite Images to map Flood Extension around the city of Saint Louis in the Senegal River Estuary,” *Jàmbá J. Disaster Risk Stud.*, vol. 1, no. 1, pp. 24–33, Apr. 2006.

[76] P. Worsley and J. Bowler, “Assessing flood damage using SPOT and NOAA AVHRR data,” in *Geospatial Information in Agriculture 2001*, 2001, pp. 2–7.

[77] C. J. Ticehurst, Y. Chen, F. Karim, D. Dutta, and B. Gouweleeuw, “Using MODIS for mapping flood events for use in hydrological and hydrodynamic models : Experiences so far,” in *20th International Congress on Modelling and Simulation*, 2013, pp. 1–9.

[78] X. Zhan, R. A. Sohlberg, J. R. G. Townshend, C. DiMiceli, M. L. Carroll, J. C. Eastman, M. C. Hansen, and R. S. DeFries, “Detection of land cover changes using MODIS 250 m data,” *Remote Sens. Environ.*, vol. 83, pp. 336–350, Nov. 2002.

[79] R. Brakenridge and E. Anderson, “MODIS-BASED FLOOD DETECTION, MAPPING AND MEASUREMENT: THE POTENTIAL FOR OPERATIONAL HYDROLOGICAL APPLICATIONS,” in *Transboundary Floods: Reducing Risks Through Flood Management*, J. Marsalek, G. Stancalie, and G. Balint, Eds. Dordrecht: Kluwer Academic Publishers, 2006, pp. 1–12.

[80] T. Sakamoto, N. Van Nguyen, A. Kotera, H. Ohno, N. Ishitsuka, and M. Yokozawa, “Detecting temporal changes in the extent of annual flooding within the Cambodia and the Vietnamese Mekong Delta from MODIS time-series imagery,” *Remote Sens. Environ.*, vol. 109, no. 3, pp. 295–313, Aug. 2007.

[81] C. Ticehurst, J. Guerschman, and C. Yun, “The Strengths and Limitations in Using the Daily MODIS Open Water Likelihood Algorithm for Identifying Flood Events,” *Remote Sens.*, vol. 6, no. 12, pp. 11791–11809, Nov. 2014.

[82] J. Shimakage and F. Yamazaki, “Detection of flooded areas following the 2011 Thailand floods using ASTER images,” in *Proc. 33rd Asian Conference on Remote Sensing*, 2012, pp. 2462–2479.

[83] K. Kouchi and F. Yamazaki, “Characteristics of Tsunami-Affected Areas in Moderate-Resolution Satellite Images,” *IEEE Trans. Geosci. Remote Sens.*, vol. 45, no. 6, pp. 1650–1657, Jun. 2007.

[84] D. Hanada and F. Yamazaki, “DETECTION OF FLOODED AREAS BY THE TOHOKU EARTHQUAKE/TSUNAMI USING ASTER THERMAL INFRARED IMAGES,” in *9th International Conference on Urban Earthquake Engineering/ 4th Asia Conference on Earthquake Engineering*, 2012, pp. 235–239.

[85] C. Domenikiotis, A. Loukas, N. R. Dalezios, N. R. D. The, and N. Avhrr, “The use of NOAA/AVHRR satellite data for monitoring and assessment of forest fires and floods,” *Nat. Hazards Earth Syst. Sci.*, vol. 3, pp. 115–128, 2003.

[86] “NOAA SATELLITE INFORMATION SYSTEM.” [Online]. Available: http://noaasis.noaa.gov/NOAASIS/ml/avhrr.html.

[87] D. R. Wiesnet, D. F. McGinnis, and J. A. Pritchard, “MAPPING OF THE 1973 MISSISSIPPI RIVER FLOODS BY THE NOAA-2 SATELLITE,” *J. Am. Water Resour. Assoc.*, vol. 10, no. 5, pp. 1040–1049, Oct. 1974.

[88] R. Bryant and M. Rainey, “Investigation of flood inundation on playas within the Zone of Chotts, using a time-series of AVHRR,” *Remote Sens. Environ.*, vol. 82, pp. 360–375, 2002.

[89] G. Mahé and D. Orange, “Estimation of the flooded area of the Inner Delta of the River Niger in Mali by hydrological balance and satellite data,” *Hydro-climatology Var. Chang.*, no. July, pp. 138–143, 2011.

[90] Q. Wang, M. Watanabe, S. Hayashi, and S. Murakami, “Using NOAA AVHRR Data to Assess Flood Damage in China,” *Environ. Monit. Assess.*, vol. 82, no. 2, pp. 119–148, 2003.

[91] C. J. van der Sande, S. M. de Jong, and A. P. J. de Roo, “A segmentation and classification approach of IKONOS-2 imagery for land cover mapping to assist flood risk and flood damage assessment,” *Int. J. Appl. Earth Obs. Geoinf.*, vol. 4, no. 3, pp. 217–229, Jun. 2003.

[92] A. Shaker, W. Y. Yan, and N. El-ashmawy, “Panchromatic Assessment Satellite Image Classification for Flood,” *J. Appl. Res. Technol.*, vol. 10, pp. 902–911, 2012.

[93] D. McLaren, J. Doubleday, and S. Chien, “Using WorldView-2 imagery to track flooding in Thailand in a multi-asset sensorweb,” in *Algorithms and Technologies for Multispectral, Hyperspectral, and Ultraspectral Imagery XVIII*, 2012, vol. 8390, pp. 1–8.

[94] M. Pesaresi, A. Gerhardinger, and F. Haag, “Rapid damage assessment of built-up structures using VHR satellite data in tsunami-affected areas,” *Int. J. Remote Sens.*, vol. 28, no. 13–14, pp. 3013–3036, Jul. 2007.

[95] N. Kussul, A. Shelestov, and S. Skakun, “Flood Monitoring from SAR Data,” in *Use of Satellite and In-Situ Data to Improve Sustainability*, F. Kogan, A. Powell, and O. Fedorov, Eds. Dordrecht: Springer Netherlands, 2011, pp. 19–29.

[96] “esa Earth Online.” [Online]. Available: https://earth.esa.int/web/guest/missions.

[97] “RADARSAT Constellation.” [Online]. Available: http://www.asc-csa.gc.ca/eng/satellites/radarsat/.

[98] “COSMO-SkyMed Sistema duale per l’osservazione della Terra.” [Online]. Available: http://www.asi.it/it/attivita/osservazione_terra/cosmoskymed.

[99] “About ALOS - PALSAR.” [Online]. Available: http://www.eorc.jaxa.jp/ALOS/en/about/palsar.htm.

[100] “TerraSAR-X Image Product Guide.” [Online]. Available: http://www.geo-airbusds.com/en/903-technical-information.

[101] D. U. Lawal, A.-N. Matori, A. M. Hashim, I. A. Chandio, S. Sabri, A.-L. Balogun, and H. A. Abba, “Geographic Information System and Remote Sensing Applications in Flood Hazards Management: A Review,” *Res. J. Appl. Sci. Eng. Technol.*, vol. 3, no. 9, pp. 933–947, 2011.

[102] T. Y. Gan, F. Zunic, C.-C. Kuo, and T. Strobl, “Flood mapping of Danube River at Romania using single and multi-date ERS2-SAR images,” *Int. J. Appl. Earth Obs. Geoinf.*, vol. 18, pp. 69–81, Aug. 2012.

[103] P. A. Brivio, R. Colombo, M. Maggi, and R. Tomasoni, “Integration of remote sensing data and GIS for accurate mapping of flooded areas,” *Int. J. Remote Sens.*, vol. 23, no. 3, pp. 429–441, Nov. 2002.

[104] K. Komwong and R. Simking, “ALOS PALSAR AND RADARSAT APPLICATIONS ON FLASH FLOOD DETECTION IN THE LOWER NORTH OF THAILAND,” in *Asian Conference on Remote Sensing*, 2006.

[105] S. Martinis, a. Twele, and S. Voigt, “Towards operational near real-time flood detection using a split-based automatic thresholding procedure on high resolution TerraSAR-X data,” *Nat. Hazards Earth Syst. Sci.*, vol. 9, no. 2, pp. 303–314, Mar. 2009.

[106] J. B. Henry, P. Chastanet, K. Fellah, and Y. L. Desnos, “ENVISAT multipolarised ASAR data for flood mapping,” in *IEEE International Geoscience and Remote Sensing Symposium*, 2003, vol. 2, pp. 1136–1138.

[107] S. Plank, “Rapid Damage Assessment by Means of Multi-Temporal SAR — A Comprehensive Review and Outlook to Sentinel-1,” *Remote Sens.*, vol. 6, no. 6, pp. 4870–4906, May 2014.

[108] L. Giustarini, R. Hostache, P. Matgen, G. J.-P. Schumann, P. D. Bates, and D. C. Mason, “A Change Detection Approach to Flood Mapping in Urban Areas Using TerraSAR-X,” *IEEE Trans. Geosci. Remote Sens.*, vol. 51, no. 4, pp. 2417–2430, Apr. 2013.

[109] G. Nico, M. Pappalepore, G. Pasquariello, A. Refice, and S. Samarelli, “Comparison of SAR amplitude vs. coherence flood detection methods - a GIS application,” *Int. J. Remote Sens.*, vol. 21, no. 8, pp. 1619–1631, Nov. 2000.

[110] L. Pulvirenti, M. Chini, N. Pierdicca, L. Guerriero, and P. Ferrazzoli, “Flood monitoring using multi-temporal COSMO-SkyMed data: Image segmentation and signature interpretation,” *Remote Sens. Environ.*, vol. 115, no. 4, pp. 990–1002, Apr. 2011.

[111] R. Heremans, A. Willekens, D. Borghys, B. Verbeeck, J. Valckenborgh, M. Acheroy, and C. Perneel, “Automatic detection of flooded areas on ENVISAT/ASAR images using an object-oriented classification technique and an active contour algorithm,” in *International Conference on Recent Advances in Space Technologies, 2003*, 2003, pp. 311–316.

[112] N. Pierdicca, L. Pulvirenti, M. Chini, G. Boni, G. Squicciarino, and L. Candela, “Flood mapping by SAR: Possible approaches to mitigate errors due to ambiguous radar signatures,” in *IEEE Geoscience and Remote Sensing Symposium*, 2014, pp. 3850–3853.

[113] Y. Cunjian, W. Siyuan, Z. Zengxiang, and H. Shifeng, “Extracting the flood extent from satellite SAR image with the support of topographic data,” in *International Conferences on Info-Tech and Info-Net*, 2001, pp. 87–92.

[114] T. Alipour Fard, M. Hasanlou, and H. Arefi, “Classifier Fusion of High-Resolution Optical and Synthetic Aperture Radar (Sar) Satellite Imagery for Classification in Urban Area,” *ISPRS - Int.*

Arch. Photogramm. Remote Sens. Spat. Inf. Sci., vol. XL–2/W3, no. November, pp. 25–29, Oct. 2014.

[115] N. Chaouch, M. Temimi, S. Hagen, J. Weishampel, S. Medeiros, and R. Khanbilvardi, "A synergetic use of satellite imagery from SAR and optical sensors to improve coastal flood mapping in the Gulf of Mexico," *Hydrol. Process.*, vol. 26, no. 11, pp. 1617–1628, May 2012.

[116] J. Töyrä, A. Pietroniro, and L. W. Martz, "Multisensor Hydrologic Assessment of a Freshwater Wetland," *Remote Sens. Environ.*, vol. 75, no. 2, pp. 162–173, Feb. 2001.

[117] J. Senthilnath, S. N. Omkar, V. Mani, and P. G. Diwakar, "Multi-Temporal Satellite Imagery for Flood Damage Assessment," *J. Indian Inst. Sci.*, vol. 93, no. 1, pp. 105–116, 2013.

[118] C. Pohl and J. L. Van Genderen, "Review article Multisensor image fusion in remote sensing: Concepts, methods and applications," *Int. J. Remote Sens.*, vol. 19, no. 5, pp. 823–854, Jan. 1998.

[119] S. Yonghua, L. Xiaojuan, G. Huili, Z. Wenji, and G. Zhaoning, "A study on optical and SAR data fusion for extracting flooded area," in *IEEE International Geoscience and Remote Sensing Symposium*, 2007, pp. 3086–3089.

[120] C. Dey, X. Jia, and D. Fraser, "Decision Fusion for Reliable Flood Mapping Using Remote Sensing Images," in *Digital Image Computing: Techniques and Applications*, 2008, pp. 184–190.

[121] S. Kuehn, U. Benz, and J. Hurley, "Efficient flood monitoring based on RADARSAT-1 images data and information fusion with object-oriented technology," in *IEEE International Geoscience and Remote Sensing Symposium*, 2002, vol. 5, pp. 2862–2864.

[122] United Nations Human Settlements Programme (UN-HABITAT), *THE STATE OF THE WORLD'S CITIES REPORT 2006/2007*. EARTHSCAN, 2006.

[123] N. Islam Khan, "Temporal mapping and spatial analysis of land transformation due to urbanization and its impact on surface water system: a case from Dhaka metropolitan area, Bangladesh," *Int. Arch. Photogramm. Remote Sens.*, vol. XXXIII, pp. 598–605, 2000.

[124] M. S. Islam, T. Hossain, S. F. Ameen, E. Hoque, and S. Ahamed, "Earthquake induced liquefaction vulnerability of reclaimed areas of Dhaka," *J. Civ. Eng.*, vol. 38, no. 1, pp. 65–80, 2010.

[125] M. S. Islam, M. Nasrin, and A. J. Khan, "FOUNDATION ALTERNATIVES IN DREDGE FILL SOILS OVERLAYING ORGANIC CLAY," *Lowl. Technol. Int.*, vol. 15, no. 2, pp. 1–14, 2014.

[126] H. Rashid, L. M. Hunt, and W. Haider, "Urban flood problems in Dhaka, Bangladesh: slum residents' choices for relocation to flood-free areas," *Environ. Manage.*, vol. 40, no. 1, pp. 95–104, Jul. 2007.

[127] A. Taleb, "Comparative Study of Urban Area Extension and flood Risk in Dhaka City of Bangladesh," *Glob. J. Hum. Soc. Sci. Geogr. Environ. Geosci.*, vol. 12, no. 11, 2012.

[128] M. Alam and M. D. G. Rabbani, "Vulnerabilities and responses to climate change for Dhaka," *Environ. Urban.*, vol. 19, no. 1, pp. 81–97, Apr. 2007.

[129] “USGS-EarthExplorer.” [Online]. Available: http://earthexplorer.usgs.gov/.

[130] C. Song, C. E. Woodcock, K. C. Seto, M. P. Lenney, and S. A. Macomber, “Classification and Change Detection Using Landsat TM Data,” *Remote Sens. Environ.*, vol. 75, no. 2, pp. 230–244, Feb. 2001.

[131] G. Jianyaa, S. Haiganga, M. Guoruia, and Z. Qimingb, “A review of multi-temporal remote sensing data change detection algorithms,” in *The International Archives of the Photogrammetry, Remote Sensing and Spatial Information Sciences*, 2008, vol. XXXVII, no. Part B7, pp. 757–762.

[132] M. Akbari, A. R. Mamanpoush, A. Gieske, M. Miranzadeh, M. Torabi, and H. R. Salemi, “Crop and land cover classification in Iran using Landsat 7 imagery,” *Int. J. Remote Sens.*, vol. 27, no. 19, pp. 4117–4135, Oct. 2006.

[133] “ENVI Reference Guide.” © ITT Visual Information Solutions.

[134] H. Rahman, “Agricultural Land Use and Land susceptibility in Bangladesh : An overview,” 2008. [Online]. Available: http://fpd-bd.com/wp-content/uploads/2013/05/agriculturallanduse.pdf.

[135] A. T. Jeyaseelan, “DROUGHTS & FLOODS ASSESSMENT AND MONITORING USING REMOTE SENSING AND GIS,” *Satell. Remote Sens. GIS Appl. Agric. Meteorol.*, pp. 291–313, 2004.

[136] B. Merz, H. Kreibich, R. Schwarze, and a. Thieken, “Review article ‘Assessment of economic flood damage,’” *Nat. Hazards Earth Syst. Sci.*, vol. 10, no. 8, pp. 1697–1724, Aug. 2010.

[137] F. Messner, E. Penning-rowsell, C. Green, S. Tunstall, A. Van Der Veen, S. Tapsell, T. Wilson, J. Krywkow, C. Logtmeijer, A. Fernández-bilbao, P. Geurts, and D. Haase, “Evaluating flood damages: guidance and recommendations on principles and methods principles and methods,” 2007.

[138] E. Pantaleoni, B. a. Engel, and C. J. Johannsen, “Identifying agricultural flood damage using Landsat imagery,” *Precis. Agric.*, vol. 8, no. 1–2, pp. 27–36, Feb. 2007.

[139] M. Haq, M. Akhtar, S. Muhammad, S. Paras, and J. Rahmatullah, “Techniques of Remote Sensing and GIS for flood monitoring and damage assessment: A case study of Sindh province, Pakistan,” *Egypt. J. Remote Sens. Sp. Sci.*, vol. 15, no. 2, pp. 135–141, Dec. 2012.

[140] A. Scarsi, W. J. Emery, G. Moser, F. Pacifici, and S. B. Serpico, “An automated flood detection framework for very high spatial resolution imagery,” in *IEEE Geoscience and Remote Sensing Symposium*, 2014, pp. 4954–4957.

[141] S. Gupta and M. Muralikrishna, “South Asia Disaster Risk Management Programme: Synthesis Report on SAR Countries Disaster Risks,” 2010.

[142] T. H. Dewan, “Societal impacts and vulnerability to floods in Bangladesh and Nepal,” *Weather Clim. Extrem.*, vol. IN PRESS, pp. 1–7, Dec. 2015.

[143] World Bank Group, *Economics of Adaptation to Climate Change - Bangladesh*. 2010.

[144] M. Monirul Qader Mirza, “Global warming and changes in the probability of occurrence of floods in Bangladesh and implications,” *Glob. Environ. Chang.*, vol. 12, no. 2, pp. 127–138, Jul. 2002.

[145] C. Ninno, P. A. Dorosh, L. C. Smith, and D. K. Roy, “The 1998 Floods in Bangladesh Disaster Impacts, Household Coping Strategies, and Response,” WASHINGTON, D.C., 1998.

[146] A. N. H. A. Hossain, “INTEGRATED FLOOD MANAGEMENT CASE STUDY BANGLADESH: FLOOD MANAGEMENT,” 2003.

[147] World Bank, “2004 Floods in Bangladesh Damage and Needs Assessment and Proposed Recovery Program: Main Report,” Washington, DC, 2005.

[148] Bangladesh and Disaster & Emergency Response DER Sub-Group, “Monsoon floods 2004 - Post-flood needs assessment summary report,” Dhaka, Bangladesh, 2004.

[149] “Government of the People’s Republic of Bangladesh - Ministry of Education.” [Online]. Available: http://www.moedu.gov.bd/old/bangladesh.htm.

[150] Y. Wang, Z. Li, Z. Tang, and G. Zeng, “A GIS-Based Spatial Multi-Criteria Approach for Flood Risk Assessment in the Dongting Lake Region, Hunan, Central China,” *Water Resour. Manag.*, vol. 25, no. 13, pp. 3465–3484, Jun. 2011.

[151] M. D. Su, J. L. Kang, L. F. Chang, and A. S. Chen, “A grid-based GIS approach to regional flood damage assessment,” *J. Mar. Sci. Technol.*, vol. 13, no. 3, pp. 184–192, 2005.

[152] J. Yin, D. Yu, Z. Yin, J. Wang, and S. Xu, “Multiple scenario analyses of Huangpu River flooding using a 1D/2D coupled flood inundation model,” *Nat. Hazards*, vol. 66, no. 2, pp. 577–589, Nov. 2012.

[153] A. Zerger and S. Wealands, “Beyond Modelling: Linking Models with GIS for Flood Risk Management,” *Nat. Hazards*, vol. 33, no. 2, pp. 191–208, Oct. 2004.

[154] S. S. Saini and S. P. Kaushik, “Risk and vulnerability assessment of flood hazard in part of Ghaggar Basin: A case study of Guhla block, Kaithal, Haryana, India,” *Int. J. Geomatics Geosci.*, vol. 3, no. 1, pp. 42–54, 2012.

[155] Y. Ouma and R. Tateishi, “Urban Flood Vulnerability and Risk Mapping Using Integrated Multi-Parametric AHP and GIS: Methodological Overview and Case Study Assessment,” *Water*, vol. 6, no. 6, pp. 1515–1545, May 2014.

[156] G. P. Siddayao, S. E. Valdez, and P. L. Fernandez, “Analytic Hierarchy Process (AHP) in Spatial Modeling for Floodplain Risk Assessment,” *Int. J. Mach. Learn. Comput.*, vol. 4, no. 5, pp. 450–457, 2014.

[157] R. Sinha, G. V. Bapalu, L. K. Singh, and B. Rath, “Flood Risk Analysis in the Kosi River Basin , North Bihar Using Multi-Parametric Approach of Analytical Hierarchy Process (AHP),” *J. Indian Soc. Remote Sens.*, vol. 36, no. December, pp. 293–307, 2008.

[158] R. Krishnamurthy and M. Jayaprakash, “Flood hazard assessment of Vamanapuram River Basin, Kerala, India: An approach using Remote Sensing & GIS techniques,” *Adv. Appl. Sci. Res.*, vol. 4, no. 3, pp. 263–274, 2013.

[159] B. Pradhan, “Flood susceptible mapping and risk area delineation using logistic regression, GIS and remote sensing,” *J. Spat. Hydrol.*, vol. 9, no. 2, 2009.

[160] S. J. Carver, “Integrating multi-criteria evaluation with geographical information systems,” *Int. J. Geogr. Inf. Syst.*, vol. 5, no. 3, pp. 321–339, Jan. 1991.

[161] H. Jiang and J. R. Eastman, “Application of fuzzy measures in multi-criteria evaluation in GIS,” *Int. J. Geogr. Inf. Sci.*, vol. 14, no. 2, pp. 173–184, Mar. 2000.

[162] J. Malczewski, “GIS-based multicriteria decision analysis: a survey of the literature,” *Int. J. Geogr. Inf. Sci.*, vol. 20, no. 7, pp. 703–726, Aug. 2006.

[163] G. Kandilioti and C. Makropoulos, “Preliminary flood risk assessment: the case of Athens,” *Nat. Hazards*, vol. 61, no. 2, pp. 441–468, Aug. 2011.

[164] K. Musungu, S. Motala, and J. Smit, “Using Multi-criteria Evaluation and GIS for Flood Risk Analysis in Informal Settlements of Cape Town : The Case of Graveyard Pond,” *South African J. Geomatics*, vol. 1, no. 1, pp. 77–91, 2012.

[165] G. Yalcin and Z. Akyurek, “Analysing flood vulnerable areas with multicriteria evaluation,” in *20th ISPRS Congress*, 2004, pp. 1–6.

[166] S. Yahaya, N. Ahmad, and R. F. Abdalla, “Multicriteria Analysis for Flood Vulnerable Areas in Hadejia-Jama’are River Basin , Nigeria,” *Eur. J. Sci. Res.*, vol. 42, no. 1, pp. 71–83, 2010.

[167] Y. Chen, D. Barrett, R. Liu, L. Gao, M. Zhou, L. Renzullo, S. Cuddy, and I. Emelyanova, “A spatial framework for regional-scale flooding risk assessment,” in *7th International Congress on Environmental Modelling and Software Modelling*, 2014.

[168] T. L. Saaty, *The analytic hierarchy process: planning, priority setting, resources allocation*. New York: McGraw, 1980, pp. 20–25.

[169] D. Lawal and A. Matori, “Detecting Flood Susceptible Areas Using GIS-based Analytic Hierarchy Process,” *2012 Int. Conf. Futur. Environ. Energy IPCBEE*, vol. 28, pp. 4–8, 2012.

[170] S. C. Michaelides, F. S. Tymvios, and T. Michaelidou, “Spatial and temporal characteristics of the annual rainfall frequency distribution in Cyprus,” *Atmos. Res.*, vol. 94, no. 4, pp. 606–615, 2009.

[171] CYPADAPT project (LIFE10 ENV/CY/000723) - Development of a national strategy for adaptation to climate change adverse impacts in Cyprus., “Report on the future climate change impact, vulnerability and adaptation assessment for the case of Cyprus. Deliverable 3.4,” 2012.

[172] World Health Organization, “The WHO e-Atlas of disaster risk for the European Region - Volume 1. Exposure to natural hazards (version 2.0),” 2011. [Online]. Available: http://data.euro.who.int/e-atlas/europe/.

[173] Water Development Department (WDD), “Report on the identification of areas for which potential significant flood risks exist or might be considered likely to occur,” 2011.

[174] D. D. Alexakis, D. G. Hadjimitsis, A. Agapiou, K. Themistocleous, and A. Retalis, “Monitoring urban land cover using satellite remote sensing techniques and field spectroradiometric

measurements: case study of 'Yialias' catchment area in Cyprus," *J. Appl. Remote Sens.*, vol. 6, no. 1, pp. 063603–11, Nov. 2012.

[175] D. D. Alexakis, D. G. Hadjimitsis, and A. Agapiou, "Estimating Flash Flood Discharge in a Catchment Area with the Use of Hydraulic Model and Terrestrial Laser Scanner," in *Advances in Meteorology, Climatology and Atmospheric Physics*, C. G. Helmis and P. T. Nastos, Eds. Berlin, Heidelberg: Springer Berlin Heidelberg, 2013, pp. 9–15.

[176] D. S. Fernández and M. a. Lutz, "Urban flood hazard zoning in Tucumán Province, Argentina, using GIS and multicriteria decision analysis," *Eng. Geol.*, vol. 111, no. 1–4, pp. 90–98, Feb. 2010.

[177] T. Blaschke, "Object based image analysis for remote sensing," *ISPRS J. Photogramm. Remote Sens.*, vol. 65, no. 1, pp. 2–16, Jan. 2010.

[178] F. Franci, A. Lambertini, and G. Bitelli, "Integration of different geospatial data in urban areas: a case of study," in *Second International Conference on Remote Sensing and Geoinformation of the Environment*, 2014, p. 92290P.

[179] S. Bhaskaran, S. Paramananda, and M. Ramnarayan, "Per-pixel and object-oriented classification methods for mapping urban features using Ikonos satellite data," *Appl. Geogr.*, vol. 30, no. 4, pp. 650–665, Dec. 2010.

[180] J. Schiewe, "SEGMENTATION OF HIGH-RESOLUTION REMOTELY SENSED DATA - CONCEPTS , APPLICATIONS AND PROBLEMS," in *Symposium on Geospatial Theory, Processing and Applications*, 2002.

[181] H. Taubenböck, T. Esch, M. Wurm, a. Roth, and S. Dech, "Object-based feature extraction using high spatial resolution satellite data of urban areas," *J. Spat. Sci.*, vol. 55, no. 1, pp. 117–132, Jun. 2010.

[182] M. Baatz and A. Schäpe, "Multiresolution segmentation: an optimization approach for high quality multi-scale image segmentation," in *Angewandte Geographische Informationsverarbeitung XII AGIT symposium*, 2000, vol. 58, pp. 12–23.

[183] U. C. Benz, P. Hofmann, G. Willhauck, I. Lingenfelder, and M. Heynen, "Multi-resolution, object-oriented fuzzy analysis of remote sensing data for GIS-ready information," *ISPRS J. Photogramm. Remote Sens.*, vol. 58, no. 3–4, pp. 239–258, Jan. 2004.

[184] L. Bruzzone and L. Carlin, "A Multilevel Context-Based System for Classification of Very High Spatial Resolution Images," *IEEE Trans. Geosci. Remote Sens.*, vol. 44, no. 9, pp. 2587–2600, Sep. 2006.

[185] T. Esch, M. Thiel, M. Bock, a. Roth, and S. Dech, "Improvement of Image Segmentation Accuracy Based on Multiscale Optimization Procedure," *IEEE Geosci. Remote Sens. Lett.*, vol. 5, no. 3, pp. 463–467, Jul. 2008.

[186] N. S. Magesh, K. V. Jitheshlal, N. Chandrasekar, and K. V. Jini, "Geographical information system-based morphometric analysis of Bharathapuzha river basin, Kerala, India," *Appl. Water Sci.*, vol. 3, no. 2, pp. 467–477, Mar. 2013.

[187] A. N. Strahler, "Quantitative Geomorphology of Drainage Basins and Channel Networks," in *Handbook of Applied Hydrology*, New York: McGraw Hill Book Company, 1964.

[188] R. E. Horton, “Erosional development of streams and their drainage basins; hydrophysical approach to quantitative morphology.,” *Geol. Soc. Am. Bull.*, vol. 56, no. 3, pp. 275–370, 1945.

[189] S. A. Schumm, “Evolution of drainage system and slopes in badlands of Perth Amboy, New Jersey.,” *Geol. Soc. Am. Bull.*, vol. 67, 1956.

[190] S. Shankar and K. Dharanirajan, “Drainage Morphometry of Flood Prone Rangat Watershed , Middle Andaman , India- A Geospatial Approach,” *Int. J. Innov. Technol. Explor. Eng.*, vol. 3, no. 11, pp. 15–22, 2014.

[191] M. Rudraiah, S. Govindaiah, and S. Vittala, “Morphometry using remote sensing and GIS techniques in the sub-basins of Kagna river basin, Gulburga district, Karnataka, India,” *J. Indian Soc. Remote Sens.*, vol. 36, no. December, pp. 351–360, 2008.

[192] R. Parveen, U. Kumar, and V. K. Singh, “Geomorphometric Characterization of Upper South Koel Basin, Jharkhand: A Remote Sensing & GIS Approach,” *J. Water Resour. Prot.*, vol. 4, pp. 1042–1050, 2012.

[193] M. O. Nyadawa and J. K. Mwangi, “GEOMORPHOLOGIC CHARACTERITICS OF NZOIA RIVER BASIN,” *J. Agric. Sci. Technol.*, vol. 12, no. 2, pp. 145–161, 2011.

[194] a. C. Dinesh, V. Joseph Markose, and K. S. Jayappa, “Bearing, azimuth and drainage (bAd) calculator: A new GIS supported tool for quantitative analyses of drainage networks and watershed parameters,” *Comput. Geosci.*, vol. 48, pp. 67–72, Nov. 2012.

[195] K. G. Smith, “Standards for grading texture of erosional topography,” *Am. J. Sci.*, vol. 248, no. 9, pp. 655–668, Sep. 1950.

[196] P. D. Sreedevi, K. Subrahmanyam, and S. Ahmed, “The significance of morphometric analysis for obtaining groundwater potential zones in a structurally controlled terrain,” *Environ. Geol.*, vol. 47, no. 3, pp. 412–420, Oct. 2004.

[197] R. A. Hajam, H. Aadil, and B. SamiUllah, “Application of Morphometric Analysis for Geo-Hydrological Studies Using Geo-Spatial Technology –A Case Study of Vishav Drainage Basin,” *J. Waste Water Treat. Anal.*, vol. 4, no. 3, pp. 1–12, 2013.

[198] M. Civita, *Idrogeologia applicata e ambientale*. 2005, pp. 36–37.

[199] Q. Weng, “Modeling Urban Growth Effects on Surface Runoff with the Integration of Remote Sensing and GIS,” *Environ. Manage.*, vol. 28, no. 6, pp. 737–748, Feb. 2001.

[200] S. Drobne and A. Lisec, “Multi-attribute Decision Analysis in GIS : Weighted Linear Combination and Ordered Weighted Averaging,” *Informatica*, vol. 33, pp. 459–474, 2009.